Nanoscale Magnetic Resonance Imaging and Magnetic Sensing Using Atomic Defects in Diamond

Citation	Grinolds, Michael Sean. 2014. Nanoscale Magnetic Resonance Imaging and Magnetic Sensing Using Atomic Defects in Diamond. Doctoral dissertation, Harvard University.
Accessed	April 17, 2018 4:59:16 PM EDT
Citable Link	http://nrs.harvard.edu/urn-3:HUL.InstRepos:12274105
Terms of Use	This article was downloaded from Harvard University's DASH repository, and is made available under the terms and conditions applicable to Other Posted Material, as set forth at http://nrs.harvard.edu/urn-3:HUL.InstRepos:dash.current.terms-of-use#LAA

(Article begins on next page)

Thesis advisor: Amir Yacoby   Michael Grinolds

Nanoscale magnetic resonance imaging and magnetic sensing using atomic defects in diamond

ABSTRACT

Magnetic resonance imaging (MRI) has revolutionized modern medicine by
providing non-invasive, chemically selective, three-dimensional imaging of living
organisms. Industrial-scale MRI has the capability to image with millimeter-scale
spatial resolution and has the sensitivity to detect as few as 10^{14} nuclear spins.
Increasing spatial resolution to the atomic scale and sensitivity to the single-spin
level would enable a wide array of applications most notably including imaging
molecular structur. However, conventional MRI methods are already highly
optimized, and further order-of-magnitude-scale improvements cannot be
reasonably expected without employing fundamentally different technologies.

This thesis presents an alternative approach to conventional MRI that pushes
resolution and sensitivity to the individual atom and molecular level. The guiding
principle for achieving multiple order-of-magnitude improvements is to
miniaturize the key components of MRI: the detector and the source of
magnetic-field gradients. By scaling down the physical size of these components
to the nano- and atomic- scales, the signals from individual spins become
measurable and resolvable.

To miniature the detector, we employ an optically-active, paramagnetic atomic
defect in diamond - a nitrogen-vacancy (NV) center - as our sensor. Owing to its
optical readout, long coherence times, atomic-size, and room-temperature

compatibility, NV centers in diamond have the capability to measure the magnetic fields from individual spins, provided the sensor can be placed sufficiently close to a target to be measured. This thesis describes the experimental realization of a microscope that can perform sensitive magnetometry experiments using a single NV center that magnetically images by spatially scanning the NV center within a few nanometers of magnetic targets. With this technique we are able to demonstrate the first room-temperature magnetic imaging of individual electron spins.

For miniaturizing the magnetic-field gradient source, we use scanning nanoscale magnets, building off the success of those used in magnetic resonance force microscopy. By shrinking the magnetic field source to tens of nanometers in size, the magnitude of the magnetic field gradients can be increased by more than a factor of 10^5 compared to conventional MRI field gradients coils, which increases spatial resolution correspondingly. With these tips optimized for compatibility with NV-based measurements, we are able to achieve sub-nanometer resolution in MRI imaging.

Contents

Author List

Large portions of Chapter 1 are published as:

"Nanoscale magnetometry with NV centers in diamond", S. Hong, M. S. Grinolds, L. Luan, L. M. Pham, D. Le Sage, R. L. Walsworth, and A. Yacoby, MRS Bulletin 38, 151-161 (2013).

Chapter 2 has been published as

"Quantum control of proximal spins using nanoscale magnetic resonance imaging", M. S. Grinolds*, P. Maletinsky*, S. Hong*, M. D. Lukin, R. L. Walsworth, and A. Yacoby, Nature Physics 7, 687-692 (2011).

Chapter 3 has been published as:

"A robust scanning diamond sensor for nanoscale imaging with single nitrogen-vacancy centres", P. Maletinsky*, S. Hong*, M.S. Grinolds*, B.J.M. Hausmann, M.D. Lukin, R. Walsworth, M. Loncar and A. Yacoby, Nature Nanotechnology 7, 320-324 (2012).

Chapter 4 has been published as

"Nanoscale magnetic imaging of a single electron spin under ambient conditions", M. S. Grinolds*, S. Hong*, P. Maletinsky*, L. Luan, M. D. Lukin, R. L. Walsworth, and A. Yacoby, Nature Physics 9, 215-219 (2013).

Chapter 5 has been published as

"Subnanometre resolution in three-dimensional magnetic resonance imaging of individual dark spins", M. S. Grinolds, M. Warner, K. De Greve, Y. Dovzhenko, L. Thiel, R. L. Walsworth, S. Hong, P. Maletinsky, and A. Yacoby, Nature Nanotechnology AOP (2014).

*These authors contributed equally to this work.

Listing of figures

Acknowledgments

It takes a heck of a lot of people to make a Ph.D's worth of work in Physics - especially on the experimental side of things - and mine is no exception.

First and foremost, I'd like to thank my advisor Amir Yacoby, who I enjoyed working with both personally and professionally. I was initially drawn to the group because of Amir's ability to turn newly discovered physics into novel sensors, but it was really the positive group culture (and consequently how happy everyone in the group was) that compelled me to join. I am so that glad I did, and it was truly a pleasure to get to work Amir on such a new and exciting project.

Throughout the course of my Ph.D. I've had the wonderful opportunity to team up with amazing people for developing and using our NV-AFM magnetometers. For the first two years of the project, I was especially fortunate to get to work hand-in-hand with Patrick Maletinsky and Sungkun Hong in setting up the NV-AFM. I also tried my best to learn as much as I could from them both: I pretty much owe all of my knowledge of optics to Patrick, my fundamentals in programming to Sungkun, and what fab I picked up to both of them. Most importantly, they were amazing teammates, and it was truly fun to come and work with them every day. It's also been great to watch the project grow and evolve with Lan Luan, Marc Warner, Kristiaan De Greve, Lucas Thiel, and Yuliya Dovzhenko. Go team NV!

The NV-AFM and NV-MRI results we were able to achieve would not have happened without help from the greater Harvard NV center community, and I'm really appreciative for the general collaborative environment fostered by the

1
Introduction

Advancements in magnetic detection and imaging have contributed immensely to a wide range of scientific communities from fundamental physics and chemistry to practical applications such as the data storage industry and medical sciences. One classic example is nuclear magnetic resonance [9, 84], which has led to powerful applications, such as magnetic resonance imaging (MRI) [66] . Over the past few decades, many advanced magnetic imaging schemes have been developed with improved sensitivities and spatial resolutions: among those are magnetic force microscopy [67], scanning Hall probe microscopy [15], superconducting interference devices [53], and magnetic resonance force microscopy [105]. However, they are often times limited by operating conditions such as cryogenic temperatures and/or high vacuum, hindering their use towards imaging systems that require ambient conditions.

Recently, negatively charged nitrogen-vacancy (NV) color centers in diamond
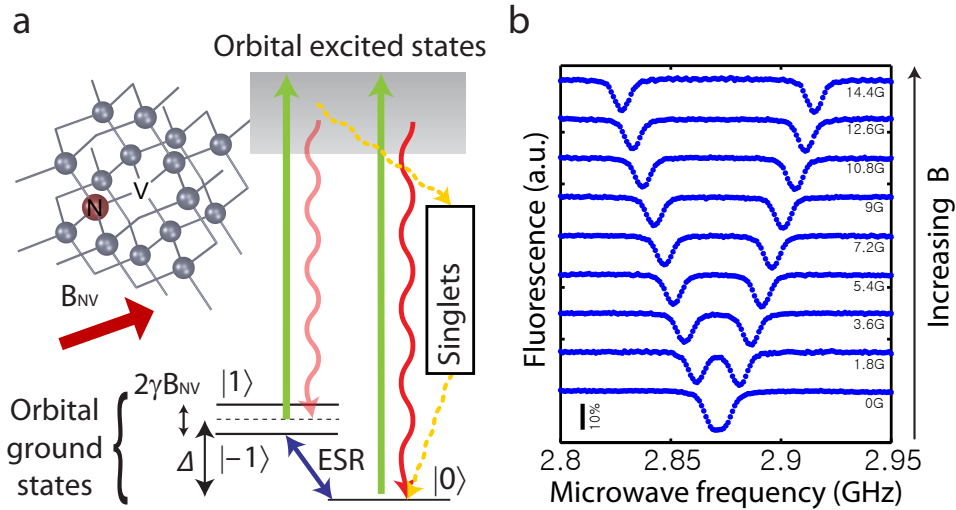
Figure 1.1.1: Nitrogen-vacancy color centers in diamond. (a) Level diagram of a single nitrogen-vacancy center in diamond. (b) Optically detected electron spin resonance as a function of magnetic fields along the NV axis.

have been proposed as a promising system for nanoscale magnetic field sensing [5, 22, 70, 95]. It has been shown, both experimentally and theoretically, that NV centers offer excellent magnetic field sensitivities [70, 95]. Moreover, since NV centers are point defects tightly confined in a crystal lattice, they can be brought in proximity to magnetic samples within a few nanometers, allowing for nanometric spatial resolution, particularly when performing MRI using magnetic field gradients. These sensing capabilities are maintained under ambient conditions (room temperature and atmospheric pressure), and can in principle work in liquid, which is crucial for biological imaging. Over the past few years, these exciting properties have led to rapid progress in developing NV-based magnetometers.

1.1 MAGNETIC FIELD SENSING WITH NV CENTERS

The NV center is a point defect in diamond consisting of a substitutional nitrogen with a vacancy in its nearest neighbor lattice site (Fig. 1.1.1a). The negatively charged state forms a spin triplet in the orbital ground state. The crystal field splits these spin sublevels, resulting in the $m_S = 0$ state in the lowest energy state, and the $m_S = \pm 1$ sublevels lifted by 2.87 GHz. An additionally applied external magnetic field splits the $m_S = \pm 1$ sublevels, which isolates an effective spin-1/2 system. The population of this spin-1/2 system can be read out and initialized optically via spin-dependent fluorescence and optical pumping, respectively. These optical readout and initialization schemes, along with the coherent microwave manipulation, allow for full control of the NV center's spin states.

Magnetic field sensing with NV centers is based on Zeeman splitting of the NV center's spin states [5, 70, 95], where the $m_S = \pm 1$ states split in proportion to the magnetic field along the N-V axis. This Zeeman energy shift can be read out optically. Optically detected electron spin resonance spectra [41] (ESR), for instance, can be used for magnetic field sensing, as spin resonance frequencies shift proportional to external magnetic fields (Fig. 1.1.1b).

A well-established methodology to precisely determine Zeeman shifts is to monitor changes in spin precession, as widely used in spin-based magnetometers such as atomic vapor cells [13]. This type of approach uses a Ramsey-type measurement sequence [95], where additionally accumulated phase $\varphi = \gamma B \tau$ ($\gamma = g e \mu_B / \hbar$ is the gyromagnetic ratio of an electron spin) during a fixed evolution time τ measures the local magnetic field B (Fig. 1.1.2a). This accumulated phase is converted to a population difference, which can be read out via an NV center's spin-dependent fluorescence. In the limit of small magnetic field, the corresponding shot-noise-limited sensitivity, or minimally detectable field δB_{opt} within a second, can be expressed by

$$\delta B_{opt} \sim \frac{2}{\gamma C} \frac{1}{\sqrt{F_{mean} N \tau_{opt}}}$$
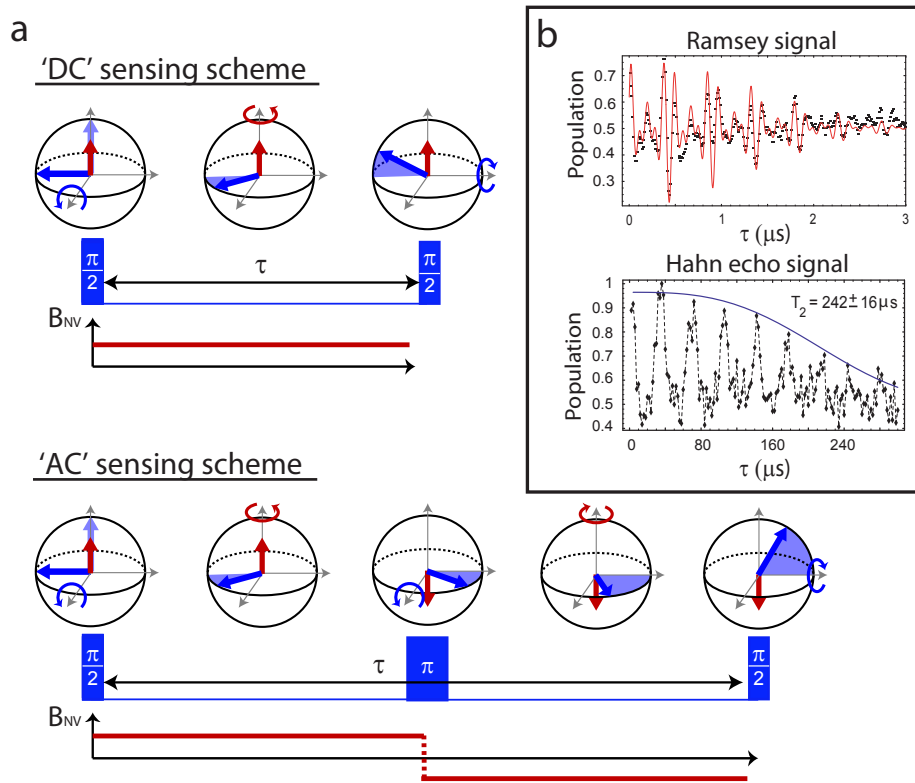
Figure 1.1.2: Magnetic field sensing with NV centers. (a) Magnetic field detection scheme with ESR pulse sequences. Measurement of static magnetic field is based on a Ramsey pulse sequence (top). The measurement starts with preparing an NV spin's state to an equal superposition of m_S=0 and m_S=1 (or -1) by applying a $\pi/2$-pulse. During a free evolution time, τ, phase is accumulated in proportion to the field. The second $\pi/2$-pulse converts the phase to the population of the NV's spin state, which then can be measured through spin-dependent fluorescence. The sensitivity of this measurement is limited by the coherence time of the Ramsey sequence. An echo-based pulse sequence can improve the magnetic field sensitivity (bottom), provided that it measures the AC magnetic field with its period matched to the total free evolution time, allowing for a longer free evolution time by prolonging the coherence time. (b) Electron spin coherence times of an NV center in high-purity diamond. The figures are adapted with permission from Reference [17]. ©2006. American Association for the Advanced of Science. The coherence time in the Hahn echo signal (242 μs) is two orders of magnitude longer than the coherence time of the Ramsey signal ($\approx$ 2 μs).

4

where F_{mean} is the mean number of photons collected per one measurement shot, C is the fluorescence contrast between the spin states $m_S = 0$ and $m_S = 1$, N is the number of NV centers participating in the measurement, and τ_{opt} is the optimal evolution time, which would normally be determined by NV spin's phase coherence time. The coherence time, otherwise limited by environmental fluctuations, can be extended by orders of magnitude using decoupling sequences such as a Hahn-echo squence [20, 95] (Fig. 1.1.2b). Using these techniques, often referred as 'AC sensing schemes', an NV center becomes sensitive only to alternating magnetic fields [95], requiring modulation of targeted magnetic sources. For paramagnetic spins, this can be achieved by conventional resonant driving methods. Using this AC sensing scheme, it has been shown that a single NV center in high purity diamond is already capable of $30 \, \mathrm{nT}/\sqrt{\mathrm{Hz}}$ sensitivity [70], and can achieve $4 \, \mathrm{nT}/\sqrt{\mathrm{Hz}}$ by isotope engineering [6].

A critical advantage of magnetic sensing with NV centers is that they are atomic-sized point defects in solids. Nanoscale magnetic imaging generally requires the sensor's close proximity to the sample of interest in addition to small detection volume of the sensor, since the magnetic fields from individual spins, the fundamental building blocks of magnetism, fall off as $1/r^3$. Fulfilling these requirements is a challenging problem in other spin-precession-based magnetometers, as the spatial extent of sensing atomic clouds are limited by the sizes of their traps. However, for a single NV center, crystal lattices naturally provide a tight and stable trapping of NV centers within only a few angstroms. Furthermore, it has been recently reported that NV centers can be formed within 5 nm from the diamond surface while maintaning coherence times longer than $100 \, \mu s$ [80]. This combination of tight confinement and nanometer-scale proximity to the diamond surface suggests that it is feasible to bring NV centers within a few nanometers from the sample. In addition, these solid-state aspects of NV centers are also advantageous for artificially engineering NV centers. For instance, well-established techniques for defect engineering, such as ion-implantation [83] and delta-doping [80], can be readily applicable to create NV centers with few nanometer position accuracy.
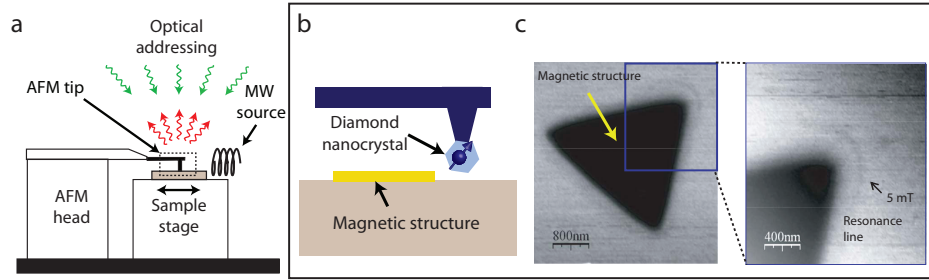
Figure 1.2.1: Scanning magnetometry with a single NV center. (a) Schematic of scanning NV magnetometry. (b) Schematic of an AFM probe with diamond nanocrystal containing a single NV center. (c) Spatial image of a magnetic field profile from a magnetic structure acquired by a diamond nanocrystal probe. The images are adapted with permission from Reference [5]. ©2008. Nature Publishing Group.

1.2 SCANNING MAGNETOMETRY WITH A SINGLE NV CENTER

A natural approach to implement nanoscale magnetometry with a single NV center to utilize scanning probe techniques with the NV center residing at the end of the tip [16, 22] (Fig. 1.2.1a). In this configuration, well established atomic force microscopy (AFM) methods allow for localizing the sensing NV to within a few nanometers of samples of interest. In addition, to collect spin-dependent fluorescence from an NV center, conventional far-field optics can be used. Finally, a microwave source is installed to manipulate the spin state of an NV center to perform magnetometry experiments.

Maintaining a short stand-off distance between the sensing NV centers and the sample is crucial for nanoscale imaging. The first scanning NV magnetometer was implemented by using commercially available diamond nanocrystals hosting a single NV center grafted at the apex of an AFM tip [5] (Fig. 1.2.1b). The size of the nanocrystals, nominally 40 nm in diameter, ensures proximity of an NV center to the sample and corresponding magnetic spatial resolution within a few tens of nanometers. Magnetic images could then be acquired by scanning the NV center with respect to the sample, while recording the NV's spin-dependent

fluorescence in response to the sample's local magnetic field.

This first scanning NV magnetometer successfully demonstrated feasibility of magnetic imaging using NV centers as a local probe. However, the magnetic field sensitivity was limited by the NV sensor's short coherence time due to a high concentration of paramagnetic defects in commercial diamond nanocrystals.

1.3 MRI USING NANOSCALE MAGNETIC FIELD GRADIENTS

While the spatial resolution of a scanning NV magnetometer is generally determined by its distance to a sample, the resolution can be improved by applying a magnetic field gradient and performing MRI, provided the targeted magnetic sample consists of paramagnetic spins that can be spectrally driven [5, 95]. Under the presence of a magnetic field gradient, two otherwise identical paramagnetic spins at distant locations experience different magnetic fields, resulting in spectrally separated spin-resonance frequencies. This spectral separation allows for selectively driving spins at particular locations and therefore can be converted to an imaging spatial resolution given by $\frac{1}{\tau\gamma\nabla B_{tip}}$. Here, γ and τ are the target spin's gyromagnetic ratio and spin-interrogation time, respectively, and ∇B_{tip} is the gradient of the tip's magnetic field at the target spin's position projected along the spin's quantization axis. In general, γ is fixed and the maximum τ is limited by the target's coherence time, and so to increase spatial resolution it is necesary to increase the magnitude of the magnetic field gradients.

Achieving nanoscale resolution with conventional MRI magnets is difficult because these magnets are roughly 1 m in size, and fields exeeding 10 T are experimentally infeasible. To increase the gradients further, rather than increasing the magnitude of the field, it is advantageous to instead decrease the size of the magnet and bring it close to magnetic targets. To this end, the magnetic resonance force microscopy community developed scanning magnets that have gradients exceeding $1.4 \cdot 10^6$ T/m [63], which afford a 10^5 improvement in MRI spatial resolution. Similar scanning nanomagnets can be applied to NV-based MRI imaging when they are optimized to work in a low-field

environment and have a small total magnetic field so as to minimize the field component off-axis to the NV sensor [37, 39].

1.4   DESCRIPTION OF THIS THESIS

This thesis describes experimental progress in developing nanoscale NV-based MRI and achieving single-spin sensitivity and sub-nanometer spatial resolution.

Chapter 2 presents proof-of-principle experiments demonstrating the potential for performing MRI using NV centers and nanoscale magnetic field gradients [37]. In this work, we employed a scanning nanomagnet to image the location of individual NV centers, which were sufficiently dense so that they could not be resolved optically. By scanning the gradient and leveraging the optical readout of the imaged NV centers, we achieved 9-nm spatial resolution in three-dimensional MRI. This work additionally outlines the combined confocal and atomic-force microscope used throughout this thesis: for all experiments, an NV center is placed in the focus of a confocal microscope to read out the NV spin state through optically detected magnetic resonance. Simultaneously, either a sample or magnetic field gradient source is scanned in three dimensions with angstrom precision, and the magnetic field at the NV center is measured as a function of space, yielding three-dimensional images.

Chapter 3 extends NV-based magnetic imaging to arbitrary magnetic targets by developing a scanning NV magnetometer. To achieve this, we developed a fabrication procedure to create diamond AFM tips that contain single NV centers at their apex. Specifically, we create monolithic diamond cantilevers with diamond nano-pillars with single NV centers artificially implanted within a few tens of nanometers from the tip surface [62]. Because these devices are fabricated from high-purity diamond, we achieve longer coherence times than those of commercial diamond nanocrystals. Moreover, the nano-pillars are designed to support efficient optical wave-guiding of the NV's fluorescence by more than a factor of five compared to conventional far-field collection, while requiring an order of magnitude less optical excitation power [4]. This

combination of long coherence time and increased photon collection efficiency results in excellent magnetic field sensitivity. As a result, an unprecedented combination of high magnetic field sensitivity ($56\,\mathrm{nT}/\sqrt{\mathrm{Hz}}$) and nanoscale spatial resolution ($25\,\mathrm{nm}$) was demonstrated.

Chapter 4 presents nanoscale imaging of the magnetic field from a single electron spin using our scanning NV devices, under ambient conditions [38]. This work constitutes the first room-temperature magnetic imaging of a single electron spin and demonstrates the capability and robustness of our scanning NV magnetometer.

Finally, in Chapter 5 we develop and apply a scheme for performing NV-based MRI on arbitrary spin targets [39]. In this work, instead of imaging the location of NV spins [37], a single NV spin is used as a sensor of its local magnetic field environment, while a scanning field gradient brings proximal target spins in and out of magnetic resonance. By mapping the NV response to driven target spins as a function of field gradient, the density of spins coupled to the NV center is mapped in three-dimensions. We demonstrate that MRI imaging using this technique can achieve sub-nanometer resolution and single spin sensitivity. In conjunction with the scanning probe methods developed in Chapter 3 and Chapter 4, this MRI mode provides a powerful tool for nanoscale MRI of arbitrary targets under ambient conditions.

2

Nanoscale magnetic resonance imaging of proximal NV spins

2.1 Introduction

Quantum control of individual spins in condensed matter systems is an emerging field with wide-ranging applications in spintronics [2], quantum computation [77], and sensitive magnetometry [16]. Recent experiments have demonstrated the ability to address and manipulate single electron spins through either optical [49, 101] or electrical techniques [31, 43, 73]. However, it is a challenge to extend individual spin control to nanoscale multi-electron systems, as individual spins are often irresolvable with existing methods. Here we demonstrate that coherent individual spin control can be achieved with few-nm resolution for proximal electron spins by performing single-spin magnetic

resonance imaging (MRI), which is realized via a scanning magnetic field gradient that is both strong enough to achieve nanometric spatial resolution and sufficiently stable for coherent spin manipulations. We apply this scanning field-gradient MRI technique to electronic spins in nitrogen-vacancy (NV) centers in diamond and achieve nanometric resolution in imaging, characterization, and manipulation of individual spins. For NV centers, our results in individual spin control demonstrate an improvement of nearly two orders of magnitude in spatial resolution compared to conventional optical diffraction-limited techniques. This scanning-field-gradient microscope enables a wide range of applications including materials characterization, spin entanglement, and nanoscale magnetometry.

Magnetic field gradients allow for spatially distinguishing spins in ensembles, as fields locally modify the spins' resonance frequencies. Spatially separated spins can therefore be addressed selectively, allowing for magnetic resonance imaging (MRI), which has revolutionized the medical and biological sciences by yielding micron-scale imaging of nuclear spins [61, 66]. Performing MRI on single spins with high spatial resolution is attractive both for determining structure on the molecular scale and for achieving individual spin quantum control in ensemble systems. With conventional MRI techniques, however, it is difficult to improve the spatial resolution to the nanoscale due to insufficient readout-sensitivity and inadequate magnetic field gradients [35]. Recently, magnetic field gradients introduced via scanning probe techniques have enabled single spin detection with few-nm resolution [5, 88]; however, control and characterization of individual spins in nanoscale clusters has not been demonstrated thus far.

Here we perform scanning field-gradient MRI on proximal electron spins in nanoscale ensembles and demonstrate a spatial resolution < 10 nm under ambient conditions. We show that scanning field-gradient microscopy not only allows for imaging but further provides quantum spin control for characterization and manipulation of individual spins on the nanoscale. By pushing the spatial resolution to few-nm length scales, our results illustrate that quantum control of individual spins can be maintained in dense ensembles of

spins (with spins separated by a few tens of nanometers), where the mutual coupling between adjacent spins can exceed their decoherence rates [76] ($1/T_2$). Thus, scanning-field-gradient MRI will help facilitate the creation of entangled spin-states with applications for quantum information processing and sensitive, nanoscale magnetometry. Although our approach is applicable to any spin system where spins can be initialized and read out, we focus here on the electronic spins associated with NV centers in diamond, where spin initialization and readout can be performed optically [41]. In addition, NV spins are attractive for performing quantum information processing [29, 76] and sensitive magnetometry [5, 22, 70, 95]. Individual NV spin control in a nanoscale ensemble is a key advance towards the implementation of these applications.

2.2 Magnetic resonance imaging of a single NV center using the scanning-field-gradient

Our scanning-field-gradient MRI system (Fig. 2.2.1a) is comprised of an atomic force microscope (AFM) with a magnetic tip and integrated into an optical confocal microscope (see Fig. 2.6.2), all operating under ambient conditions. The magnetic tip used in the experiments is a laser-pulled quartz tip coated with a 25 nm magnetic film (see Fig. 2.6.1). Small ensembles of shallowly implanted NV centers, nominally 10 nm below the surface of a diamond sample, are placed in the confocal spot (volume $< 1\,\mu m^3$) where an excitation laser at 532 nm is used to initialize and read out the NV centers' spin states. Because of the NV centers' spin-dependent fluorescence ($\approx 630 - 800$ nm), optically detected electron spin resonance (ESR) can be observed by sweeping the frequency of a driving radio-frequency (RF) field through the spin resonance and measuring the corresponding variation in fluorescence (Fig. 2.2.1b) [41], in this case on a single NV center. As has been demonstrated by Balasubramanian et al. [5], a magnetic tip in proximity to an NV center shifts the energy of the NV spins, particularly for fields along the NV axis. By selectively detuning the applied RF field and scanning the magnetic tip over a single NV center, a magnetic field map

corresponding to the applied detuning can be acquired (Fig. 2.2.1c). Using the AFM to regulate the magnetic tip's height allows for precise nanoscale control of the tip's location in three dimensions: the height of the tip is maintained via a conventional feedback loop on the force from the sample, while several-nm precision in lateral positioning is achieved by using the sample's topography as a marker.

2.3 Three-dimensional nanoscale MRI of proximal NV spins

We first demonstrate how this technique can be used for imaging proximal NV spins. The magnetic response shown in Figure 2.2.1c provides a direct means for determining the relative location of proximal NV centers. For NVs with an identical orientation, the indistinguishable nature of their spins leads to an identical but spatially shifted magnetic field map for each NV spin. Thus, magnetic resonance images of single-spins (such as in Figure 2.2.1c) can serve as the point spread function for multi-spin imaging. To demonstrate the performance of this technique, we executed scanning-field-gradient imaging on three closely spaced NV centers (Fig. 2.3.1). As the magnetic tip is scanned laterally across the sample, a magnetic field contour is observed for each center. Here, we selected an ensemble of NVs where all three have a common quantization axis orientation, so that every spin responds in the same way to the presence of the magnetic tip. Thus, the relative distances between NV spins can be obtained by quantifying the spatial shift between the observed resonance rings through a deconvolution procedure (see Fig. 2.6.4). The resulting image (Fig. 2.3.1a) indicates the relative positions of the NV centers, which we find are spaced by 50 nm and 75 nm with respect to NV II. A spatial resolution of 9 nm can be extracted from the width of the resonance ring along the vector connecting NV centers II and III; a precision of 0.2 nm can be determined from a two-dimensional Gaussian fit to the deconvolved peak. This estimate of precision only accounts for variance induced by random noise and does not account for
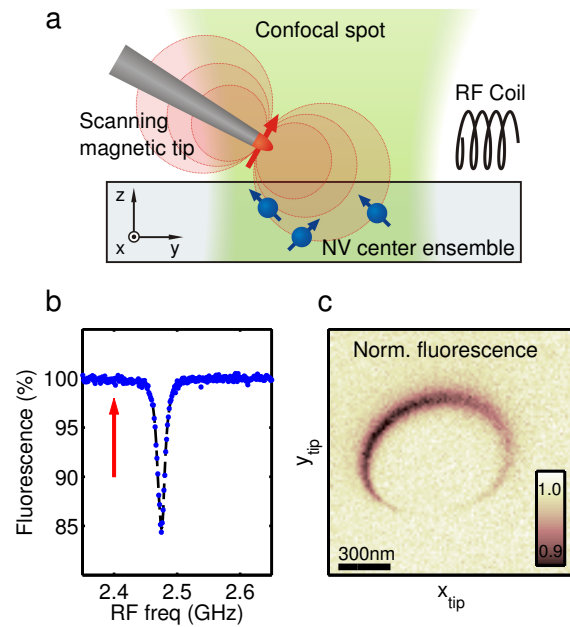
Figure 2.2.1: Two-dimensional imaging of a single NV center using the scanning-field-gradient MRI microscope. (a) Schematic of the experimental approach. A magnetic tip is scanned by an AFM over a diamond sample containing multiple shallow NV centers separated by distances smaller than the optical excitation wavelength. Each NV center experiences a different magnetic field from the tip. Thus, spin transitions for individual NV centers can be selectively driven by tuning the frequency of an externally applied radio-frequency (RF) field. A confocal microscope provides NV spin-state preparation via optical pumping, and detection via spin-state dependent fluorescence. (b) Optical fluorescence measurement of the electron spin resonance (ESR) of a single NV center in the absence of the magnetic tip. The NV-spin-dependent fluorescence rate leads to a drop in emitted (and detected) photons when the external RF source is swept onto the NV spin resonance (here at 2.47 GHz instead of the zero-field value of 2.87 GHz because of an applied static magnetic field). (c) Two-dimensional magnetic resonance image of a single NV center, created by scanning the magnetic tip across the surface and fixing the RF frequency off resonance from the NV ESR transition (see arrow in (b)). A reduction of fluorescence is observed for positions of the magnetic tip relative to the NV that put the NV spin on resonance with the RF field, creating a dark "resonance ring". The plotted fluorescence magnitude is normalized to the NV fluorescence when no driving RF field is applied near the ESR transition (see Fig. 2.6.3).

14

systematic deviations caused by effects such as scanner non-linearity or deviations from the peak shape to the Gaussian fit.

Our single-spin MRI technique can be extended to three dimensions by performing magnetic tomography, where the magnetic tip is retracted from the surface in few-nm steps and scanned laterally (Fig. 2.3.1b). The size of the resonance rings evolves quickly as a function of z-distance as the magnetic field from the tip becomes too weak to bring the spin-transitions into magnetic resonance with the detuned RF driving field. The height differences between the NVs can be seen here as NV I vanishes roughly 15 nm before the other two, which indicates that NV I lies roughly 15 nm further below the surface than both NV II and III. A vertical scan across NVs II and II shows the z-resolution of this measurement to be 10 nm, which is extracted from the width of the resonance line in the z-direction. Since the lateral separation of these two NVs is larger than our spatial resolution, we can determine the relative height of the two NVs with high precision, which we find to be 3 nm.

The NV centers in our demonstration experiments were created through implantation of nitrogen ions forming a layer $\approx$ 10 nm below the diamond surface. Modeling of this implantation procedure [104] predicts a spatial variation of ± 3 nm; whereas we observe a larger variation in the distribution of NV depths (> 10 nm) using our scanning-field-gradient MRI technique. This discrepancy may arise from ion channeling or surface effects. Nanoscale precision in measuring the distance between proximal NV spins also allows determination of the mutual dipole coupling between adjacent spins (see Supp. 2.6.5), a key component for creating entangled spin-states.
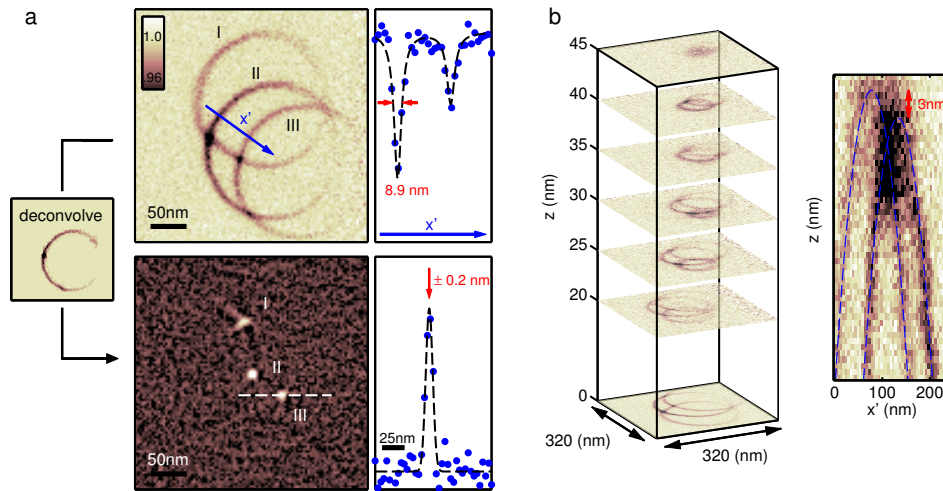
Figure 2.3.1: Three-dimensional magnetic resonance imaging of proximal NV spins. (a) Scanning the magnetic tip over a cluster of three NV centers with the same crystallographic orientation yields multiple dark-resonance rings in the observed fluorescence, one for each NV center (upper image). The relative locations of the NV centers are extracted from the magnetic resonance image through a deconvolution process (see Supp. 2.6.4), yielding adjacent NV-NV distances of 50 nm and 70 nm (bottom, left image, which plots the normalized deconvolved signal). ESR spectral linecuts (top, right) give a spatial resolution of roughly 9 nm with 0.2 nm precision taken from a two-dimensional Gaussian fit to the deconvolved peak (bottom, right). (b) The relative depths of the NV centers below the diamond surface are determined by taking magnetic resonance images for different magnetic tip heights above the sample surface. Comparing the evolution of the three NV resonance rings as a function of tip-to-sample distance, we determine that NV I lies roughly 15 nm below NV II and NV III (stack of images on left). A vertical cut further resolves NV II and NV III, showing that they are 3 nm apart in depth (right image).

16

2.4 INDIVIDUAL AND SELECTIVE QUANTUM CONTROL AND CHARACTERIZATION OF PROXIMAL NV SPINS

Scanning-field-gradient MRI provides not only a method for nanoscale mapping of the spatial locations of proximal spins but also allows for individual spin transitions to be resolved in frequency space with high precision. In the absence of magnetic field gradients, identical spins sharing a quantization axis are indistinguishable, making selective control over proximal spins impossible. Performing scanning-field-gradient MRI on proximal spins differentiates their transition frequencies, allowing for coherent manipulation and characterization of individual spins in the ensemble. This can be done simultaneously on several NV spins while preserving independent control of each spin. Such selective control over proximal spins can be maintained as long as the magnetic field gradient separates the transition frequencies of neighboring spins by more than their resonance linewidth, which is the same condition that determines the spatial resolution in MRI. Therefore, spins separated by more than the achieved MRI spatial resolution ($\approx$ 9 nm for the NV spin experiments reported here) can be addressed independently using our technique.

To demonstrate such selective nanoscale characterization and control of proximal spins we examined a pair of proximal NV centers (NV IV and NV V, separated by 135 nm, see Supp. 2.6.6), which share the same NV axis orientation. In the absence of the magnetic tip, we performed a continuous-wave ESR measurement on both NV spins simultaneously (Fig. 2.4.1a, left panel), finding no difference in their spectra, as expected. After tuning the RF frequency to the pair of NV spins, we drove Rabi oscillations and observed the free induction decay of the two NV spins via a Ramsey sequence (Fig 2.4.1a, right panels). The measured Ramsey fringes show a pronounced beating pattern due to the hyperfine structure of the NV spin transitions and are damped due to inhomogeneous dephasing of the two NV centers. However, information

distinguishing the individual coherence-properties of the proximal NV centers cannot be extracted from these measurements. In contrast, when the magnetic tip is brought in close proximity to the NV spins, it splits their resonance frequencies due to the differing magnetic fields applied to each NV, thereby allowing each NV spin to be addressed and characterized individually and coherently (Fig. 2.4.1b) without modifying the spin of the neighboring NV.

Such coherent individual spin control was realized by tuning the RF frequency to the ESR resonance of the target NV center. Pulsing the RF with a variable duration induced coherent Rabi oscillations of either NV IV or NV V, depending on the tuning of the RF frequency. Similarly, characterization of individual spin coherence properties was achieved by measuring the spin's free-induction decay via a Ramsey sequence using the appropriate RF frequency for the target NV spin. We observed that NV IV has a faster free-induction decay rate than NV V, indicating that the two spins have different inhomogeneous dephasing times, T_2^*. The measured free-induction decay rate for NV V with and without the magnetic tip are comparable, indicating that additional decoherence induced by the tip is small compared to that spin's ambient dephasing $1/T_2^*$. In order to prevent tip-induced spin-decoherence, we employed a three-dimensional spatial feedback scheme, which ensured that variations in the applied tip-field were smaller than the intrinsic NV inhomogeneous dephasing rates (see Supp. 2.6.7). Thus, the applied magnetic field gradient can be used to characterize individual spin coherence properties, which is a direct consequence of achieving single-spin control.

Figure 2.4.1: Individual quantum control and characterization of proximal NV centers. (a) With the magnetic tip pulled far away from the sample, two NV centers (IV and V) separated by 135 nm (see Supp. 2.6.6) and sharing the same spin-quantization axis cannot be resolved by their ESR spectra ($m_S = 0 \to m_S = 1$ transition of the NV triplet groundstate, observed by spin-state dependent fluorescence), as they experience the same static magnetic field (left panel). By driving both NVs at once, Rabi oscillations (middle panel) and the NV spins' collective free-induction decay (right panel) can be observed using the indicated Rabi and Ramsey RF pulse sequences. (b) With the magnetic tip in close proximity to the sample, the two NV spin resonances are spectrally distinguishable by their differing Zeeman shifts (left panel; $\approx$ 30 MHz splitting), allowing each NV to be addressed independently, so that Rabi oscillations (middle panel) and Ramsey free-induction decay (right panel) of each NV spin can be individually measured (NV IV in red and NV V in green). For these measurements, the probability of the spin being in the mS=0 state is plotted.

Figure 2.4.1 *(Continued)*
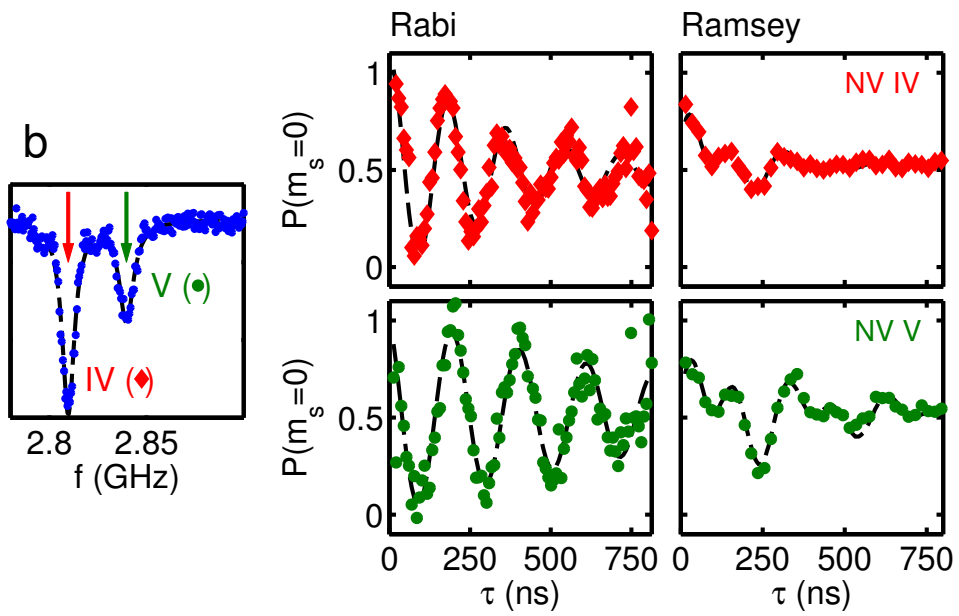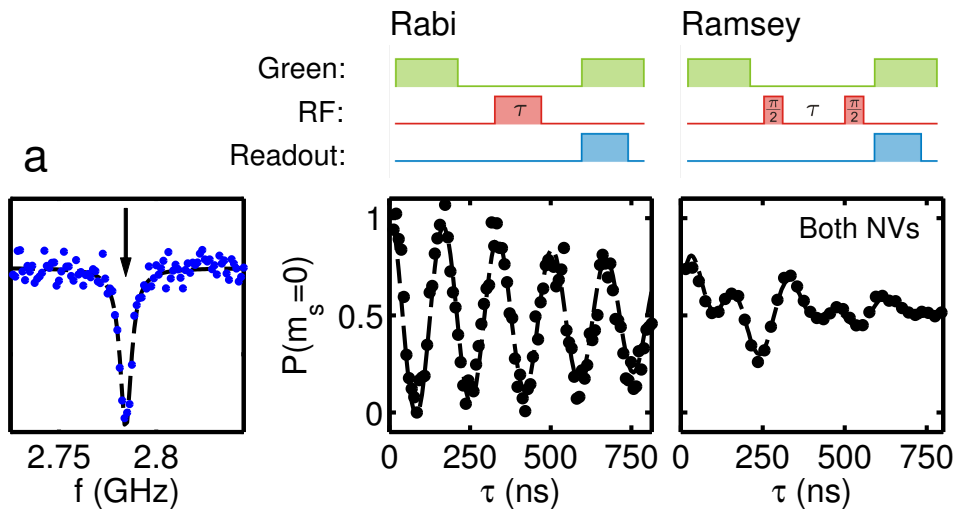
Figure 2.4.2: Selective, independent RF control of proximal NV spins in the presence of the tip magnetic field gradient. (a) Fluorescence measurements were performed for the same two proximal NV centers as in Figure 2.4.1, while undergoing simultaneous, near-resonant driving by fields RF 1 and RF 2; and with the tip magnetic field gradient inducing a large ($\approx$ 30 MHz) Zeeman frequency shift between the ESR frequencies of the two NV spins. The frequency of RF 1 was set on resonance with NV IV and was pulsed with varying duration (τ_{RF_1}) to induce Rabi oscillations. Simultaneously, RF 2 was continuously applied while its frequency (ω_{RF_2}) was swept through the spin resonance of NV V to measure its ESR spectrum. (b) Two-dimensional data set sweeping over τ_{RF_1} and ω_{RF_2} for the two NV spins (base of cube). Individual behavior of each NV spin is extracted by subtracting the mean measured fluorescence for each row (i.e., fixed value of ω_{RF_2}) from the data for that row; and similarly for each column (fixed value of τ_{RF_1}). The resulting extracted data sets (shown in the sides of the cube) are found to be independent of row or column number, showing that varying the Rabi pulse duration τ_{RF_1} for NV IV does not influence the results of sweeping ω_{RF_2} through the spin resonance of NV V, and vice versa. Summing up the measurements for all rows and columns yields the resulting averaged Rabi oscillation measurement for NV IV (top of left wall) and ESR spectrum from NV V (top of right wall), respectively.

Figure 2.4.2 *(Continued)*

a

Green:

RF 1: τ

RF 2: ω

Readout:

b

NV IV

NV V

$P(m_s)=0$

Fluor. (a.u)

Row #

Col #

2.88
2.87
2.86
2.85
2.84

ω_{RF2} (GHz)

600
400
200

τ_{RF1} (ns)
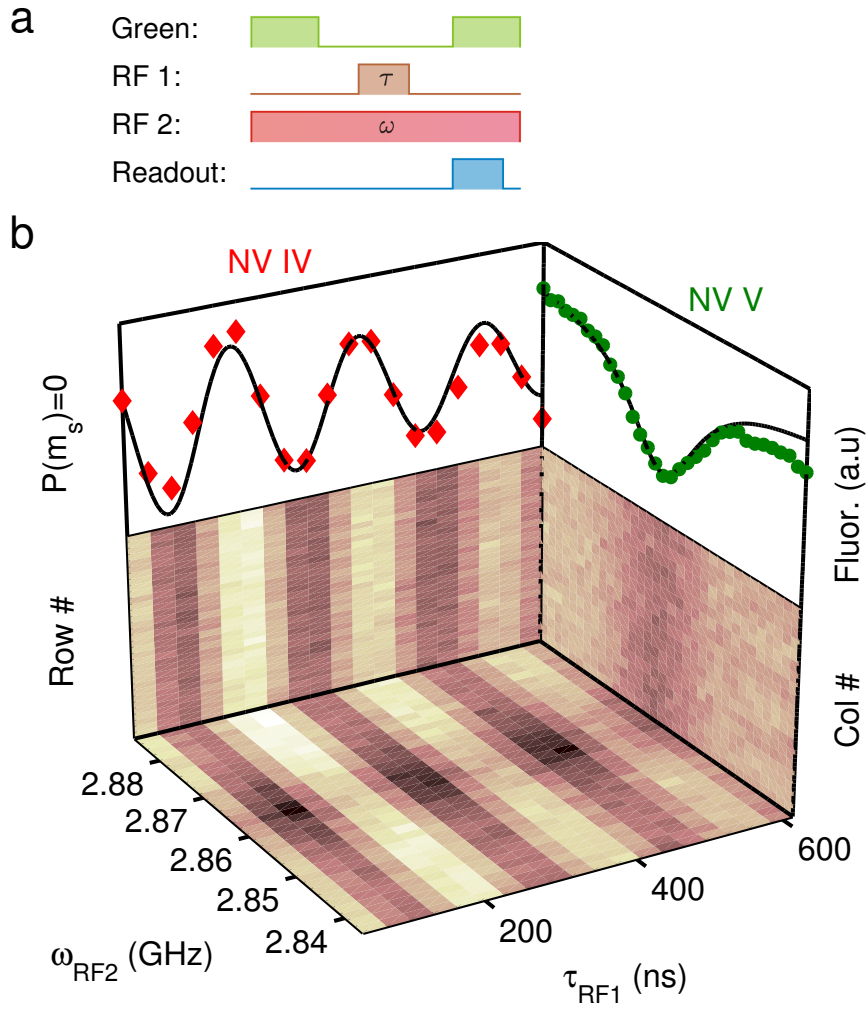
Under the influence of the tip's magnetic field gradient, manipulating one NV spin does not perturb the state of a neighboring NV spin. To experimentally verify this selective, independent spin control, we simultaneously drove Rabi oscillations on NV IV while measuring the ESR spectrum of NV V (Fig. 2.4.2a) by applying two separate RF fields (RF 1 and RF 2), each used to drive one NV spin-resonance. To illustrate the independence of the two measurements, we performed a two-dimensional sweep over the RF 1 pulse duration (τ_{RF_1}) and the frequency of RF 2 (ω_{RF_2}) (Fig. 2.4.2b). We then subtracted out the mean of each row or column to show that the two measurements are independent. Rows or columns were summed to reconstruct the resulting Rabi oscillations of NV IV or the ESR curve of NV V, respectively. The only deviations from simultaneous, independent NV spin measurements are observed when ω_{RF_2} is swept close to the resonance of NV IV, yielding a slight damping in the Rabi oscillations. These deviations do not persist through the ESR transition of NV V, which shows that both NVs can be manipulated independently when they are driven on resonance.

2.5　Discussion and outlook

There are several promising avenues in applications of field-gradient MRI. First of all, we expect that the demonstrated magnetic field gradient method can be used to improve spatial resolution of the scanning NV magnetometer introduced in Chapter 3 and, 4 [95]. The field-gradient-induced spectral separation of identical spins at different positions provides an orthogonal means to attain spatial resolution not limited by the sensor-to-target separation, and could potentially be pushed to the sub-nm scale with experimentally achieved field-gradients [63]. Realizing such nano- or atomic scale resolution in imaging single paramagnetic spins under ambient conditions would enable diverse applications such as imaging magnetic point defects in solid-state systems [74] and tracking individual spin-labels in biological systems [3].

In addition, scanning-field-gradient MRI of spins yields precise determination of their relative locations with nanometric spatial resolution, which will be

crucial for optimizing the functionality of spin-based quantum bit ensembles. Once suitable spin ensembles are identified and spatially mapped, individual spin control both allows for the determination of individual spin properties and - when combined with magnetic dipole coupling between adjacent spins - provides a method for achieving complete control of the quantum state of spin ensembles. For our demonstrated spatial resolution (9 nm) in resolving nearby spins, coupling rates between proximal spins can be as strong as 36 kHz for optimally oriented spins. Thus, so long as spin coherence times exceed 28 μs, such spins can be entangled. As NV spin coherence times up to 1.8 ms have been demonstrated [6], our scanning-field-gradient MRI is immediately applicable from sensitive nanoscale magnetometers to scalable quantum information processors [103].

The control and manipulation of individual spins using magnetic field gradients is independent of the method used for spin readout, therefore can be extended to other spin qubit systems. For optically addressable spins, such as NV spins, integrating far-field, sub-diffraction schemes - such as stimulated emission depletion (STED) [86] and reversible saturable optical linear fluorescence (spin-RESOLFT) [68] - with a scanning magnetic field gradient would allow for both robust individual spin control and readout with nanometric resolutions. In addition, selective optical control of such systems is possible via the incorporation of an electric field gradient to the scanning tip [47], which would allow both spin and electronic degrees of freedom to be both addressed individually. Alternatively, using demonstrated single-shot electrical readout of individual spins [7, 73] would allow for MRI to be performed rapidly and efficiently, as acquisition times would not be limited by the readout integration time.

400 nm

Figure 2.6.1: Scanning electron micrograph of a quartz tip with magnetic coating. The metal coating is overlain in red (false color).

2.6 SUPPLEMENTARY SECTION

2.6.1 MAGNETIC TIPS

Magnetic tips were created by evaporating a magnetic layer onto quartz tips with the aspect ratio of 5 and the diameter of roughly 40 nm, which were fabricated using a commercial laser-pulling system (Sutter Instrument, P-2000). Using a thermal evaporator, a 25 nm layer of cobalt–iron was deposited on the side of the pulled quartz tip. A 5 nm chrome layer was then evaporated, which serves as a capping layer to prevent oxidation of the magnetic material. These tips result in magnetic field gradients of roughly 1 G/nm at distances of roughly 100 nm.

2.6.2 COMBINED AFM AND CONFOCAL MICROSCOPE

Two stacks of piezo coarse positioners and scanners (Attocube ANPxyz101/RES ANSxyz100) are used for positioning a magnetic tip and a bulk diamond sample containing NV centers. NV centers are placed at the focus of a confocal microscope using one set of piezo scanners (XYZ1), while the tip's distance to the sample is regulated via AFM feedback on the other set of stacks (XYZ2). Atomic force detection is done electrically by measuring changes in the resonant frequency of an oscillating tuning-fork operating in shear mode. The tip can be
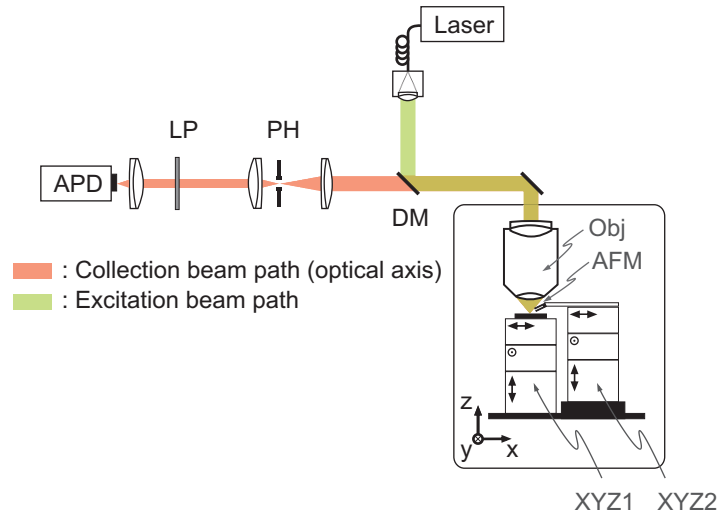
Figure 2.6.2: Combined AFM and confocal microscope.

scanned using XYZ2 to produce magnetic resonance images, while NV spins on the sample are read out confocally. A green excitation laser (532 nm wavelength) is focused on the NV centers using a long working distance objective (Mitutoyo, M Plan Apo NIR 100X) and excites NV centers non-resonantly, which then fluoresce at longer wavelengths. An acousto-optical modulator (not illustrated), is used to pulse the laser allowing for measuring the time-dependent fluorescence of NV centers. A dichroic mirror (DM) separates the collection and excitation laser paths to avoid unwanted photon counts from the excitation laser. Emitted light passes through a telescope containing a pinhole (PH), making the optical detection confocal. A longpass filter (LP) is used to further suppress green excitation counts before the emitted light is collected via an avalanche photo diode (APD) (Perkins and Elmer, SPCM-AQRH-13).
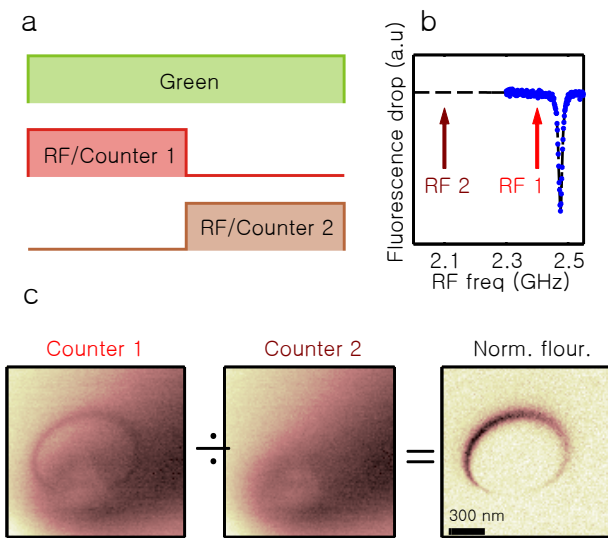
Figure 2.6.3: Normalized fluorescence for magnetic imaging. (a) Pulse sequence for magnetic resonance imaging. (b) The frequency of RF 1 and RF2 relative to ESR frequency of an NV center in the absence of the magnetic tip. (c) Normalization of counter 1 to counter 2 for background-free magnetic image.

2.6.3 Normalized fluorescence for magnetic imaging

This section describes the procedure to acquire background-free magnetic resonance imaging. Figure 2.6.3a is the pulse sequence used in the imaging. Green light is continuously applied to the NV center. For the first half of the sequence, one radio-frequency (RF 1) field is applied, and the corresponding NV counts are collected in counter 1. For the second half of the sequence, the same is done for RF 2 and counter 2. The length of the total sequence is roughly 50 μs, much longer than the spin-pumping time and much shorter than the pixel integration time of our MRI scans. The frequency of RF 1 is tuned close to the NV resonance, while RF 2 is detuned by more than 10 linewidths so that the tip never brings the NV spin into resonance with RF 2 (Fig. 2.6.3b). When a tip is scanned over the sample (same data as Figure 2.2.1c), counts are collected in both counter 1 and counter 2. Counter 1 contains a magnetic contour showing the location where the tip brings the NV into resonance with RF 1 (Fig. 2.6.3c, left panel). However, there are also significant non-magnetic features due to artifacts such as tip shadowing and the influence of topographic features (Fig. 2.6.3c, middle panel). These non-magnetic features can be removed by normalizing counter 1 to counter 2; the latter is affected by the same artifacts as the former but contains no magnetic signal. This normalization results in an image that has only magnetic-field induced fluorescence variations (Fig. 2.6.3c, right panel). We note that by modulating between two RF sources, the overall RF power can be kept constant in time, which is crucial for maintaining AFM performance.

2.6.4 Deconvolution to extract spin-spin distances

A deconvolution process is used to extract the relative distance between NVs from the magnetic contours in Figure 2.3.1 of the main text. As the magnetic response of each NV to the tip is identical, but spatially shifted, we note that images of multiple NV spins are simply the magnetic response of one NV convolved with a map of delta functions corresponding to the spins' relative locations. Thus, we can use deconvolution of the observed magnetic image with

the response of one of the NV spins to retrieve relative spin locations. Doing so requires the point spread function of a single NV spin, which can be found by first measuring the response of a single NV spin before moving to ensemble systems. Alternatively, for ensembles where there is not significant overlap between magnetic resonance curves, one can isolate a single ring and use that as the point-spread function for the deconvolution. We use the latter approach here by manually cropping out data not associated with NV II's magnetic resonance (shown in Fig. 2.3.1a in the main text).

Once the point-spread function of a single spin is determined, deconvolution can be readily performed. Because of finite signal to noise ratios in our data, applying a filter during the deconvolution process is necessary to avoid artificial divergences. We accomplish this by using a Wiener filter, provided in the MATLAB Image Processing Toolbox, which minimizes the contribution from noise at frequencies which have low signal-to-noise ratios (Gonzalez, R. C. & Woods, R. E. Digital Image Processing. (Addison-Wesley Publishing Company, Inc., 1992)). Wiener deconvolution has no free parameters as the optimal amount of filtering is dictated by the noise power spectrum of the image. For NV spin states read out optically, the dominant source of noise is photon shot noise, and consequently, the power spectrum is flat. Thus, the only relevant parameter is the signal to noise ratio of the image, which we find to be 7. Using this value yields the deconvolved image in Figure 2.3.1 which results in an image where each NV spin's location corresponds to a single peak. We note that the peak corresponding to NV I is significantly skewed (as compared to NV III) because that NV lies at a different depth (15 nm further into the surface) than NV II, which slightly modifies its response to the magnetic tip. In principle, to deconvolve spins separated in three dimensions it is necessary to perform a deconvolution on the three-dimensional response of the NV spins to the tip. For this work, because spins are separated laterally more than in the z-direction, this is unnecessary for measuring relative spin distances.

Performing deconvolution is more involved if NV spins in an ensemble are not identically oriented. In bulk diamond, there are four possible quantization axes

for NV centers, dictated by the crystallographic vector connecting the nitrogen atom and neighboring carbon vacancy. As spins' resonant frequencies predominantly shift to energies along their quantization axes, up to four different magnetic responses can be observed upon scanning arbitrary NV spin ensembles with a magnetic tip. While simple deconvolution can be used to find the relative distances between spins sharing an axis in the ensemble, finding the relative distances between the four NV types requires additional consideration.

One method for measuring the distance between NV spins of different axes is to magnetize the tip-field to be perpendicular to the diamond surface, which for cylindrical tip geometries will yield a cylindrically symmetric magnetic field. Then for $[001]$ diamond crystals, where all four NV axes have the same projection along the z-direction, the tip induces an identical, but rotated, magnetic response from each NV axis direction. Thus deconvolution can again be performed after rotating the magnetic response by 90, 180, or 270 degrees depending on the NV axis. Alternatively, for tips without cylindrical symmetry, the sample can be rotated in 900 increments to have each NV direction respond identically to the tip. Relative distances between these four measurements can be determined by using AFM topography, which should not change upon rotation of the sample and can thus be used to correlate the magnetic measurements. Additionally, this technical challenge is unique to spins associated with NV centers, where the quantization is defined by a zero-field splitting along a crystallographic vector. For many other systems, the quantization axis for spins can be dictated by an externally applied field, and consequently all spins will respond identically to the local tip field.

2.6.5   Theoretical NV coupling for the measured NV locations

NVs I, II, and III (Fig. 2.3.1), are plotted in real space with the relative distances extracted through our scanning-magnetic field gradient imaging. Arrows indicate the NV orientation determined by measuring the Zeeman splitting along different directions with a three-axis Helmholtz coil (data not shown). All three
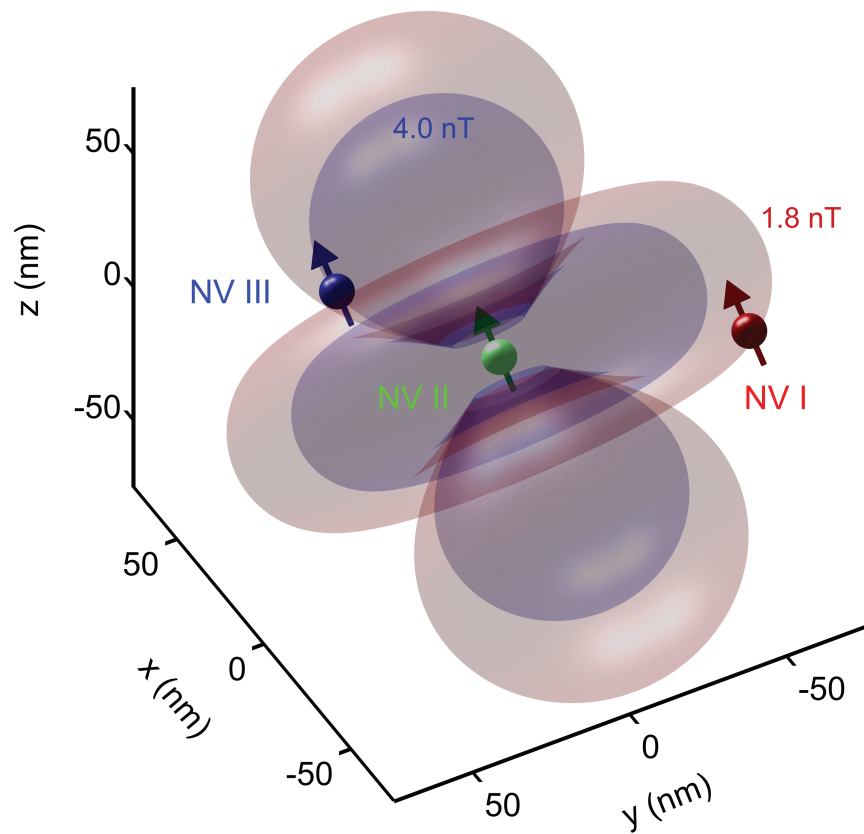
Figure 2.6.4: Theoretical NV coupling for the measured NV locations.
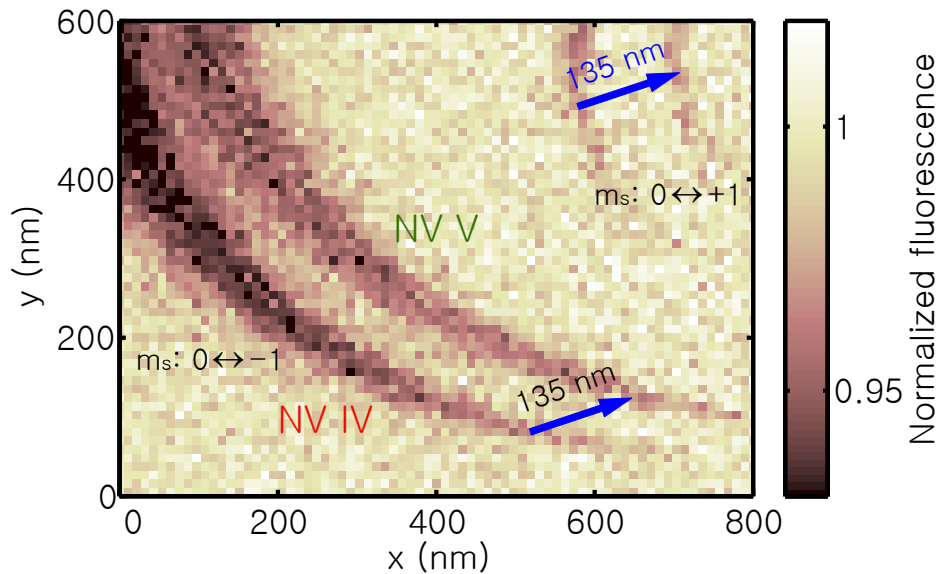
Figure 2.6.5: Distance between NV IV and NV V.

NVs have the same NV axis. The dipolar magnetic field strength from NV II along the NV axis is plotted as a function of position. We plot equal field-strength contours that intersect NV I (red) and NV III (blue), yielding their theoretical dipolar coupling strengths of 1.8 nT and 4.0 nT respectively. The shapes of the contours indicate the strong angular dependence of the coupling strength, illustrating the importance of three-dimensional imaging for a priori determination of NV coupling frequencies.

2.6.6   DISTANCE BETWEEN NV IV AND NV V

Analogous to Figure 2.3.1, magnetic imaging is done on NVs IV and V to determine their relative lateral distances. When the tip is scanned over of the pair of NVs, four contours are seen for the two NVs. There are two contours per NV because the tip field is strong compared to the applied static field, which splits the $m_S = -1$ and $m_S = +1$ in the NV triplet ground state. Unlike the imaging done in Figures 2.2.1 and 2.3.1, where the tip is only strong enough to bring one spin

transition into resonance, now the tip can bring either $m_S = -1$ or $m_S = +1$ into resonance with $m_S = 0$, depending on the sign of the field. The distance between NVs is given by the offset of the magnetic contours for the two NVs, which is the same for both spin transitions and is 135 nm (length of blue arrows). We note that this configuration of field-strength and detuning is advantageous in this situation, since the detection of the two ESR transitions ($m_S = 0 \rightarrow m_S = -1$ and $m_S = 0 \rightarrow m_S = 1$) allows for accurately determining both x and y displacements of the NV centers while maintaining a small scan range.

2.6.7   ACTIVE AFM DRIFT CORRECTION

This section describes the active drift correction scheme used to ensure the tip position with few-nm resolution during repetitive NV-control experiments. Figure 2.6.6a shows AFM topographic image of an NV-containing nanostructure (here a triangle). This triangle contains the two NV centers studied in Figures 2.4.1 and 2.4.2 in the main text. Magnetic resonance imaging is performed on the two NV spins, and their magnetic responses are observed in the normalized fluorescence (plotted is the same region as Fig. 2.6.5). In order to achieve coherent control of each of the two spins, it is necessary to position the tip where it splits the two NV resonances and maintain the tip location with few-nm resolution to overcome NV spin-decoherence induced by tip-drifts. Here, we fix the tip at the green marker, but after performing experiments on each NV spin, the tip may have changed location due to temperature-induced drifts or piezo-electric creep. As an example of drifts, whose magnitude is exaggerated here, we examine the situation where the tip has drifted from the green marker to the blue marker. The real-space location of the drifted tip is unknown. To determine its location efficiently, we take a single AFM line-scan which intersects the edge of the AFM triangular structure (green line in Fig. 2.6.6a). In Figure 2.6.6b, we plot the measured line-scan topography (green line), and cross-correlate it to individual lines of a topographic scan of the triangle edge (blue and grey lines). The AFM line yielding the highest cross-correlation (blue
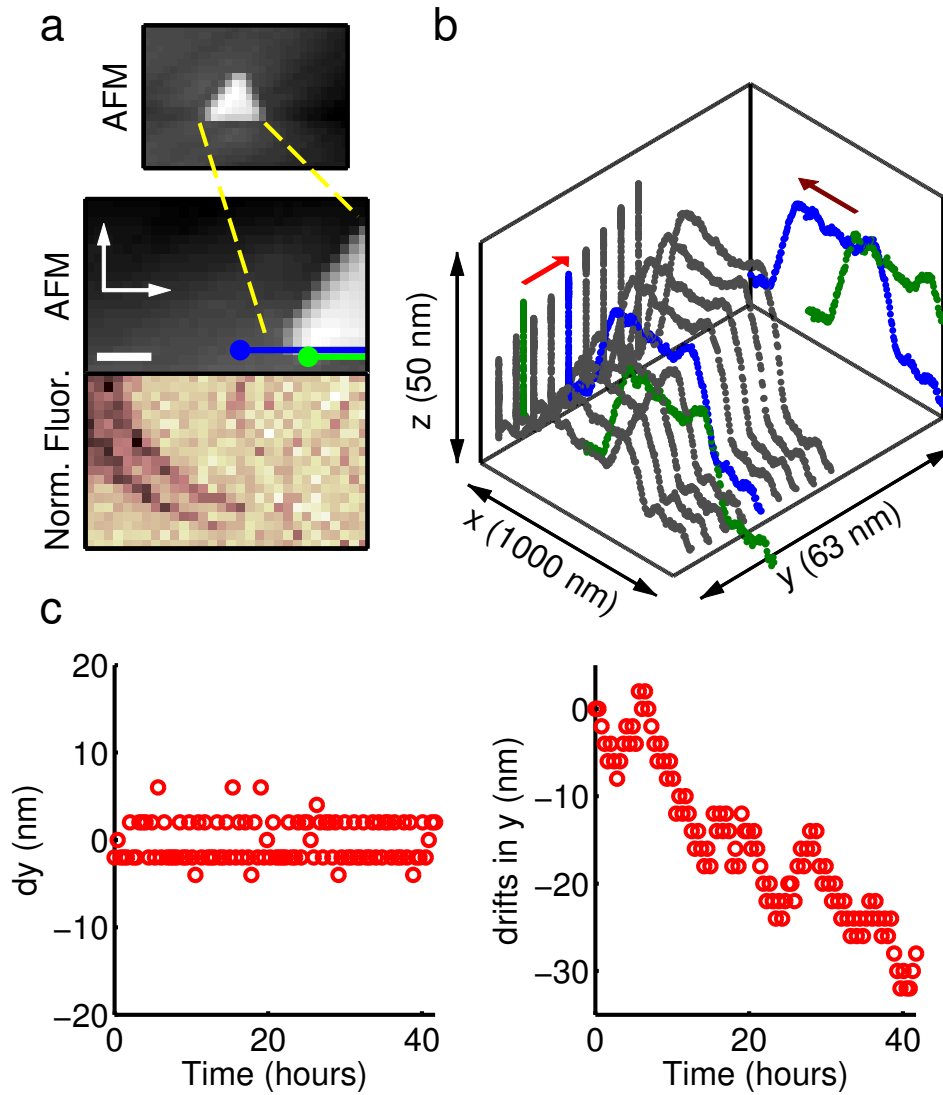
Figure 2.6.6: Active AFM drift correction. (a) AFM topographic image of an NV-containing nanostructure. (b) Lateral positioning feedback via line-scan correction. (c) Lateral positioning feedback performance.

line), measures the tip's drift in the y-direction (dy). Drifts in the x-direction (dx) can additionally be extracted from the spatial offset between the green and blue panels, which is given by the location of the peak in the performed cross-correlation. Positioning is performed intermittently, and the resulting drifts in the y-direction (dy) are plotted (Fig. 2.6.6c, left panel). Magnetic field-gradients are predominantly directed along the y-direction (measured from the MRI image of the NVs in Fig. 2.6.5), and consequently achieving high-precision in y-positioning is necessary for maintaining the NV spins resonance. Here we show positioning can be achieved with a standard deviation of 2.3 nm, only limited by pixelation of the topographic data. Spatial variations can then be converted to spectral uncertainties using the measured magnetic field gradient of our tip (0.1 G/nm here), indicating that the magnetic resonance can be maintained with 500 kHz precision. This sets a limit for tip-drift induced decoherence of NV spins which is smaller than the inhomogeneous dephasing rate $(1/T_2^*)$ of the NV spins studied here. Integrating the measured drifts between line-scans gives the overall tip motion (Fig. 2.6.6c, right panel), which indicate that the tip location would drift considerably more without the use of line-scan feedback.

2.6.8 Ramsey free-induction decay measurements

The Ramsey free-induction decay measurements in Fig. 2.4.1 are taken with the radiofrequency driving field detuned by 5 MHz from the target NV center's nominal ESR frequency in the presence of the magnetic tip; the observed oscillations are due to beating of this detuning with the ^{15}N hyperfine splitting (3.1 MHz). The measured Ramsey data are fitted to the sum of two exponentially damped sinusoids, whose phases are fixed by the relative strength between the net detuning (the radiofrequency field detuning plus or minus half the hyperfine splitting) and the Rabi frequency (5.5 MHz), governed by the strength of the applied radiofrequency field.

3

A robust scanning diamond sensor for nanoscale imaging with single nitrogen-vacancy centers

3.1 INTRODUCTION

The nitrogen-vacancy (NV) defect center in diamond has potential applications in nanoscale electric and magnetic field sensing [5, 22, 25, 70, 95], single-photon microscopy [18, 91], quantum information processing [76], and bioimaging [71]. These applications rely on the ability to position a single NV center within a few nanometers of a sample, and then scan it across the sample surface, while preserving the center's spin coherence time and readout fidelity. However, existing scanning techniques, which use a single diamond nanocrystal

grafted onto the tip of a scanning probe microscope [5, 18, 55, 87], suffer from short spin coherence times due to poor crystal quality, and from inefficient far-field collection of the fluorescence from the nitrogen-vacancy center, Here, we demonstrate a robust method for scanning a single NV center within tens of nanometers from a sample surface that addresses both of these concerns. This is achieved by positioning a single NV center at the end of a high-purity diamond nanopillar, which we use as the tip of an atomic force microscope. Our approach ensures long NV spin coherence times ($75\ \mu$s), enhanced collection efficiencies of NV fluorescence due to waveguiding, and mechanical robustness of the device (several weeks of scanning time). We are able to image magnetic domains with width of 25 nm, and demonstrate a magnetic field sensitivity of 56 nT/$\sqrt{\text{Hz}}$ at a frequency of 33 kHz, which is unprecedented for scanning NV centers.

NV-based nanoscale sensing is possible because the NV center forms a bright and stable single-photon source [56] for optical imaging, and has a spin-triplet ground state that offers excellent magnetic [70] and electric [25] field sensing capabilities. The remarkable performance of the NV center in such spin-based sensing schemes, is the result of the long NV spin coherence time [6], combined with efficient optical spin preparation and readout [41]. These properties persist from cryogenic temperatures to ambient conditions, which distinguishes the NV center from other systems proposed as quantum sensors such as single molecules [72], or quantum dots [16].

Reducing the distance between the NV center and the sample of interest is crucial for improving spatial resolution. Past experiments aimed at implementing scanning NV microscopes were focused on grafting diamond nanocrystals onto scanning probe tips [5, 18]. Although used successfully in the past, this approach suffers from the poor sensing performance of nanocrystal-based NV centers, for which the spin coherence times are typically orders of magnitude shorter than for NVs in bulk diamond [70]. Here, we present a novel approach that overcomes these drawbacks and thereby realizes the full potential of bulk NV-based sensing schemes in the scanning geometry relevant for nanoscale imaging. In particular, we have developed a monolithic 'scanning NV sensor' (Fig. 3.2.1 a), which uses a

diamond nanopillar as the scanning probe, with an individual NV center artificially created within 10 nm of the pillar tip through ion implantation [50]. Long NV spin coherence times are achieved as our devices are fabricated from high-purity, single-crystalline bulk diamond, which brings the additional advantage of high mechanical robustness. Furthermore, diamond nanopillars are efficient waveguides for the NV fluorescence band [4], which for a scanning NV device yields record-high NV signal collection efficiencies.

3.2 EXPERIMENTAL SET-UP AND DEVICE FABRICATION FOR THE SCAN-NING NV SENSOR

Figure 3.2.1b shows a representative scanning electron microscope (SEM) image of a single-crystalline diamond scanning probe containing a single NV center within 10 nm of its tip. To prepare such devices, a series of fabrication steps are performed sequentially, including low-energy ion implantation for NV creation, several successively aligned electron-beam lithography steps and reactive ion etching [45]. An essential element to this sequence is the fabrication of micrometer-thin, single-crystalline diamond slabs that form the basis of the scanning probe device shown in Fig. 3.2.1b. A detailed description of the fabrication procedure of these slabs and the resulting devices can be found in the Supplementary section 3.7.1. Our scanning diamond nanopillars have typical diameters of 200 nm and lengths of 1 µm and are fabricated on few-micrometer-sized diamond platforms that are individually attached to atomic force microscope (AFM) tips for scanning (see Fig. 3.2.1b and Supp. 3.7.1 for details of the attaching process). Our fabrication procedure (Fig. 3.2.1c) allows for highly parallel processing, as shown in the array of diamond devices depicted in the SEM image in Fig. 3.2.1d. Close to 30% of the diamond nanopillars in our samples contain single, negatively charged NV centers. Other devices contain more than one NV, or one NV in a charge-neutral state, which is unsuitable for magnetometry. From these 30%, we select the NV centers that exhibit the highest
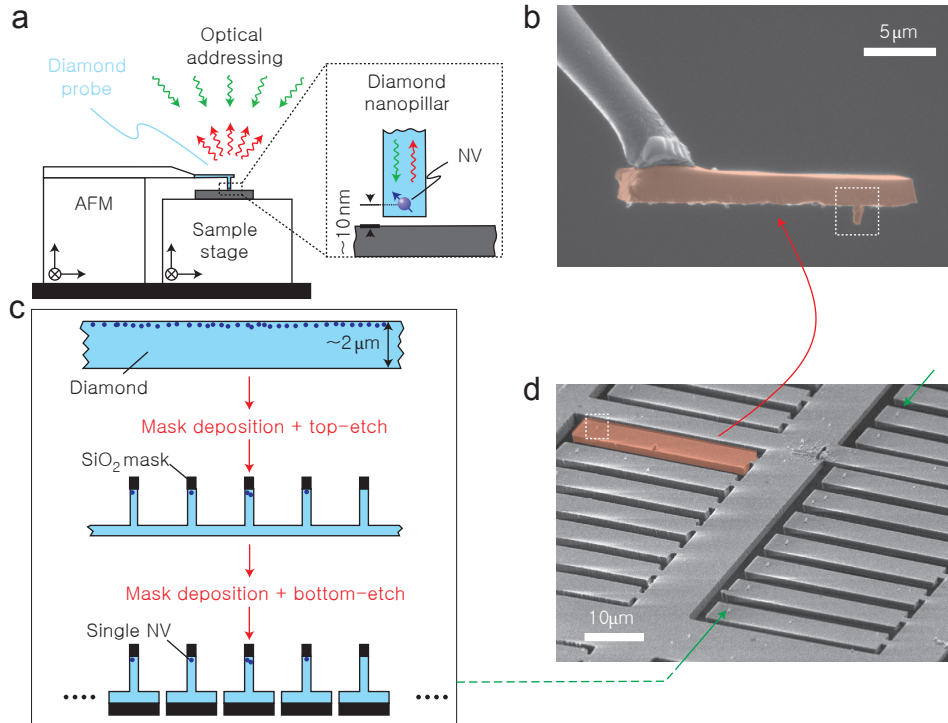
Figure 3.2.1: Experimental set-up and probe fabrication for the scanning NV sensor. (a) Schematic of the set-up, consisting of a combined optical and atomic force microscope (AFM). We use a 532 nm laser (green arrows) to address the scanning NV center through its red fluorescence (red arrows). The scanning NV center resides in a diamond nanopillar (inset) and its proximity to the sample is maintained by means of AFM feedback. (b) SEM image of a single-crystalline diamond nanopillar probe (false color coded in red) with a single NV center in its tip (see Fig. 3.3.1). (c) Brief depiction of the fabrication process for scanning single-crystalline diamond NV sensors. Electron-beam lithography is used to define nanopillars and platforms from the top and bottom sides of a few-micrometer thin diamond membrane. Patterns are then transferred to the diamond by reactive ion etching. (d) SEM image of a finalized array of diamond platforms with nanopillars. In all panels, dotted rectangles highlight diamond nanopillars.

photon count rates and longest spin coherence times and mount these single-NV nanopillars onto AFM tips to yield the finalized scanning probe shown in the SEM picture in Fig. 3.2.1b. We note that these scanning devices were fabricated from a [001]-oriented diamond crystal, resulting in NV orientation and magnetic-field sensing along an axis tilted by 54.7° from the nanopillar direction.

To use the scanning NV sensor and characterize its basic spin and optical properties, we used a combined confocal and atomic force microscope as sketched in Fig. 3.2.1a. The set-up was equipped with piezo positioners for the sample and an AFM head to allow for independent scanning with respect to the optical axis. Optical addressing and readout of the NV center was performed through a long-working-distance microscope objective (numerical aperture, NA = 0.7). Microwave radiation for coherent NV spin manipulation was applied using a gold bonding wire attached in proximity to the NV center (see Supp. 3.7.2).

3.3 CHARACTERISTICS OF A SINGLE NV CENTER IN A SCANNING DIAMOND NANOPILLAR

Figure 3.3.1a shows a confocal scan under green laser illumination (excitation wavelength, 532 nm) of a typical single scanning NV device. The bright photon emission emerging from the nanopillar (white circle) originates from a single NV center, as indicated by the pronounced dip in the photon-autocorrelation measurement (Fig. 3.3.1b) and the characteristic signature of optically detected NV electron-spin resonance (ESR) [41] (Fig. 3.3.1c), all obtained on the same device. Importantly, we confirm that photon waveguiding through the nanopillar [4] persists despite the close proximity of the NV to the tip of our fabricated nanopillar devices. For example, the data in Fig. 3.3.1c were obtained at 100 μW excitation power and demonstrate single NV counts approaching $2.2 \cdot 10^5$ counts per second (c.p.s.)—an approximately fivefold increase in detected fluorescence intensity compared to an NV observed under similar
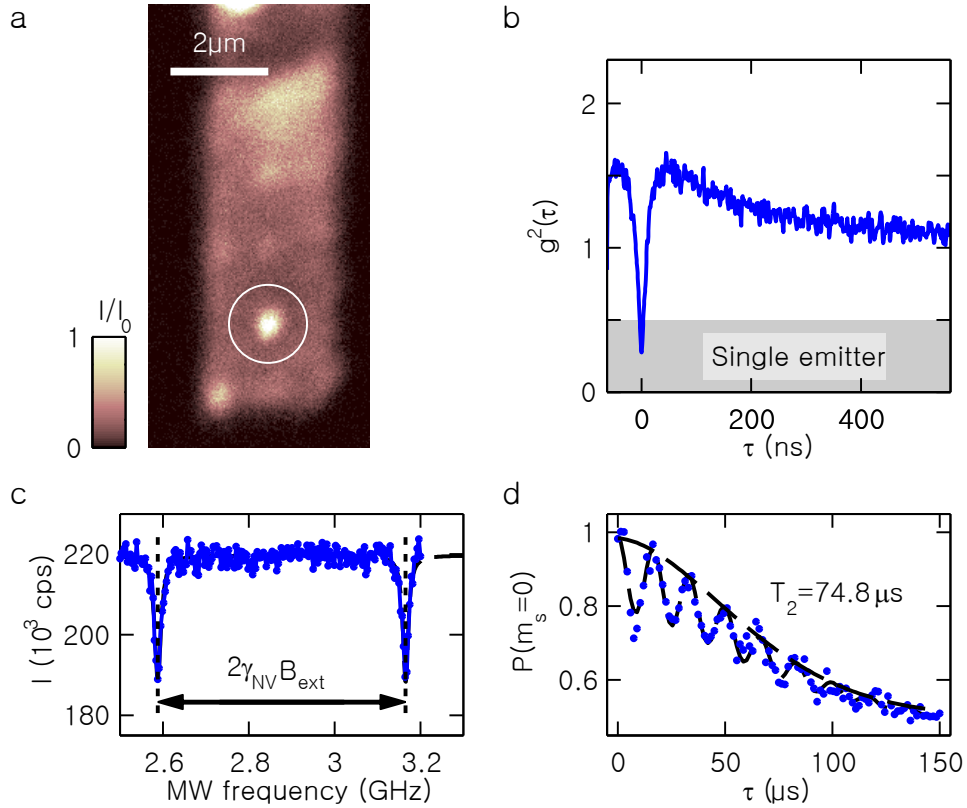
Figure 3.3.1: A single NV center in a scanning diamond nanopillar. (a) Confocal image of red fluorescence from a single-crystalline diamond probe (see side view SEM image in Fig. 3.2.1b). Fluorescence counts are normalized to $I_o = 1.5 \cdot 10^5$ c.p.s. The encircled bright feature stems from fluorescence of a single NV center in the nanopillar. b, Photon autocorrelation measurement ($g_2(\tau)$) for NV fluorescence in the scanning nanopillar device. Data with $g_2 < 0.5$ (grey-shaded region) demonstrate the presence of a single photon emitter in the nanopillar. (c) Optically detected ESR identifies the single emitter in the nanopillar as an NV center. The two possible NV spin transitions [41] are split by the NV electron Zeeman splitting $2\gamma_{NV}B_{NV}$, where γ_{NV} = 2.8 MHz/ G is the NV gyromagnetic ratio and B_{NV} is the magnetic field along the NV axis (here, B_{NV} 103 G). (d) Spin-echo measurement for the NV center in the diamond nanopillar device. The envelope fitted to the characteristic NV spin-echo decay (see Supp. 3.7.3) yields the NV spin coherence time of T_2 = 74.8 μs. Data in panels b–d were all taken on the same device. Green excitation power: 100 μW in b–d, and 400 μW in a.

conditions in an unpatterned diamond sample. We thus significantly increase the fluorescence signal strength from the scanning NV and at the same time minimize exposure of the samples to green excitation light, which is especially relevant for possible biological or low-temperature applications of the scanning NV sensor. Using well-established techniques for coherent NV-spin-manipulation [49], we characterized the spin-coherence time, T_2, of the same NV center studied so far. Spin-coherence sets the NV sensitivity to magnetic fields and limits the number of coherent operations that can be performed on an NV spin; it is therefore an essential figure of merit for applications in magnetic field imaging [95] and quantum information processing [76]. Using a Hahn-echo pulse sequence, we measured the characteristic single NV coherence decay [98] shown in Fig. 3.3.1d; from the decay envelope we deduce a spin coherence time of $T_2 = 74.8\,\mu$s. We note that this T_2-time is consistent [95] with the density of implanted nitrogen ions $(3 \cdot 10^{11}\,\text{cm}^{-2})$ and conclude that our device fabrication procedure fully preserves NV spin coherence. Combining measurements of the T_2-time with the fluorescence count rate and NV spin readout contrast as obtained in Fig. 3.3.1, we obtain a maximal 'AC' magnetic field sensitivity [95] of $56\,\text{nT}/\sqrt{\text{Hz}}$ at a frequency of 33 kHz and (based on data in Fig. 3.3.1c) and a 'DC' sensitivity of $6.0\,\mu\text{T}/\sqrt{\text{Hz}}$. We note that both 'AC' and 'DC' magnetic field sensitivities could be further improved by using spin-decoupling sequences [20] and optimized parameters for spin-readout [27], respectively.

3.4 NANOSCALE MAGNETIC FIELD IMAGING WITH THE SCANNING NV SENSOR

To characterize the resolving power of the scanning NV sensor, we imaged a nanoscale magnetic memory medium consisting of bit-tracks of alternating (out-of-plane) magnetization with various bit-sizes. Figure 3.4.1 illustrates our method and results. The scanning NV sensor operated in a mode that imaged contours of constant magnetic field strength (B_{NV}) along the NV axis through the continuous monitoring of red NV fluorescence, in the presence of an ESR

driving field of fixed frequency ω_{MW} and typical magnitude $B_{MW} \approx 2$ G (as determined from NV Rabi oscillations (not shown)). We detuned ω_{MW} by δ_{MW} from the bare NV spin transition frequency, ω_{NV}, but local magnetic fields due to the sample changed this detuning during image acquisition. In particular, when local fields brought the spin transition of the NV into resonance with ω_{MW}, we observed a drop in NV fluorescence rate, which in the image yielded a contour of constant $B_{NV} = \delta_{MW}/\gamma_{NV}$, with $\gamma_{NV} = 2.8$ MHz/G being the NV gyromagnetic ratio. We simultaneously acquired two such images by applying sidebands to ω_{NV} with $\delta_{MW} = \pm 10$ MHz (dark and bright arrows in Fig. 3.4.1c). Normalization of the pixel values in the two data sets then directly provided a map of magnetic field contours with positive and negative values of B_{NV} (here, with $B_{NV} = \pm 3$ G) and at the same time helped to reject low-frequency noise. Fig. 3.4.1a shows a resulting scanning NV magnetometry image of two stripes of magnetic bits (indicated by the white dashed lines) with bit-spacings of 170 nm and 65 nm. The shape of the observed domains is well reproduced by calculating the response of the NV magnetometer to an idealized sample with rectangular magnetic domains of dimensions corresponding to the written tracks (Fig. 3.4.1e and Supp. 3.7.4).

The spatial resolution of an NV magnetometer is affected by the distance of the NV center to the sample. Therefore, approaching the NV sensor more closely to the magnetic sample revealed magnetic bits with average sizes of ≈ 38 nm, as shown in Fig. 3.4.1b. We note that in this image, due to the large field gradients generated at the boundaries between domains, we could observe transitions between magnetic field lines on length-scales of ≈ 3 nm (full width at half maximum of the line-cut in Fig. 3.4.1d). An even further decrease of NV-sample distance allowed us to image yet smaller domains, ≈ 25 nm in width (Fig. 3.4.1f), but with a reduced imaging contrast caused by strong magnetic fields transverse to the NV axis, which occur in close vicinity to the sample's surface [57] (see Supp. 3.7.5). One of the disadvantages of using a hard drive to characterize our tip is that the local magnetic fields are very large and exceed the

Figure 3.4.1: Nanoscale magnetic field imaging with the scanning NV sensor. (a) NV magnetic field image of bit-tracks on a magnetic memory, highlighted by dashed white lines. We plotted normalized data, $I_{\mathrm{norm}} = I_{\mathrm{MW,1}}/I_{\mathrm{MW,2}}$ (see text and (c)), to reveal magnetic field lines corresponding to $B_{\mathrm{NV}} = \pm 3$ G (see inset in a). Additionally, a bias magnetic field of $B_{\mathrm{MW}} \approx 52$ G was applied to determine the sign of the measured magnetic fields. (b) Magnetic image obtained as in a, but with the NV-sample distance decreased by an estimated 50 nm. Bringing the NV closer to the sample increases the magnetic field magnitude at the NV sensor, and improves the imaging spatial resolution, allowing us to image magnetic bits, ≈ 38 nm in width. Approximate NV-sample distances are noted in the schematics illustrating the experimental configuration, with the sensing NV center fixed on the optical axis and the magnetic sample scanned below the pillar. Total image acquisition times were 11.2 minutes (50 ms/pixel) for a, and 12.5 minutes (75 ms/pixel) for data in b, with laser powers of 130 μW. The color bar applies to a and b. (c) Optically detected ESR of the sensing NV center. For magnetic field imaging, we modulate an applied microwave field between two frequencies ($\omega_{\mathrm{MW,1}} = 2.766$ GHz and $\omega_{\mathrm{MW,2}} = 2.786$ GHz) and collect NV fluorescence counts ($I_{\mathrm{MW,1}}$ and $I_{\mathrm{MW,2}}$, respectively) in synchrony with the microwave modulation. (d) Line-cut along the white line indicated in b (averaged across six adjacent pixels) indicating the sensor's ability to spatially distinguish magnetic field lines separated by ≈ 3 nm (limited by the local magnetic field gradient). (e) Calculated NV response for the experimental situation in a, assuming a simplified magnetic sample (see Supp. 3.7.4) (f) Magnetic image as in a and b for a different experimental realization. Here, due to a further decrease in the NV-sample distance, the smallest observed domains have average sizes of 25 nm as determined for the six domains found in the 150 nm interval marked by the blue arrows. The reduced imaging contrast in f results from the close proximity of the NV to the sample (see text).

Figure 3.4.1 *(Continued)*

a

~ 70 nm

b

~ 30 nm

I_{norm} (%): 90 — 110

B_{NV}
— : −3G
— : +3G

200 nm

100 nm

c

I/I_0 (2%/div)

$\omega_{MW,1}$ $\omega_{MW,2}$

2.75 ω_{MW} (GHz)   2.8

d

I_{norm} (5%/div)

3 nm

10 nm

x"

e

model

200 nm

f

I_{norm} (%): 98 — 103

150 nm
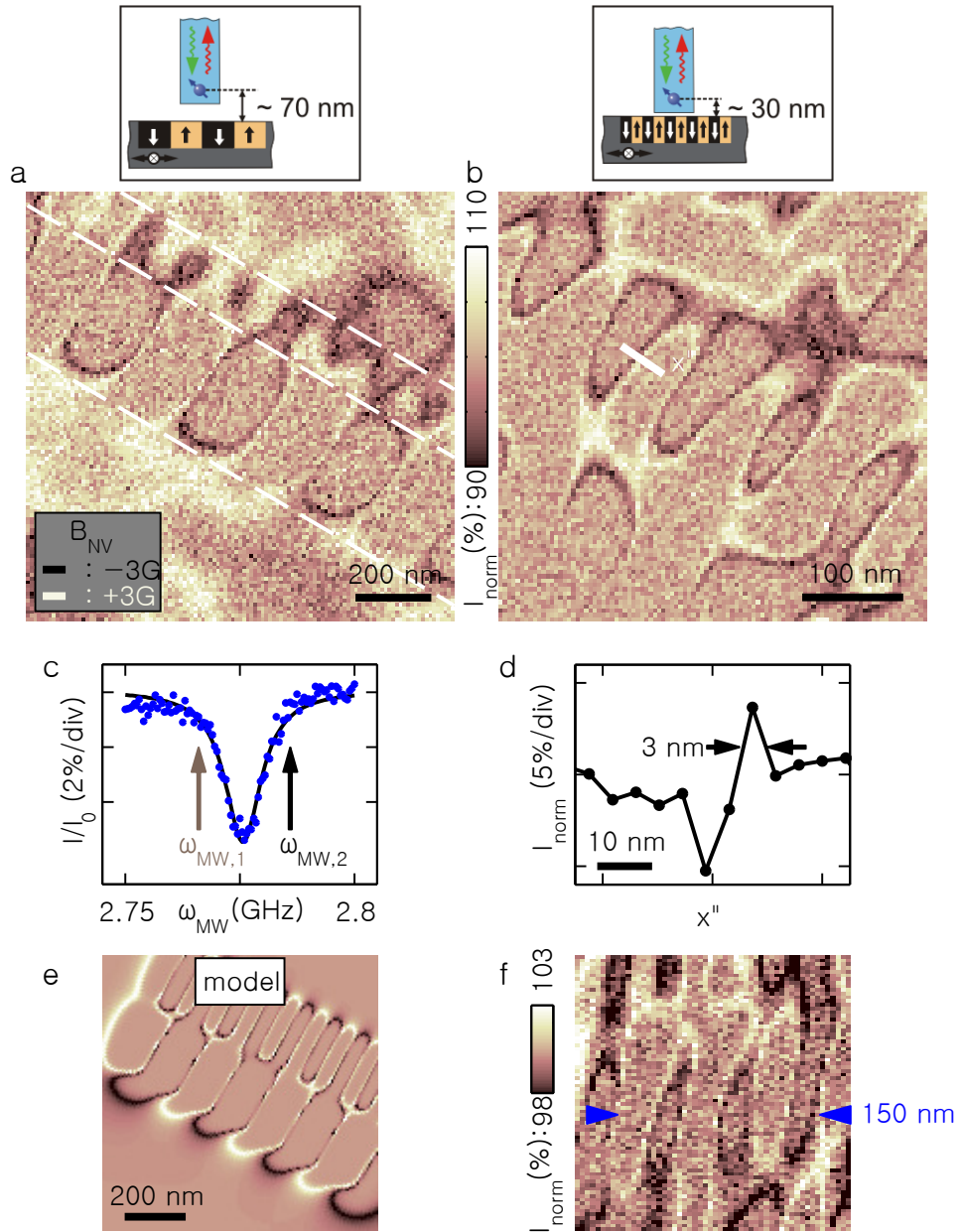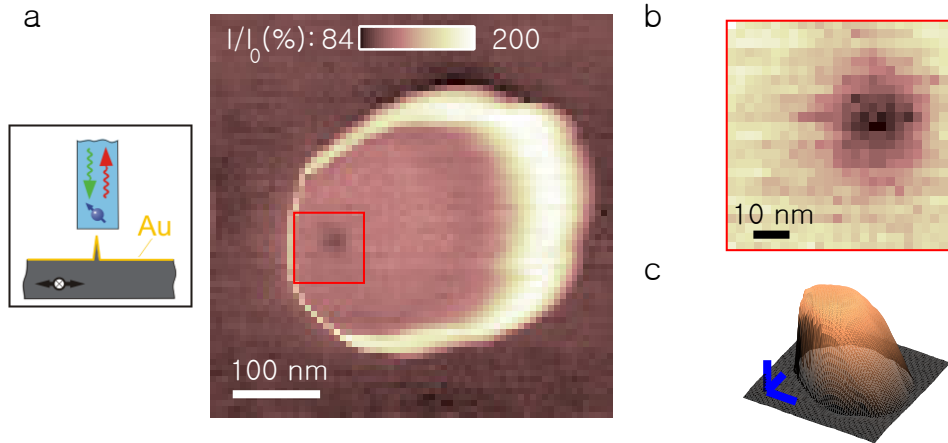
Figure 3.5.1: Nanoscale fluorescence quenching imaging of the scanning NV sensor. (a) Scanning the diamond pillar over a sharp metallic tip leads to a bright, circular feature due to sample-topography (see Supp. 3.7.8). Positioning the metallic tip exactly at the location of the NV center (red square), however, yields a sharp dip in NV fluorescence. The illustration shows the experimental configuration used in this experiment. (b) Zoomed-in image of the red square region in a. The observed fluorescence quenching dip has a spatial resolution ≈ 20nm. (c) AFM topography image obtained simultaneously with the data in b. Blue scale bars represent 100 nm displacement in all directions. Image acquisition times were 30 minutes (320 ms/pixel) and 2.7 minutes (250 ms/pixel) in a and b, respectively at laser power of 35 μW.

typical dynamic range of our technique. However, such experiments provide valuable information regarding NV-sample distance, and consequently the spatial resolution achieved in imaging. In particular, we estimate the distance between the scanning NV and the sample to be comparable to 25 nm, based on the smallest magnetic domain-sizes we observed.

3.5 DETERMINING THE LOCATION OF A SINGLE NV CENTER IN A DIAMOND NANOPILLAR

To independently verify the NV's proximity to the diamond surface, we have conducted a measurement where we scanned a sharp metallic tip ($<$ 20 nm in

diameter, see schematic in Fig. 3.5.1a and Supp. 3.7.7) over the NV-containing pillar to image the NV's location. The imaging contrast consisted of the detected NV fluorescence in the far-field changing when the NV was in close proximity to the metallic tip [12]. Owing to the strong dependence of NV fluorescence rate on the distance between the NV and the metallic sample [12] (here, due to partial fluorescence quenching and local modifications of excitation light intensity), we could use this technique to precisely locate the position of the NV center within the diamond nanopillar. The resulting data (Fig. 3.5.1a) showed signatures of the topography of the scanning diamond nanopillar (bright ring in the NV fluorescence signal, see Supp. 3.7.8 for details). More importantly, however, while the front-end of the diamond probe scanned over sharp metallic tip, we observed a dip in NV fluorescence (red square in Fig. 3.5.1a and zoomed image in Fig. 3.5.1b) when the metallic tip was positioned at the location of the NV center. This feature is not accompanied by any topographic features and is thus attributed to partial quenching of NV fluorescence due to the sharp metallic tip (see Fig. 3.5.1c and Supp. 3.7.8). The Gaussian width (double standard deviation) of 25.8 nm of this fluorescence quenching spot was likely still limited by the size of the metallic tip and therefore marks an upper bound to our ability to localize the NV center within the pillar. Importantly, such data allow us to find the position of the single NV center with respect to the topography of our device (Fig. 3.5.1c), which will greatly facilitate precise alignment of our sensing NV center with respect to (magnetic) targets in future sensing and imaging applications.

3.6   DISCUSSION AND OUTLOOK

The biggest remaining uncertainty to the distance between the scanning NV center and the sample is vertical straggle in the NV implantation process, which is still poorly understood [97]. Naturally occurring, stable NV centers have been observed as close as 3 nm from diamond surfaces [11] and thus future advances in the controlled creation of NV centers [82] should allow us to further improve NV-sample distance and therefore spatial resolution in scanning NV imaging by

about one order of magnitude. Additionally, the coherence properties of artificially created NV centers close to the diamond surface could be further improved by appropriate annealing techniques [75] or dynamical decoupling [20] which would both significantly improve the magnetic sensing capabilities of the scanning NVs. We note that for magnetic field imaging, our current ability to resolve individual magnetic domains already equals the typical performance of alternative methods [54, 100], with the added advantages of being non-invasive and quantitative.

The magnetic field sensitivity we demonstrated here with the scanning NV sensor compares well to the performance realized previously with single NV centers in ultrapure, bulk diamond samples [70]. Additionally, the mechanical robustness and durability of our diamond probes (up to several weeks of scanning with the same tip) illustrate the advantage of our method over alternative approaches to scanning NV magnetometry [5, 18]. Compared to other physical systems used for nanoscale magnetic imaging, NV centers in monolithic diamond scanning probes stand out due to the excellent photostability of the NVs, the possibility of room temperature operation and the chemical inertness of diamond, which allow for magnetometry operation even under harsh environmental conditions. To conclude, we note that the scope of applications of our scanning NV probe extends far beyond magnetic imaging. For example, our devices are ideally suited to use as an optical sensors [72, 91] and form an interesting platform to coherently couple the scanning NV spin to other spin systems such as phosphorus in silicon [51], other NV centers, or carbon-based spin qubits [85]. Quantum information could thereby be transferred between a stationary qubit and our scanning NV center, and from there to single photons [96] or other qubit systems such as long-lived nuclear spin qubits in the diamond matrix.

3.7 Supplementary section

3.7.1 Diamond tip fabrication

Devices were fabricated from a sample of high purity, single crystalline diamond (Element Six, electronic grade diamond, < 5 ppb nitrogen; thickness 50 μm). We implanted the sample with atomic nitrogen at an energy and density of 6 keV and $3 \cdot 10^{11}$ cm^{-2} (leading to a nominal mean NV depth of $\approx$ 10 nm). Subsequent annealing at 800°C for two hours yielded a shallow layer of NV centers with a density of $\approx$ 25 NVs/μm^2 and a depth of $\approx$ 10 nm. We then etched the sample from the non-implanted side to a thickness of $\approx$ 3 μm using reactive ion etching (RIE, Unaxis shuttleline). We employed a cyclic etching recipe consisting of a 10 min Ar/Cl$_2$ [60] etch, followed by 30 min of O$_2$ [45] etching and a cooling step of 15 min. This sequence was essential to maintain the integrity of the diamond surface during the few-hour etching time. On the resulting thin diamond membrane, we fabricated an array of diamond nanopillars on the top side by using electron-beam lithography and RIE as described previously [45]. Next, we performed a second lithography step on the back-side of the diamond slab, which defined platforms to hold the diamond nanopillars. A final RIE process transferred the resist pattern to the sample, and fully cut through the diamond membrane to yield in the structure shown in Fig. 3.2.1d.

To mount a pre-selected diamond platform on an AFM tip, we used a focused ion beam (FIB) system (Zeiss NVision 40) equipped with a nanomanipulator (Omniprobe AutoProbe 300) and ion-assisted metal deposition. We used tungsten deposition or SEM-compatible glue (SEMGLU, Kleindiek) to attach a diamond platform to a quartz AFM tip and then used FIB cutting to release the diamond platform from the bulk. With a properly aligned FIB, this process does not contaminate the scanning diamond nanopillar, and yields a NV/AFM probe as shown in Fig. 3.2.1b.

3.7.2 Combined confocal and atomic-force microscope

We used a homebuilt microscope combining optical (confocal) imaging and AFM. The optical microscope was based on a long working-distance microscope objective (Mitutoyo ULWD HR NIR 100x, 0.7NA). The AFM was tuning-fork based, controlled using commercial electronics (Attocube ASC500) and mounted using a home-built AFM head. Both the sample and the AFM head were fixed on three-axis coarse and fine positioning units (Attocube ANPxyz101 and ANSxyz100, respectively) to allow positioning of the diamond tip with respect to the fixed optical axis and subsequent scanning of the sample with respect to the diamond probe.

Optical excitation of the NV center was performed using a diode-pumped solid-state laser (LaserGlow LRS-0532-PFM-00100-01) at a wavelength of 532 nm. Pulsed excitation for coherent NV spin manipulation used a double-pass acousto-optical modulator (AOM) setup (Isomet, AOM 1250C-848). ESR was driven with a microwave generator (Rhode Schwartz, SMB100A) and amplifier (MiniCircuits, ZHL-42W). The microwave field was delivered to the NV center through a gold bonding-wire (25 μm diameter) which was mounted as a short-cut termination to a semi-rigid coaxial cable. The wire was brought in close proximity ($\approx$ 50 μm) to the scanning NV to minimize the required microwave power. Both the microwave source and the AOM were timed using a computer-controlled trigger-card (Spincore, PulseBlasterESR-PRO-400).

3.7.3 Fit to spin-echo data.

To obtain the NV T_2-time form the spin-echo measurement presented in Fig. 3.3.1d, we fitted the data to a sum of gaussian peaks, modulated by a decay envelope $\propto \exp[-(\tau/T_2)^n]$, i.e., we employed the fit-function [17]

$$\exp[-(\tau/T_2)^n] \sum_j \exp[-((\tau - j\tau_{\text{rev}})/T_{\text{dec}})^2]. \qquad (3.1)$$

Taking T_2, n, τ_{rev} and T_{dec} as free fitting parameters, we found
$T_2 = 74.8 \pm 4.3\ \mu s$, $n = 1.7 \pm 0.2$, $\tau_{\text{rev}} = 16.7 \pm 0.1\ \mu s$ and $T_{\text{dec}} = 7.6 \pm 0.2\ \mu s$
for the data shown in Fig. 3.3.1d (errors indicate 95% confidence intervals for the
nonlinear least squares parameter estimates).

3.7.4 SIMULATION OF MAGNETIC IMAGES

In order to reproduce the magnetic images obtained with the scanning NV
sensor, we performed a model-calculation of the local magnetic fields in
proximity to the hard-disc sample we imaged in our experiment. The magnetic
domains were approximated by an array of current-loops in the sample-plane as
illustrated in Fig. 3.7.1a. We chose the sizes of the loops to match the nominal
size of the magnetic bits on the sample (bit-with 200 nm and bit-length 125 nm
and 50 nm for the tracks in the figure) and set the current to 1 mA (corresponding
to a density of ≈ 1 Bohr magneton per $(0.1\ \text{nm})^2$), which we found to yield the
best qualitative match to the magnetic field strengths observed in the experiment.
We then applied Biot-Savart's law to this current-distribution to obtain the
magnetic field distribution in the half-plane above the sample.

Fig. 3.7.1b shows the resulting magnetic field projection onto the NV center at
a scan height of 50 nm above the current loops. The NV direction was
experimentally determined to be along the $([0\bar{1}\bar{1}])$ crystalline direction of the
diamond nanopillar (in a coordinate-system where $x-$, $y-$ and $z-$ correspond to
the horizontal-, vertical and out-of plane directions in Fig. 3.7.1b), by monitoring
the NV-ESR response to an externally applied magnetic field (using 3-axis
Helmholtz-coils). We then allowed for slight variations of the NV orientation
due to alignment errors between the diamond crystallographic axes and the scan
directions to find the NV orientation that reproduced our experimental data best.
With this procedure, we found an NV orientation $(\sqrt{2}\sin(\varphi), \sqrt{2}\cos(\varphi), 1)/\sqrt{5}$,
with $\varphi = \pi 162/180$.

Finally, we used this magnetic-field distribution to calculate the response of
the NV center to a magnetometry scan as described in the main text. For this, we
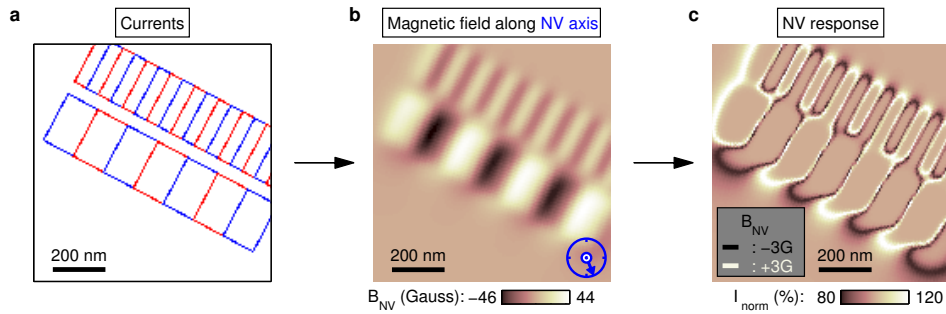
Figure 3.7.1: Simulation of NV response to bits of a magnetic memory. (a) Current distribution used to simulate the magnetic bits imaged in this work. Red (blue) loops indicate currents of 1 mA in the (counter-)clockwise direction. (b) Magnetic field generated by the current-distribution in (a), projected on the NV axis at a height of 50 nm above the current loops. The NV axis was tilted by 37° out of the scan-plane ($[1\bar{1}1]$ crystalline direction) with an in-plane component as illustrated by the blue arrow. (c) NV magnetometry response obtained from the magnetic field distribution in (b), assuming a Lorentzian NV-ESR response and microwave detunings as in the original experiment (see text). Note that this experimental situation only resolves magnetic field lines corresponding to the microwave detuning (here: $B_{NV} = \pm 3$ G).

assumed a Lorentzian ESR response with a full-width at half maximum of 9.7 MHz, a visibility of 20 % and two external microwave sources with detunings ± 10 MHz from the bare ESR frequency, all in accordance with our original experimental parameters.

3.7.5   NV MAGNETOMETRY IN CLOSE PROXIMITY TO A STRONGLY MAGNETIZED SAMPLE

The presence of a strong magnetic field $B_\perp$, transverse to the NV axis leads to a reduction of contrast in optically detected ESR and moreover reduces the overall fluorescence intensity of the NV center [30]. These effects result from a mixing of the NV spin-levels in the optical ground and excited states of the NV center in the presence of $B_\perp$. Such mixing on one hand allows for spin non-conserving
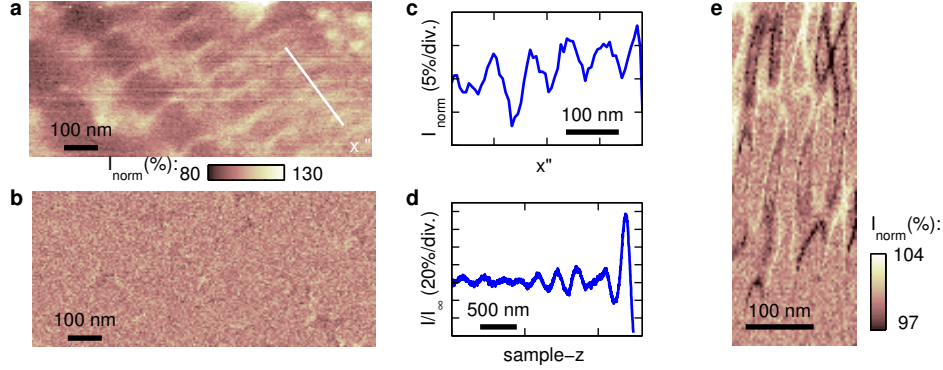
Figure 3.7.2: Quenching of NV fluorescence and ESR contrast in hard-disc imaging. (a) Total NV fluorescence I_{norm} as a function of sample position for an NV in close proximity to the hard-disc sample. I was normalized to the average fluorescence intensity of $I_o \approx 15000$ cps in the scan. Dark regions in the scan correspond to individual magnetic domains and are caused by strong magnetic fields transverse to the NV axis which occur in close proximity to the domains. (b) NV magnetic image recorded simultaneously with (a). Data acquisition and integration time per pixel was analogous to the magnetic imaging described in the main text. However here, due to strong transverse magnetic fields, NV ESR contrast almost completely disappeared and prevented NV magnetic imaging using optically detected ESR. The color-bar applies to (a) and (b). (c) Line-cut along the white line in (a), averaged over 7 adjacent pixels. I_{norm} shows a periodicity of ≈ 64 nm, indicating a bit-width of 32 nm. (d) Fluorescence approach curve on the magnetic memory medium. NV fluorescence I was normalized to the fluorescence rate $I_\infty = 27'000$ cps when the NV center was far from the sample. In contact with the magnetic sample (last data-point to the right), NV fluorescence was reduced by almost a factor of two compared to the NV counts far from the sample. (e) Magnetic imaging with the same NV sensor: Even in close contact to the sample, NV magnetic imaging using ESR is still possible, albeit with a strongly reduced ESR contrast and signal to noise ratio compared to the data shown in the main text. Data in (e) was acquired over 180 minutes, for the smallest resolvable magnetic domains (top third of image) we measure a mean width of 16.5 nm. The laser power was set to 100 μW in a-d and 60 μW in e.

optical transitions and on the other hand suppresses the spin-dependence in shelving from the NV excited state (triplet) to the metastable NV singlet state. Both, spin-conservation under optical excitation and spin-dependent shelving are responsible for the non-zero contrast in optically detected ESR of NV centers [33] and consequently, their suppression with transverse magnetic fields explains the disappearance of NV magnetometry features when closely approaching a strongly magnetized sample.

Fig. 3.7.2a shows the raw NV fluorescence counts observed when scanning an NV in a diamond nanopillar in close proximity (estimated $10 - 20$ nm distance between NV and sample surface) to the sample. Dark features appear when the NV is scanned over magnetic bits that enhance $B_\perp$, while the inverse happens when $B_\perp$ is reduced (or the longitudinal field B_{NV} enhanced) by local fields. This mode of bit-imaging allows for spatial resolutions $\approx 20 - 30$ nm (Fig. 3.7.2c). At the same time, a magnetic image recorded with the technique described in the main text shows no appreciable imaging contrast (Fig. 3.7.2b). Only exceedingly long integration times on the order of hours allowed us to reveal weak magnetic features with dimensions on the order of 20 nm (Fig. 3.7.2d).

The rates of the two effects which lead to a disappearance of ESR contrast, i.e. spin-flip optical transitions and shelving of $m_s = 0$ electronic states into the metastable singlet, scale approximately as $\left(\frac{B_\perp}{D_{GS}-D_{ES}}\right)^2$ and $\left(\frac{B_\perp}{D_{ES}}\right)^2$, respectively, with $D_{GS(ES)}$ the ground- (excited-) state zero-field spin-splitting of 2.87 GHz and 1.425 GHz [32], respectively. Given that $D_{GS} \approx 2D_{ES}$, the scaling of the two mechanisms with $B_\perp$ will be very similar. The characteristic scale of D_{ES} $(D_{GS}/2)$ for the disappearance of ESR contrast thus allows us to estimate $B_\perp$ close to the sample to be $B_\perp \approx D_{ES}/\gamma_{NV} \approx 514$ Gauss. We note however that this simple argument likely gives and over-estimation of $B_\perp$ as smaller values can already significantly effect ESR contrast and NV fluorescence intensity due to the complex dynamics of NV spin pumping. Indeed, strong reductions of NV fluorescence rates for $B_\perp$ less than 100 G have been observed in the past [30]. Transverse magnetic fields on this order were consistent with the largest *on-axis* magnetic fields observed on our experiments as well as with the calculations of
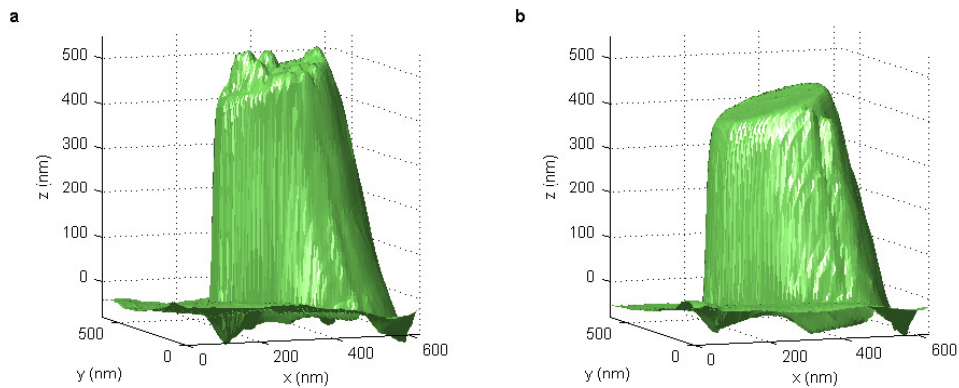
Figure 3.7.3: Contamination of diamond tips. (a) AFM image of the end of a scanning diamond nanopillar after contamination during scanning. The image was acquired by scanning the diamond nanopillar over a sharp diamond tip as shown in Fig. 3.7.4. (b) AFM Image of the same nanopillar as in (a) after cleaning of the pillar's end-face by repeated "scratching" over the sharp diamond tip.

magnetic field profiles presented in Sect. 3.7.4 (for the parameters used in Fig. 3.7.1, we obtain maximal values of $B_\perp \approx 200$ Gauss for an NV-to-sample distance of 20 nm).

3.7.6 LIMITATIONS TO NV-SAMPLE DISTANCE

As mentioned in the main text, NV-sample distance is an essential parameter for the performance of our microscope as it determines the overall resolving power with which weak magnetic targets can be imaged. We identified three critical parameters that can affect NV-sample distance:

- Implantation-depth of NV centers in the diamond nanopillars:
  The depth of the NV centers created using ion implantation can be controlled by the energy of the ions used for NV creation. However, the stopping of ions in matter is a random process [104] and the depth of the created NV centers therefore not perfectly well-defined. This straggle in ion implantation poses an intrinsic uncertainty to the distance between

the scanning NV and the end of the diamond nanopillar. For implantation energies of 6 keV (with nominal implantation-depths of 10 nm) as used in this work, NV straggle has recently been shown to be as large as $10 - 20$ nm [37, 97]. We note that since straggle in NV implantation is hard to circumvent it is essential for the future to develop techniques to precisely pre-determine the depth of a given sensing NV in a diamond nanopillar. This could be performed using recently developed nanoscale imaging methods for NV centers [37], or by scanning the NV sensor over a well-defined magnetic field source.

- Contamination of scanning diamond nanopillars:
  During scanning-operation, the scanning diamond nanopillar can gather contamination from the sample or environment. An example for such a contaminated diamond-tip is shown in the AFM image shown in Fig. 3.7.3a (which was acquired with the scanning protocol employed in Fig. 3.5.1, using the a sharp diamond tip as shown in Fig. 3.7.4). Such contamination can artificially increase the distance of the scanning NV center to the sample by several 10's of nm (see Fig. 3.7.3a). To undo contamination of the diamond-tip after excessive scanning over dirty samples, we developed a "tip-cleaning technique" that allowed us to revert a contaminated tip to its initial, clean state (as illustrated by the transition from Fig. 3.7.3a to b). Tip cleaning is performed by repeated scanning of the diamond nanopillar over a sharp diamond tip (Fig. 3.7.3a) in the absence of AFM feedback. Such feedback-free scanning can partly remove contamination from the diamond pillar, which after repeated operation leads to a clean device as the one shown in Fig. 3.7.3b.
  We note that with proper sample-cleaning, control over environmental conditions and occasional "tip-cleaning" runs, adverse effects of tip-contamination can be essentially eliminated. This, together with the excellent photo-stability of NV centers, then allows for long-term operation of the scanning NV sensor.
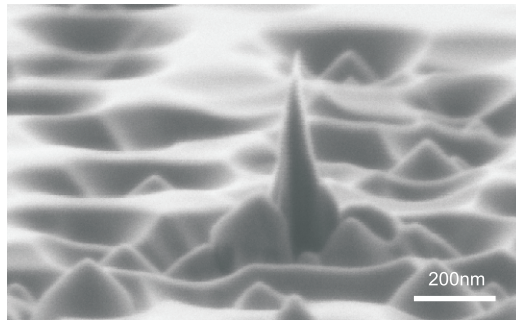
Figure 3.7.4: Sharp diamond tip for FQI. Image of a sharp diamond tip similar to the one used for the experiments presented in Fig. 3.5.1a of the main text. Typical tip-radii are on the order of 10nm.

- AFM control:

  Proper AFM control is necessary to assure close proximity of the NV center to the sample surface. It has been shown in the past that bad mounting or improper AFM feedback control can lead to AFM tip-sample distances in excess of 20 nm [52]. Careful mounting of AFM tips and proper setup and tuning of AFM feedback (here provided by an Attocube ASC500 controller) was therefore essential to observe, for instance, the fluorescence quenching features discussed in Fig. 3.5.1 of the main text.

3.7.7 FABRICATION OF SHARP DIAMOND TIPS

For the experiment presented in Fig. 3.5.1a of the main text, we fabricated sharp diamond tips which were metal coated for in order to localize the NV in the scanning nanopillar through fluorescence quenching. Diamond tip fabrication was based on the nanofabrication techniques [45] that we already employed for the production of the scanning diamond nanopillars presented in Fig. 3.2.1. A type Ib diamond (Element six) was patterned with circular etch-masks (flowable oxide, FOx XR, Dow Corning) of 100 nm diameter. Here, in order to obtain sharp diamond tips instead of cylindrical diamond nanopillars, we modified the RIE etching recipe we had previously used: While we kept the (oxygen) etching

chemistry identical to pillar fabrication, we significantly increased the etching time, such as to completely erode the etch mask on the diamond substrate. As a result, the etched diamond structures acquired the form of sharp tips as shown in the representative SEM image in Fig. 3.7.4. Typical tip-radii were in the range of 10 nm and tip lengths were on the order of 200 nm.

For the experiments described in the main text, we then coated the sharp diamond tips with a thin metallic layer using thermal metal evaporation. To avoid oxidation of the metal, we chose gold as the quenching metal and used a chrome adhesion layer between the gold and the diamond. For the tips employed in this work, we deposited 5 nm of gold and 5 nm of chrome.

3.7.8   Explanation of topographic features in Fig. 3.5.1

The features observed in Fig. 3.5.1a of the main text were governed by direct fluorescence quenching through metallic objects (as highlighted by the red square in the figure) and by a confluence of the distance-dependence of the NV fluorescence with topographic features on the sample (bright, ring-shaped feature in the figure). When approaching the NV to our metallic sample-surface, the total NV fluorescence collected in the far-field through the pillar changed as shown in the measurement in Fig. 3.7.5b. This well-known [28] variation of NV fluorescence is a result of the variable electromagnetic density of states in the vicinity of metallic or dielectric interfaces, which influences the NV radiative lifetime as well as the total effective laser excitation intensity impinging on the NV center. During our scanning experiments, the topography causes the mean distance between the scanning NV center in the nanopillar and the metallic substrate to vary, which in turn causes variations in the collected NV fluorescence rate. Assuming to first order that the metallic tip does not itself affect NV fluorescence (so long as it is not placed in direct contact to the NV center as in the "red-square region"), one can understand most features observed in Fig. 3.5.1a as a pure effect of topography. Based on this principle, in Fig. 3.7.5 we reconstruct the data in Fig. 3.5.1a from a measurement of sample topography (a)
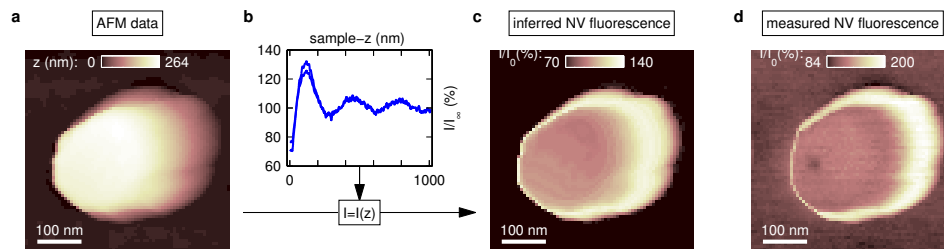
Figure 3.7.5: Explanation of topographic features in fluorescence quenching. (a) AFM topography recorded during the experiment presented in Fig. 3.5.1 (same data as shown in Fig. 3.5.1a). (b) "Approach-curve" of the far-field NV florescence rate as the nanopillar with the NV center was approached to the sample. "z=0" was defined as the point of AFM contact (leftmost data-point) (c) Total fluorescence image reconstructed form the datasets in (a) and (b): Looking up the NV fluorescence intensity in (b) for every tip-sample displacement measured in (a) yields the reconstructed topographic features shown in the panel. We note that here, fluorescence quenching is solely induced by the sample surface, while the tip merely acts as a "spacer" between NV center and sample. Fluorescence-quenching that is directly induced by the tip (additional dark spot in d) is not reproduced here. (d) Original data (same data as Fig. 3.5.1a). The features common to (c) and (d) are attributed to effects of sample topography. The additional, dark feature in the center of (d) (red square in Fig. 3.5.1a) has no correspondence in topography and stems from direct fluorescence quenching of the NV center on the sharp metallic tip.

and an independently acquired fluorescence "approach-curve" (b), characteristic for fluorescence quenching of an emitter approaching a metallic surface [12]. The reconstructed image (Fig. 3.7.5c) was obtained by taking the value of the AFM z-displacement for each point in the scan in Fig. 3.7.5a and looking up the corresponding fluorescence-rate obtained in the approach-curve. The resulting image shows striking similarity with the actually measured data (Fig. 3.7.5e; same data as Fig. 3.5.1a) and supports the validity of our explanation.

4

Nanoscale magnetic imaging of a single electron spin under ambient conditions

4.1 INTRODUCTION

The detection of ensembles of spins under ambient conditions has revolutionized the biological, chemical, and physical sciences through magnetic resonance imaging [66] and nuclear magnetic resonance [9, 84]. Pushing sensing capabilities to the individual-spin level would enable unprecedented applications such as single molecule structural imaging; however, the weak magnetic fields from single spins are undetectable by conventional far-field resonance techniques [35]. In recent years, there has been a considerable effort to develop nanoscale scanning magnetometers [15, 53, 67, 105], which are able to measure fewer spins by bringing the sensor in close proximity to its target. The most

sensitive of these magnetometers generally require low temperatures for operation, but measuring under ambient conditions (standard temperature and pressure) is critical for many imaging applications, particularly in biological systems. Here we demonstrate detection and nanoscale imaging of the magnetic field from a single electron spin under ambient conditions using a scanning nitrogen-vacancy (NV) magnetometer. Real-space, quantitative magnetic-field images are obtained by deterministically scanning our NV magnetometer 50 nanometers above a target electron spin, while measuring the local magnetic field using dynamically decoupled magnetometry protocols. This single-spin detection capability could enable single-spin magnetic resonance imaging of electron spins on the nano- and atomic scales and opens the door for unique applications such as mechanical quantum state transfer.

To date, the magnetic fields from single electron spins have only been imaged under extreme conditions (ultralow temperatures and high vacuum), with data integration times on the order of days [88]. Magnetometers based on negatively charged nitrogen-vacancy (NV) centers in diamond have been proposed as sensors capable of measuring individual spins [5, 22, 70, 95] because they can be initialized and read-out optically [41] and have long coherence times [6], even under ambient conditions. Moreover, since NV centers are atomic in size, they offer significant advantages in magnetic resolution and sensing capabilities if they can be brought in close proximity of targets to be measured. Recent advances in diamond nanofabrication have allowed for the creation of robust scanning probes that host individual NV centers within roughly 25 nm of their tips [62]. Here, we employ such a scanning NV center to image the magnetic dipole field of a single target electron spin.

4.2   Scanning NV magnetometer

As described in Chapter 2, our scanning NV magnetometer (Fig. 4.2.1a) consists of a combined confocal and atomic force microscope (AFM), which hosts a sensing NV center embedded in a diamond nanopillar scanning probe tip [62].

The sensor NV's spin-state is initialized optically and read out through spin-dependent fluorescence, while its position relative to the sample is controlled through atomic-force feedback between the tip and sample. Microwaves (MWs) are used to coherently manipulate the sensor NV spin. Magnetic sensing is achieved by measuring the NV spin's optically detected electron spin resonance (ESR), either by continuously applying near-resonant MW radiation (Fig. 4.2.1b) or through pulsed spin-manipulation schemes [70, 95], (Fig. 4.2.1c), where the sensor NV spin precesses under the influence of its local magnetic field (projected along the NV center's crystallographic orientation). We measure the contribution of the magnetic field from a target electron spin to this precession. The entire system, including both the scanning NV magnetometer and the target sample, operates under ambient conditions.

4.3   Isolated NV spin as a target single electron spin

To verify the single-spin detection and imaging, we choose our target to be the spin associated with an additional negatively charged NV center in a separate diamond crystal (so that the sensor and target NV centers can be scanned relative to one another). The advantage of using an NV target is that both its location and spin state can be independently determined by its optical fluorescence. As discussed below, we can thus compare the target NV's magnetically measured location to its optically measured location and ensure that the magnetic image is from a single targeted spin. Additionally, we can guarantee that the target spin is initialized and properly modulated, as is useful for optimizing AC magnetic sensing.

To isolate single NV targets for imaging, NV centers are created in a shallow (< 25 nm) layer of a bulk diamond through established implantation and annealing techniques (see Supp. 4.7.2). The target diamond surface is structured to create nanoscale mesas, whose diameters (~ 200 nm) are chosen to contain,
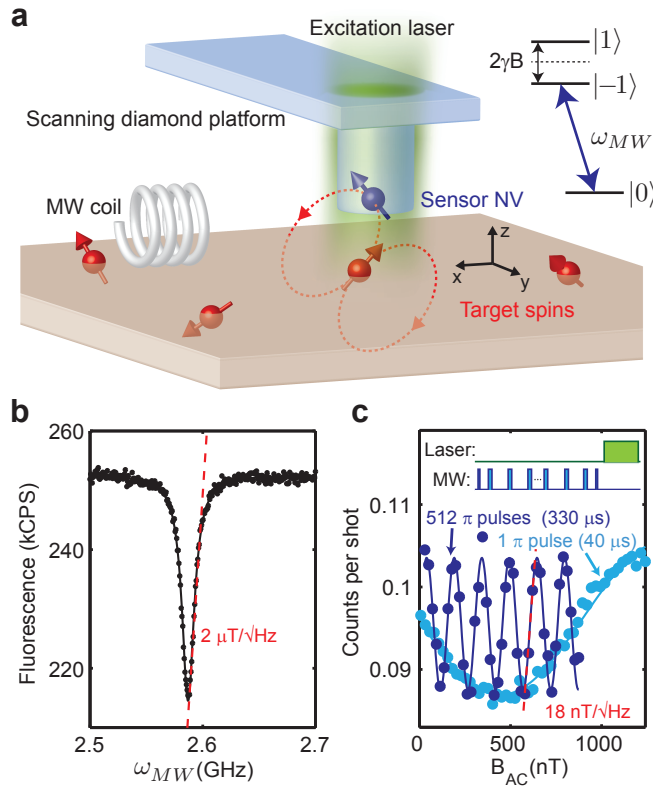
Figure 4.2.1: Scanning NV magnetometer. (a) Conceptual schematic of the scanning NV magnetometer. The sensor NV is hosted within a scanning diamond nanopillar [62], where its spin is initialized and read-out optically from above (532 nm excitation laser spot shown). Coherent NV spin manipulations are performed via a nearby microwave (MW) coil, in this work operating near resonance with the $|0\rangle$ or $|-1\rangle$ transition, in the presence of a static applied magnetic field (not shown). The sensor NV is scanned over target spins of interest to construct magnetic field images. (b) By continuously applying the excitation and sweeping the MWs across the $|0\rangle$ to $|-1\rangle$ transition, optically detected magnetic resonance provides a measure of the static magnetic field at the NV center, with a DC sensitivity of $\sim 2\mu T/\sqrt{Hz}$. (c) By dynamically decoupling the sensor NV spin from its environment, the sensor's magnetic field sensitivity is dramatically improved for AC magnetic fields. Plotted are a spin-echo (1-pulse) magnetometry sequence with a $40 - \mu$s total evolution time, and a 512-pulse XY8 [42] magnetometry sequence (see Supp. 4.7.1) with $330 - \mu$s total evolution time, which achieve magnetic field sensitivities of 56 nT/$\sqrt{Hz}$ and 18 nT/$\sqrt{Hz}$, respectively.

on average, a single NV spin. Mesas with single NV centers (as determined through photon auto-correlation experiments, Supp. 4.7.4) are chosen for our measurements. In order to individually control the target and sensor NV spins, we choose a target NV center with a different crystallographic orientation (which determines the spin quantization axis) from the sensor NV, so that their spin transitions can be spectrally separated in ESR measurements by applying a uniform static magnetic field.

Spatial features in the collected fluorescence from scanning the NV magnetometer over target diamond mesas allow us to independently determine the relative positions of the sensor and target NV spins (Fig. 4.3.1). Firstly, the scanning diamond nanopillar acts as a waveguide [4] which, when centered precisely above the target NV, provides efficient collection of fluorescence from the target NV (in addition to the sensor NV). Also, the sensor NV's fluorescence is efficiently coupled into the target bulk diamond when it is centered on a mesa, due to the diamond's high refractive index. The intersection of these two near-field fluorescence features indicates where the sensor NV spin is closest to the target NV spin. This spatial location is later used to confirm the location of the magnetically imaged target NV spin.

4.4   Single spin detection scheme

Near the expected location of the target, the local magnetic field is measured with a magnetometry pulse sequence performed on the sensor NV using a combination of dynamic decoupling [19] and double electron-electron resonance [59]. The sensor NV spin is prepared in a superposition of spin states, where it accumulates phase proportional to the local magnetic field, including contributions from the target NV spin. To optimize magnetic field sensitivity, the sensor NV is dynamically decoupled from fluctuating magnetic fields in its environment (Fig. 4.4.1, upper panel) through the repeated application of MW π-pulses. Normally, this pulse sequence would also remove any magnetic signal
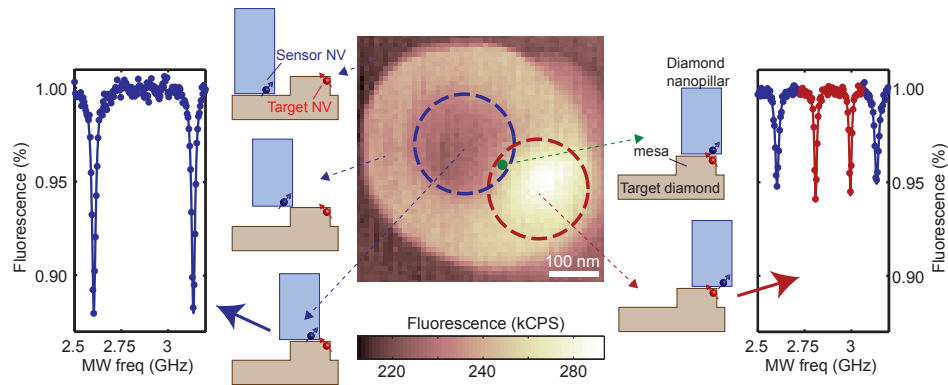
Figure 4.3.1: Independent determination of a target spin's location.
The sensor NV's diamond nanopillar is scanned over a target nanostructure
("mesa") containing a single target NV center. The combined NV fluores-
cence is recorded as a function of position (center panel). The fluorescence
has a strong spatial dependence because (i) sensor NV fluorescence can par-
tially couple into the target bulk diamond when the sensor NV is close to the
sample surface, and (ii) target NV fluorescence can couple into the nanopillar
waveguide when the nanopillar is located above of the target NV. When the
nanopillar is located away from the target NV, only fluorescence from the sen-
sor NV is collected, as indicated by ESR measurements showing two spectral
peaks corresponding to the sensor NV spin $m_S = 0 \leftrightarrow \pm 1$ transitions (left
panel). For ESR measurements taken with the nanopillar located above the
target NV (right panel) there are four observable spectral peaks that corre-
spond to both the sensor and target NV spin transitions (blue and red, respec-
tively), with reduced ESR contrast due to collecting fluorescence from both
NV spins. The center of the target-coupling circle (red dashed circle around
bright fluorescence spot) indicates the lateral location of the target NV spin
relative to the center of the nanopillar. Similarly, the center of the sensor-
quenching circle (blue dashed circle around dark fluorescence spot) indicates
the lateral location of the sensor NV spin. With both NV spins' lateral loca-
tions known, the position of sensor-target closest approach can be ascertained
(green dot).

from a static target spin, but we also simultaneously invert the target NV spin in phase with the π-pulses applied to the sensor NV spin (Fig. 4.4.1, lower panel) to maintain the sign of phase accumulation by the sensor spin due to the target NV spin. The total acquired phase is converted to a population difference, which is measured via NV spin-dependent fluorescence.

With the sensor NV in close proximity to the target diamond surface, the field sensitivity of the sensor NV is reduced, because sensor NV fluorescence is partially emitted into the target bulk diamond (due to its high refractive index), and the target NV adds background fluorescence to magnetic measurements. Because of these effects, our sensor NV's magnetic field sensitivity at closest approach to the target NV is somewhat reduced to approximately $96 \text{ nT}/\sqrt{\text{Hz}}$ (with a 32-π-pulse XY8 [42] decoupling scheme and a 40-μs total phase accumulation time; Supp. 4.7.8). Since the target NV is embedded in bulk diamond, the sensor-to-target vertical separation is roughly twice the distance between the sensor NV and the diamond surface. Thus, for our magnetic field imaging of a single target NV spin, we expect a $\sim$ 50-nm sensor-target vertical separation, which results in a magnetic field of about 10 nT at the sensor NV location.

4.5   Nanoscale imaging of the magnetic field from a single electron spin

A magnetic field image centered at the expected target spin location is acquired by averaging the sensor's NV fluorescence in multiple scans of the NV magnetometer across a $\sim$ 200 $\times$ 200-nm field-of-view (taken using a lateral drift correction scheme detailed in Supp. 4.7.6). A normalization scheme is applied to the magnetometry, where we alternately initialize the target NV spin in the $|0\rangle$ state and the $|-1\rangle$ state and measure the equal and opposite phase shifts induced during the sensor NV's magnetometry sequence (Supp. 4.7.5). We subtract the measured NV fluorescence rates for these two initial target NV spin polarizations,
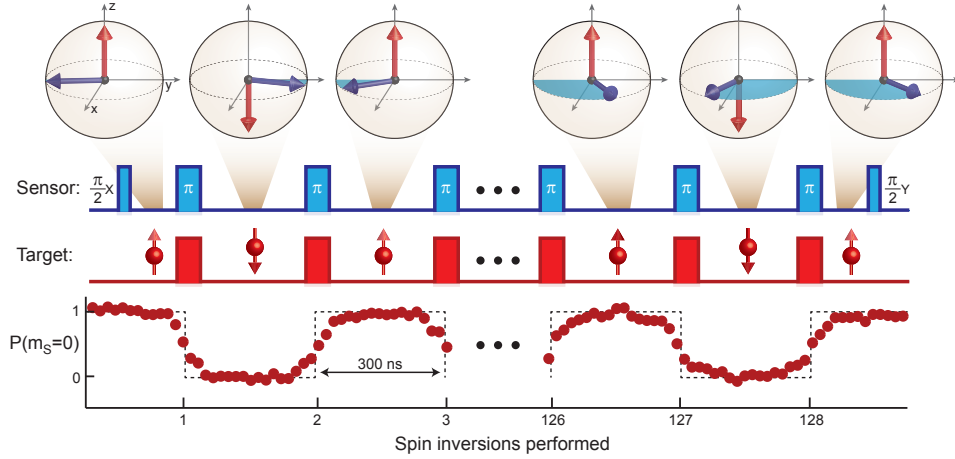
Figure 4.4.1: Single spin detection scheme and target spin modulation verification. To detect the magnetic field from the target NV spin, the sensor NV spin (top panel, blue arrow) is placed in a superposition of spin states with a MW $\frac{\pi}{2}$ pulse (around the X axis). It then evolves under the influence of the magnetic field from the target spin (red arrow), accumulating phase (shaded blue region, whose extent is visually exaggerated for visibility). To optimize the sensor spin's magnetic sensitivity, it is dynamically decoupled from its environment (see Supp. 4.7.1) [19] by the repeated application of MW π-pulses using an XY8 sequence [42]. In order to magnetically measure the target NV spin, it is inverted, synchronously with the π-pulses applied to the sensor NV, so that phase shifts induced on the sensor by the target spin constructively accumulate. (The target NV spin is modulated between the $m_S = 0$ and $m_S = -1$ states to isolate an effective spin-$\frac{1}{2}$ system from the target NV's spin triplet.) To invert the target NV spin with high fidelity, we employ adiabatic fast passages (see Supp. 4.7.3). Plotted is the measured fluorescence for pulses 1, 2, 127, and 128, indicating that the target NV spin can be modulated many times without substantial polarization decay. The sensor NV's accumulated phase is converted to a population difference using a final $\frac{\pi}{2}$ pulse, whose axis (Y) is chosen to maximize sensitivity to small magnetic fields.

which isolates the magnetic field signal from the target spin (Supp. 4.7.7).

Near the center of the magnetometry scan, we observe a drop in the normalized fluorescence from the magnetometry sequence that is well beyond the uncertainty set by the measurement's noise level and is consistent with the effect of a single target NV spin's magnetic field on the sensor NV. The complete magnetic field image clearly indicates the presence and location of the target NV spin (Fig. 4.5.1a). This single electron spin detection is confirmed by repeating the measurement with a spatial linecut of magnetometry measurements (Fig. 4.5.1b), with a resulting magnetic response that fits well to a vertical separation of 51.1 ± 2.0 nm between the sensor and target NV centers. (Errors are determined from the χ^2 of the fit as a function of distance, where the sensor-to-target displacement is the only free-parameter and the orientations of both NV spins are independently measured using ESR.) The measured fluorescence difference is converted to a magnetic field at the sensor NV (peak value of 8.6 nT, Fig. 4.5.1b) by using the sensor NV spin's independently calibrated magnetic field response and fluorescence rate. Both scanning magnetometry measurements are in good agreement with simulations of the sensor NV's response to the magnetic field from a single electron spin at a vertical distance of 51 nm (Fig. 4.5.1c). Thus the above measurements are consistent and confirm the detection and nanoscale imaging of the single target spin.

In the demonstrated magnetic field imaging, single-spin measurements with a signal-to-noise ratio (SNR) of one can be acquired in 2.3 minutes. The data for both single-spin measurements presented in Fig. 4.5.1 have been integrated for a total time of 42 minutes per point, yielding an SNR of 4.3. This integration time is consistent with the measured target NV spin magnetic field (8.6 nT) and sensor NV magnetic field sensitivity calculated by assuming the noise is dominated by photon shot noise ($96 \, \text{nT}/\sqrt{\text{Hz}}$).

Figure 4.5.1: Single-spin magnetic imaging. (a) Magnetic field image of a target NV spin near the surface of a diamond mesa, acquired with the scanning NV magnetometer. While repeatedly running an AC magnetometry pulse sequence (here with a 32-pulse XY8 sequence, with 40 μs of total evolution time), the sensor NV is laterally scanned over the target, and the fluorescence rates for the target spin starting in the $|0\rangle$ state as well as the $|-1\rangle$ state are independently recorded. Plotted is the difference between these measurements, which depends only on the sensor NV's magnetic interaction with the target spin and not on background fluorescence variations (see Supp. 4.7.7). The pronounced drop in fluorescence near the center of the image indicates a detected single electron spin. (b). An independent magnetometry linecut taken along the green arrow confirms the single spin imaging, which has an intensity and width consistent with the recorded image. The measured fluorescence difference is converted to the measured magnetic field using the sensor NV's calibrated field sensitivity and fluorescent rate (see Supp. 4.7.8). (c) Simulated fluorescence due to a target spin. With only the sensor-target displacement as a free parameter, the spin signal is simulated, which agrees well with both the spin image and the linecut for a vertical distance of 51 nm (the fit in (b) and the image in (c) have the same parameters). (d) If the sensor-target vertical distance can be moderately reduced, the quality of single-spin imaging will be dramatically improved. Plotted are simulated lateral magnetic field contours from a single target electron spin for different sensor-target vertical separations where each contour indicates an increase of signal-to-noise by one for a 100 second integration time. At 50 nm (the current condition), there is only one contour, indicating single-spin imaging with a signal-to-noise of one; however at 10 nm, a signal-to-noise of roughly 100 is possible, such that many contours and the dipole lobes of the target spin are clearly observable.

Figure 4.5.1 *(Continued)*

a Experiment

Fluorescence difference (CPS)

-4 -3 -2 -1 0 1

b

c Simulation

Fluorescence difference (CPS)

-4 -3 -2 -1 0 1

d
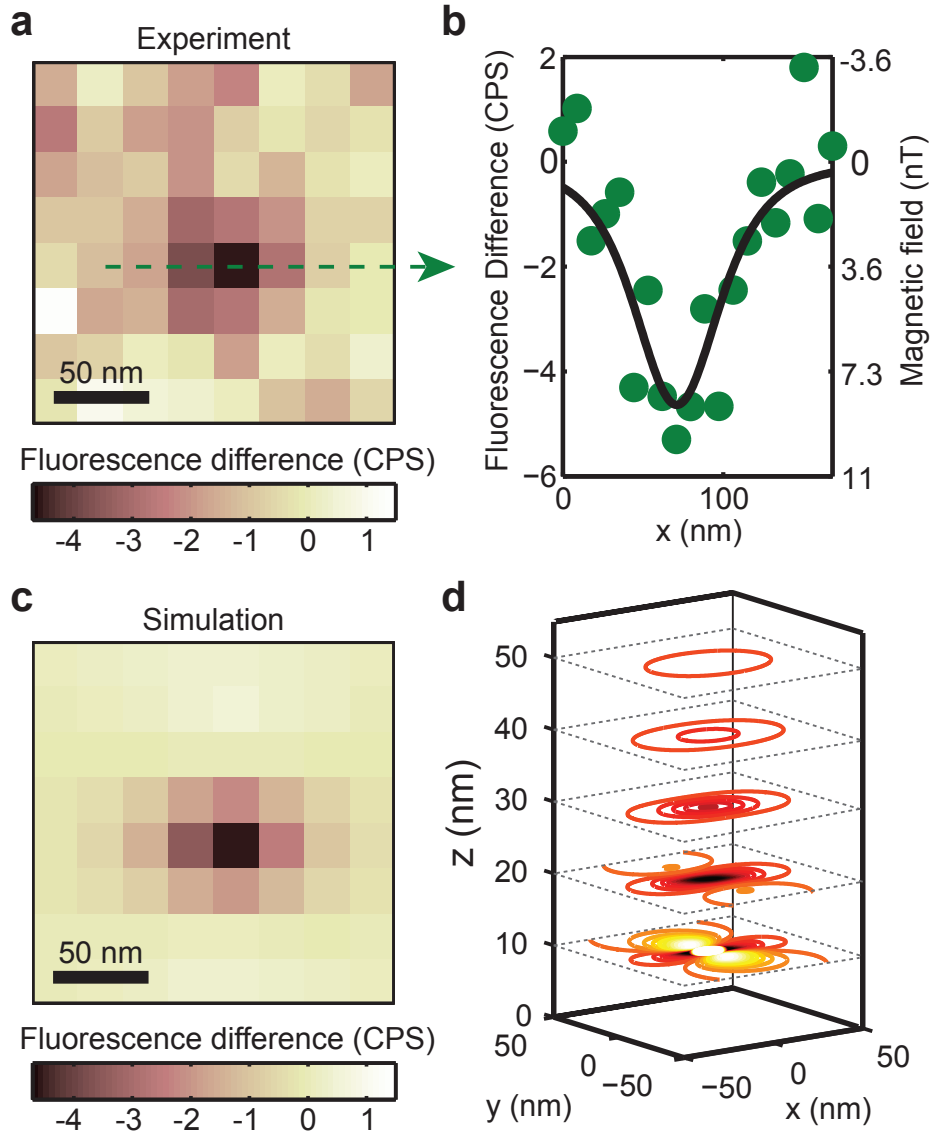
4.6 Discussion and outlook

By successfully measuring the magnetic field from a single target NV spin, our spin-sensing protocols have been confirmed, enabling otherwise undetectable "dark" electron spins to be detected with confidence. Note that imaging dark spins rather than an NV target could potentially be performed with higher sensitivity, because optical fluorescence from the sensor NV could be better collected and isolated. In addition, for dark spins on or near a sample surface rather than embedded beneath it, the sensor-to-target separation would be reduced by a factor of about two: thus the SNR for magnetic field imaging would increase by nearly an order of magnitude (Fig. 4.5.1d) because dipolar fields decay as $1/r^3$. Moreover, the required measurement time for a given SNR scales with the sixth power of sensor-to-target separation for a shot-noise-limited measurement: e.g. at a separation of 25 nm, a target surface spin would be detectable in two seconds (with our instrument's demonstrated sensitivity and a SNR of one).

For target spins of interest that cannot be initialized, the variance of the magnetic field at the sensor NV could instead be measured, which is detectable with nearly the same sensitivity as the field itself if an appreciable amount of phase can be acquired [95]. For instance, at a 25 nm sensor-to-target distance, with a phase evolution time of $100\mu s$, an uninitialized, driven spin could be detected within two seconds of integration time (SNR of one, for the same sensor NV spin-dependent fluorescence rate and contrast as in the demonstrated spin imaging; Supp. 4.7.9). For the phase-evolution time used in the demonstrated single-spin imaging ($40\mu s$), the integration time would be 20 s.

If the coherent sensor-target coupling is strong enough for more than 2π of sensor NV phase to be accumulated during magnetic field measurements, then phase-estimation techniques can be employed, thus allowing the measurement noise to decrease linearly in time [78, 99], and potentially offering a great boost in speed to magnetic imaging. Moreover, if a target spin can be initialized and has a coherence time as long as the sensor NV, then the target and sensor spins could

be entangled. Combined with long-lived storage techniques for quantum states [69], the ability to entangle a scanning sensor and target spins could allow for mechanical transfer of quantum information between solid-state spins.

4.7   Supplementary section

4.7.1   Dynamic decoupling of the sensor NV spin

The sensor NV spin coherence time is prolonged by dynamically decoupling it from its noisy environment [10, 19, 20]. This is achieved by the repeated application of microwave (MW) π-pulses, which causes the effects of slowly fluctuating magnetic fields to re-phase and cancel out. To apply a large number of pulses without scrambling the sensor NV spin state, the control pulses are carefully calibrated to within 2% using a boot-strap tomography scheme [24]. For the dynamic decoupling scheme and magnetometry, we employ an XY8 sequence [42], which uses π-pulses around two orthogonal axes on the equator of the sensor NV's Bloch sphere to minimize the accumulation of pulse errors. This sequence $(\pi_x - \pi_y - \pi_x - \pi_y - \pi_y - \pi_x - \pi_y - \pi_x)$ is repeated as many times as possible to maximize the sensor NV's magnetometry sensitivity, which – as a function of the number of pulses – is a compromise between the extended NV coherence from the decoupling and the reduced contrast from accumulated pulse errors.

MW fields are supplied from a Rhode and Schwarz SMB100A signal generator. MW phase control is achieved using an IQ mixer (Marki-1545) with pulsed analog inputs on the I and Q ports supplied by an arbitrary waveform generator (Tektronix AWG5000). NV spin Rabi frequencies in this work are 15-20 MHz, with typical π-pulse durations of 30 ns.

4.7.2   NV center targets

NV centers were created through implantation of ^{15}N ions [83] into ultrapure diamond (Element Six, electronic grade diamond, $<$ 5 ppb nitrogen). The

implantation was done at an energy of 6 keV with a dose of $2.5 \cdot 10^{11}$ cm^{-2} to give a nominal nitrogen depth of 10 nm [104]. To form NV centers, the sample was annealed in vacuum at 800 °C, where existing vacancies are mobile and can pair with the implanted nitrogen atoms. The resulting density of NV centers corresponds to one center every $\sim$ 200 nm, forming a layer within $\sim$ 25 nm from the surface. To isolate NV centers, we selectively etched [60] away most of the shallow diamond surface layer, leaving individual NV-containing nanostructures. This was done using electron-beam lithography to define an etch mask from a flowable oxide [45] (Dow Corning, XR-1541). A reactive-ion etch then removed any exposed diamond surfaces, resulting in shallow diamond nanostructures (200 nm across) containing, on average, single NV centers. The spacing between the structures are chosen to be 3 μm, sufficiently larger than the size of focused laser spot, which ensures optical measurements of only one structure at a time, We then, perform photon autocorrelation measurement (see Supp. 4.7.4) with each fluorescent diamond structure to find the ones with single NV centers.

4.7.3   ADIABATIC FAST PASSAGES FOR CONTROLLING THE TARGET NV SPIN

To control the target NV spin with high fidelity over numerous spin inversions, we employ adiabatic fast passages. The spin-state is prepared optically in the mS = |0> state, and microwaves (MW) with bare Rabi frequency ω_R are applied and detuned by $\delta(t = 0)$ from the target NV transition. The detuning is ramped through zero to $-\delta(t = 0)$ over a pulse time, T_p. At any point in time, the target NV spin in the rotating frame prececess around an effective magnetic field Ω_R, which is the sum of the MW field and the remaining static magnetic field in the rotating frame resulting from the non-zero MW detuning. If the angular velocity, $d\theta/dt$ of Ω_R is slow compared to ω_R, then the NV spin-state is effectively locked to the motion of this effective magnetic field as it moves from $|0\rangle$ to $|-1\rangle$. In general, it is advantageous to sweep the detuning non-linearly in time and spend most of TP when the NV spin is near the equal population state where it is most susceptible to dephasing [34]. To achieve this, we ramp the detuning to keep the

74

rate of change of the spin's angle with respect to the $|0\rangle$ state constant, so that:

$$\delta(t) = \omega_R \tan(\beta(\frac{t}{2T_p} - 1)) \tag{4.1}$$

where β is chosen to achieve the desired sweep range. For the adiabatic fast passages presented in Fig. 4.4.1 of the main text, $T_p = 300$ ns, $\delta(t = 0) = 100$ MHz, and $\omega_R = 17$ MHz.

The detuning ramping is implemented by using an arbitrary waveform generator to output a sinusoid at a frequency of the desired detuning, which is mixed with a continuous-wave MW source (all are the same make and model as the sensor-addressing MW equipment). By setting the phase of this sinusoid to be the integral of the detuning as a function of time, the mixed MW frequency can be continuously varied.
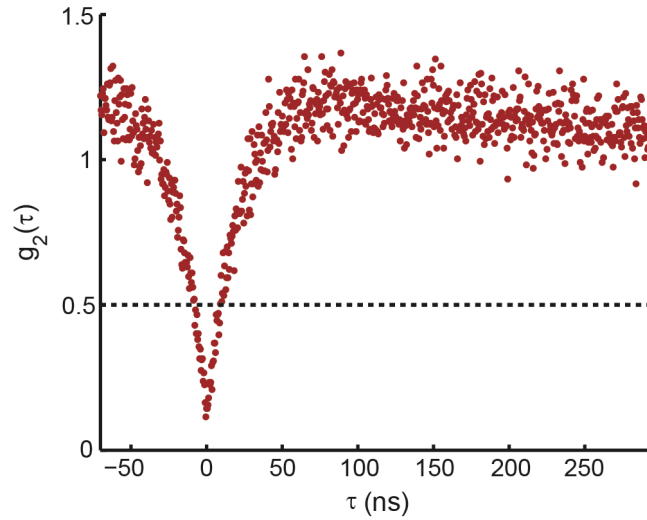
Figure 4.7.1: Photon-autocorrelation measurements for the target NV center.

4.7.4 PHOTON-AUTOCORRELATION MEASUREMENTS FOR THE TARGET NV CENTER

Photon-autocorrelation measurements for the target NV in the absence of the sensor NV (Fig. 4.7.1) give $g^2(\tau = 0) < 0.5$, ensuring that a single target NV spin lies in the diamond mesa on which magnetic field imaging is performed with the scanning NV magnetometer. No background subtraction was performed on the data and normalization was performed based on count-rates on the individual detectors as well as the time-binning in the photon-correlation hardware.

4.7.5 MAGNETOMETRY NORMALIZATION SCHEME

To isolate the sensor NV's spin-state-dependent fluorescence from spatially varying background fluorescence, we employ a normalization scheme that involves alternatively performing two slightly different magnetometry pulse sequences, and then subtracting the measured NV fluorescence rates (Fig. 4.7.2). These two sequences are similar to the double-electron-electron resonance
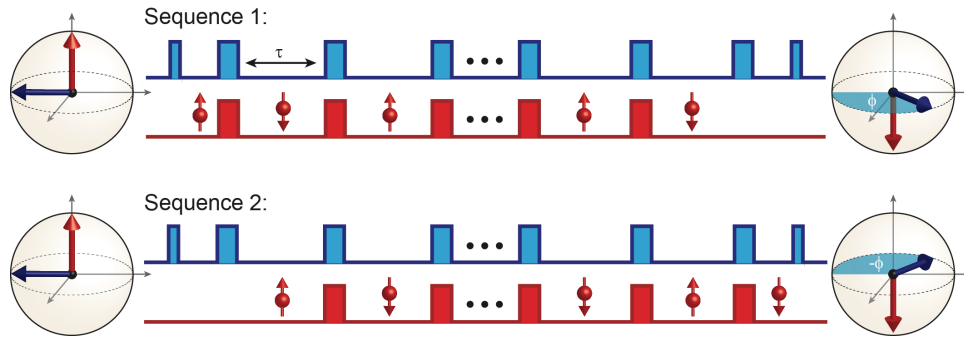
Figure 4.7.2: Magnetometry normalization scheme.

scheme presented in Fig. 4.7.3, except that one target NV spin-inversion (performed via an adiabatic fast passage) is removed from each sequence: in Sequence 1, the last spin inversion is removed, while in Sequence 2 it is the first spin inversion. By removing spin inversions in this manner, we ensure that the sensor NV (blue arrow) acquires an equal and opposite target-spin-induced phase shift (Φ, shaded blue region) during the two pulse sequences, because the target spin-state is inverted in the two sequences for the majority of the phase evolution time. Crucially, the target NV spin ends in the same state for the two pulse sequences (here, $|-1\rangle$). Thus subtracting the measured NV fluorescence rates for the two pulse sequences removes the contribution of background fluorescence from the NV target, which has a non-trivial spatial dependence (Fig. 4.3.1). Moreover, both pulse sequences have the same number of target spin inversions, which alleviates unavoidable spin-polarization losses associated with flipping the target spin and cross-talk between the applied MW sources. In this scheme, a small amount of integration time is unused for sensor NV phase accumulation (the portions next to the $\frac{\pi}{2}$ pulses at the beginning and end of each sequence cancel, equal to one delay period τ between π pulses). However in the limit of a large number of spin inversions, this loss of integration time is negligible.
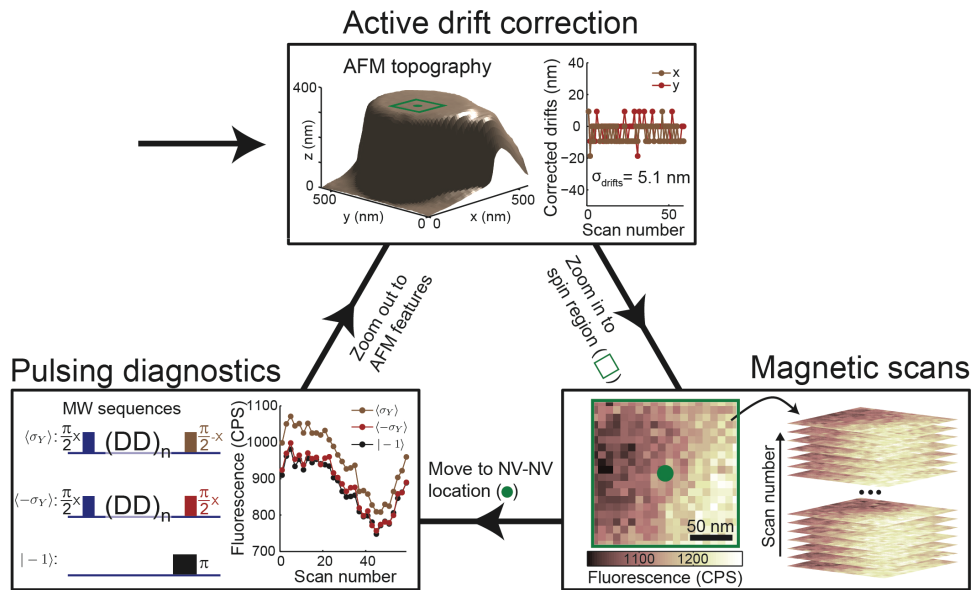
Figure 4.7.3: Magnetic field image acquisition protocol.

4.7.6 MAGNETIC FIELD IMAGE ACQUISITION PROTOCOL

Scanning an AFM for long periods of time with nanometer precision can be difficult to achieve under ambient conditions because of thermal-induced drifts. Temperature fluctuations on the order of a fraction of a degree can lead to tens of nanometers of relative motion between the sensor and target NV spins, which would considerably smear out our magnetic field imaging. These drifts generally occur on long time-scales, with a few nanometers of drift every hour. To minimize their effect, we employ an image acquisition protocol that periodically corrects for sensor-to-target drifts, as described in Figure 4.7.3.

The protocol has three major components: (1) Drift-correction using the sample topography to determine the target's location (top panel); (2) Taking a relatively quick magnetic scan over the target spin location (lower right panel); and (3) Checking to make sure that the MW pulsing has not degraded over time, and that the sensor NV's magnetic sensitivity has not been significantly compromised (lower left panel).

Drift correction is performed by scanning over the target-containing diamond

mesa, and the measured topography is the convolution of this mesa ($\sim$ 200 nm in diameter) with the diamond nanopillar scanning tip ($\sim$ 200 nm in diameter). From this topography, and the simultaneously measured fluorescence (as in Fig. 4.3.1), the target NV spin can be located (green dot) and an appropriate scan range can be defined (green square). The topography of successive scans (taken after both magnetometry and diagnostic measurements), can be compared to the first reference scan by cross-correlation, and thus drifts can be corrected between scans. In the single-spin measurements presented in Fig. 4.5.1, we observe a mean variation of 5 nm between successive scans (limited by the pixel size of the reference scan), indicating that magnetic field images can be overlapped with roughly 5-nm precision.

After zooming into the appropriate scan region, where the expected target spin NV lies in the center of the scan range, magnetic field images are acquired while simultaneously alternating between the two magnetic detection pulse sequences (Fig. 4.7.2) and monitoring their fluorescence rates (only one sequence is illustrated). Each scan is integrated for roughly 30 minutes to minimize the drifts between scans.

When a magnetic scan is finished, the sensor NV is placed at the approximate measurement position to measure the optimal sensitivity to the target NV and as a function of time. In general, the sensor NV can slowly drift in and out of the green laser confocal spot, causing variations in the overall detected NV fluorescence. Additionally, the power of the MW source can drift, which can decrease the performance of dynamic decoupling and magnetometry pulse sequences. Magnetic field sensitivity is experimentally determined by running the magnetometry sequence, with the phase of the last $\frac{\pi}{2}$ pulse set at $\pm\frac{\pi}{2}$ (red and brown data points, respectively) to measure the $\langle -\sigma_y \rangle$ and $\langle \sigma_y \rangle$ projections of the sensor NV. The difference between these measurements gives the contrast and counts of the sensor NV's magnetic response, and when combined with the phase accumulation time, determines the magnetic field sensitivity of the sensor NV. To differentiate overall NV fluorescence rate changes from pulsing performance changes, we also measure fluorescence counts for the $|-1\rangle$ state

79
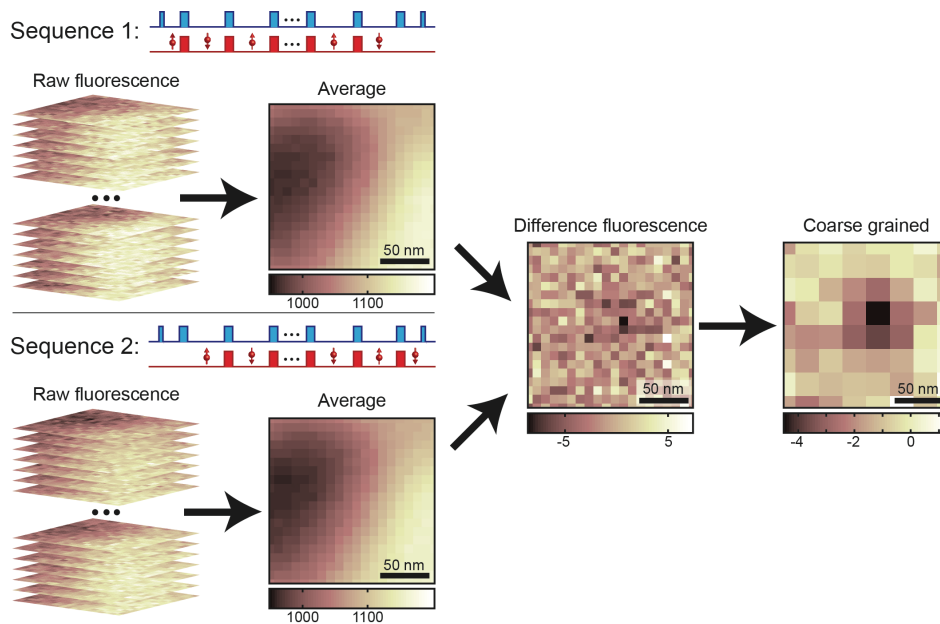
Figure 4.7.4: Magnetic field image data processing.

(black data points), which should overlap with the $-\sigma_y$ measurement in the case of no pulse errors or dephasing.

After these pulse diagnostics, we zoom out to measure the topography of the sample again, completing a measurement cycle. This procedure is repeated until a desired signal-to-noise in the magnetic field image has been achieved.

4.7.7 Magnetic field image data processing

The multiple images taken during a magnetic field scan for each magnetometry sequence (Fig. 4.7.4, left column) are averaged (without any further spatial correction), to yield the average fluorescence map (Fig. 4.7.4, center left column). In these averaged measurements, there are large variations in fluorescence due to near field coupling into and out of the diamond nanopillar for the target and sensor NV centers, as described in Fig. 4.3.1. These variations are quite large (~ 150 CPS) compared to the expected effect of a single target NV's magnetic field on the sensor NV signal (fluorescence change ~ 4 CPS under inversion of

the target NV spin). Subtracting the average fluorescence maps of the two magnetometry sequences yields a difference fluorescence signal free of the large background fluorescence (Fig. 4.7.4, center right). In general, the difference in fluorescence between the two magnetometry sequences has a small remaining offset, and so it has a mean of a few counts per second, even in the absence of the target NV. This is likely due to a small amount of cross-talk between the target-addressing MW and the sensor NV, which is slightly different between the two sequences. During our pulsing diagnostics in the measurement acquisition, we measure this fluorescence offset with the sensor NV very far from the sample ($> 1\mu$m), and we subtract this value from the difference fluorescence, which yields a mean of zero counts per second away from the target NV spin. As long as this remainder fluorescence (4.3 CPS for this image) times the percent fluorescence variations across the scan region (15%) is smaller than the target NV spin signal - as is the case here - then the target NV spin signal will be the largest feature in the difference fluorescence map. To increase the signal-to-noise ratio (SNR) of magnetic field imaging, we average multiple pixels together to coarse-grain the scan (Fig. 4.7.4, right panel), yielding a scan with 64 pixels across a field-of-view of $\sim 200 \times 200$ nm, with 42 minutes of integration time per pixel providing average SNR of 4.3.

4.7.8   SIMULATION OF SINGLE-SPIN MAGNETIC FIELD IMAGING

The response of the scanning NV magnetometer to a single electronic spin is simulated by considering an electron spin at the origin of a coordinate system with a quantization axis oriented along the $[x, y, z] = [0, -\sqrt{2}, 1]$ direction (to match the orientation in the sample that is measured through ESR measurements using a three-axis Helmholtz coils). Equi-field contours of this target spin's magnetic field are plotted as a function of three-dimensional space (Fig. 4.7.5, displayed here are 2 nT, 4 nT, and 6 nT). Because the sensor NV is first-order sensitive only to magnetic fields along its quantization axis ($[x, y, z] = [0, \sqrt{2}, 1]$), the plotted field contours from the target spin have been
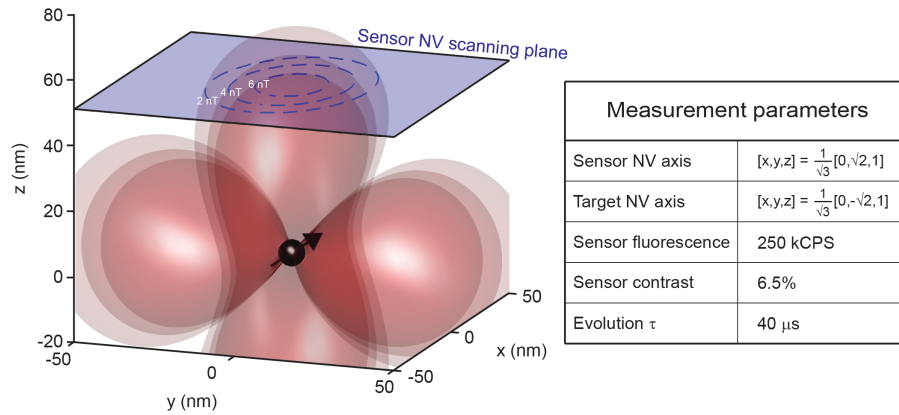
Figure 4.7.5: Simulation of single-spin magnetic field imaging.

projected along the sensor NV quantization axis, which yields the dipole field lobe pattern shown here. Experimental magnetic field scans are taken as plane-cuts of this dipole field pattern above the location of the target spin (at an a-priori unknown distance; plotted is the best fit value of 51 nm). The simulated magnetic field profile is converted into a spatial map of sensor NV fluorescence rate using measured values of the sensor NV fluorescence rate, contrast, and phase evolution time, giving a magnetic field sensitivity conversion factor of −1.8 nT per count per second.

4.7.9 Measuring the variance of a non-initialized spin

If target electron spins cannot be initialized (unlike the target NV spin measured in this work), then the spin's magnetic field will average out to zero over multiple measurements, as at the start of a given measurement ("shot") the target spin has an equal probability of being either up or down. However, if the target's spin's

82
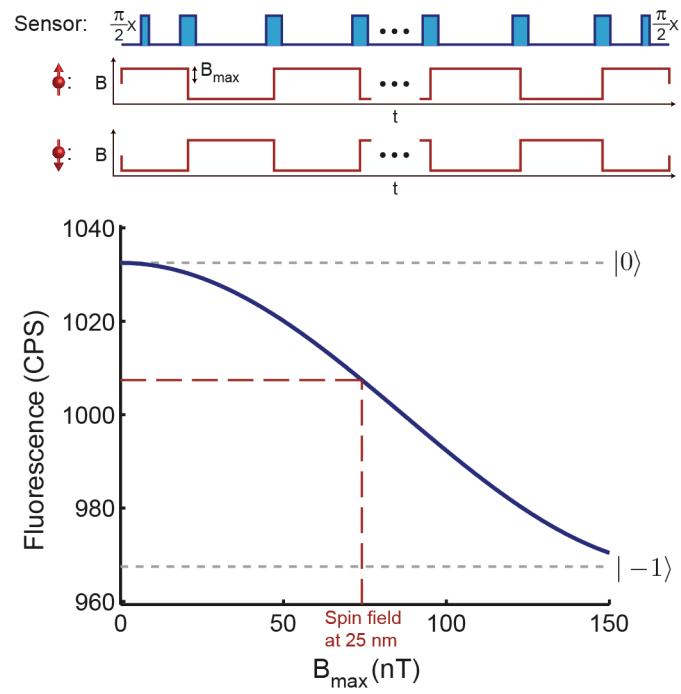
Figure 4.7.6: Measuring the variance of a non-initialized spin.

longitudinal relaxation time is much longer than the magnetometry phase-evolution time τ, within a single shot, then the target spin maintains its statistical polarization, and a net phase shift will be accumulated by the sensor spin. By choosing the axis of rotation of the final $\frac{\pi}{2}$ pulse to match the axis of the first $\frac{\pi}{2}$ pulse, when the accumulated phase shifts from multiple measurement shots are converted to a net population difference, the effect of the target spin's magnetic field no longer cancels out and can be measured via the sensor NV's spin-dependent fluorescence. This scheme effectively measures the variance of the target spin polarization ($\langle \sigma_z^2 \rangle - \langle \sigma_z \rangle^2$, for the thermal state of a target spin) instead of its mean polarization ($\langle \sigma_z \rangle$)

Plotted in Figure 4.7.6 is the sensor NV's response for $\tau = 100\mu s$, plotted is the sensor's NV response to a (driven) target electron spin with random polarization (either up or down) at the measurement's start. (The sensor NV's fluorescence and spin-dependent contrast used are those demonstrated in spin-imaging; Supplementary Fig. 4.7.5.). The magnetic field profile for this driven target spin is a square wave with amplitude B_{max}, which is synchronized to the sensor NV's decoupling scheme. For a sensor-to-target distance of 25 nm (and the same sensor and target spin-quantization axes used in the present work; Supplementary Fig. 5), $B_{max} = 74$ nT, which gives a signal of 25 CPS with respect to the $|0\rangle$ state. Within two seconds of integration time, this signal divided by the measurement's shot noise gives a signal to noise ratio of one.

5

Sub-nanometer resolution in three-dimensional magnetic-resonance imaging of individual dark spins

5.1 Introduction

Magnetic resonance imaging (MRI) has revolutionized biomedical science by providing non-invasive, three-dimensional biological imaging [66]. However, spatial resolution in conventional MRI systems is limited to tens of microns [35], which is insufficient for imaging on molecular and atomic scales. Here we demonstrate an MRI technique that provides sub-nanometer spatial resolution in three dimensions, with single electron-spin sensitivity. Our imaging method works under ambient conditions and can measure ubiquitous 'dark' spins, which

constitute nearly all spin targets of interest and cannot otherwise be individually detected. In this technique, the magnetic quantum-projection noise of dark spins is measured using a single nitrogen-vacancy (NV) magnetometer located near the surface of a diamond chip. The spatial distribution of spins surrounding the NV magnetometer is imaged with a scanning magnetic-field gradient. To evaluate the performance of the NV-MRI technique, we image the three-dimensional landscape of dark electronic spins at and just below the diamond surface and achieve an unprecedented combination of resolution (0.8 nm laterally and 1.5 nm vertically) and single-spin sensitivity. Our measurements uncover previously unidentified electronic spins on the diamond surface, which can potentially be used as resources for improved magnetic imaging of samples proximal to the NV-diamond sensor. This three-dimensional NV-MRI technique is immediately applicable to diverse systems including imaging spin chains, readout of individual spin-based quantum bits, and determining the precise location of spin labels in biological systems.

5.2 SCHEME FOR NANOSCALE MRI WITH NV CENTERS

Atomic-scale magnetic resonance imaging (MRI) would have wide-ranging applications including determining the structure of individual biomolecules [46], imaging the dynamics of bottom-up molecular engineering [81], and achieving site-resolved readout in solid-state quantum simulators [14]. Performing conventional MRI on sub-micron length scales is not possible because macroscopically generated magnetic-field gradients limit spatial resolution, and inductive detection schemes suffer from significant thermal noise [35]. Great progress has been made using scanning-probe-based magnetic gradient techniques, which enable nanoscale MRI, [5, 93] using ultrasensitive force detection at cryogenic temperatures [23, 88] or fluorescence measurements of optically 'bright' spins such as nitrogen vacancy (NV) color centers in diamond [5, 37]. However for most MRI applications, measurements must be taken near room temperature, and nearly all targets of interest contain optically

'dark' spins that are unpolarized or weakly polarized. In this work we demonstrate a technique to perform three-dimensional (3D) MRI with sub-nanometer resolution on dark electronic spins under ambient conditions, using a single NV center near the surface of a diamond as a magnetic sensor of its local environment, together with a scanning-tip magnetic-field gradient to provide high spatial resolution. Our method is compatible with numerous developed methods for bringing imaging targets sufficiently close for NV magnetic detection [40, 62, 64, 65, 94], and extends the reach of nanoscale MRI to previously inaccessible systems in both the physical and life sciences.

The NV-MRI technique combines an NV magnetometer with scanning magnetic-field gradients using an atomic-force microscope (Fig. 5.2.1a). Individual shallowly implanted NV centers (nominal depth of 10 nm) are placed in the focus of a confocal microscope, so that the NV electronic spin can be initialized by optical pumping, used as a sensor to measure nearby dark spins, and read out using time-dependent fluorescence [41]. To image the 3D distribution of dark spins via NV-MRI, we apply a local magnetic-field gradient with a scanning magnetic tip. The magnetic tip provides a narrow spatial volume (a 'resonant slice') in which dark spins are on resonance with a driving radio-frequency (RF) field. Only dark spins within the resonant slice are RF-driven, and thus contribute, to the dark-spin magnetic signal measured by the NV center. The 3D position of the resonant slice is then controllably scanned throughout the sample with angstrom precision by moving the magnetic tip, allowing high-resolution 3D MRI of target dark spins.

To create 3D magnetic resonance images, the detected NV-MRI signal at each magnetic tip position is made conditional on the resonant RF-driving of target dark spins via double electron-electron resonance (DEER) [21, 40, 59, 64]. As illustrated in Fig. 5.2.1b, microwave (MW) pulsing on the NV spin prepares a coherent superposition of NV-spin states with phase φ_{NV} that evolves with evolution time τ_{NV} in proportion to the local magnetic field (projected along the NV quantization axis) from the target dark spins (B_{Dark}). Halfway through τ_{NV},
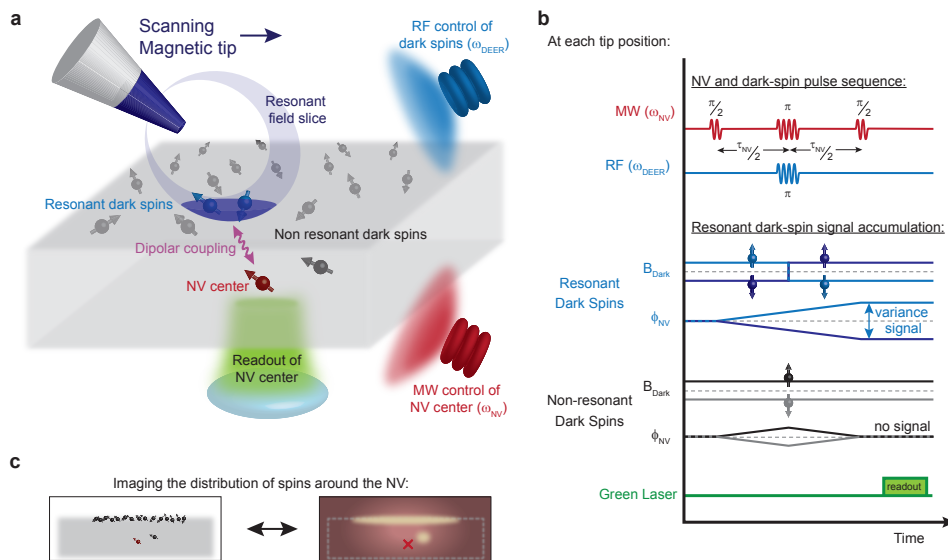
Figure 5.2.1: Dark-spin MRI using scanning gradients and a single NV sensor. (a) Schematic of NV-MRI technique depicting an NV center in diamond situated in a confocal laser spot with nearby dark spins. A scanning magnetic tip is placed within 100 nm of the diamond surface. Applied microwave (MW) and radio frequency (RF) signals allow for independent coherent control of the NV spin and dark spins. By scanning the magnetic tip, non-resonant dark spins (shown in black) are systematically brought into resonance with the RF signal (resonant spins shown in blue) and are measured via optically detected magnetic resonance of the NV sensor. (b) Double electron-electron resonance (DEER) pulse sequences executed at each magnetic tip position. A MW spin-echo sequence is executed on the NV sensor. By synchronizing an RF π pulse on the dark spins with the MW π pulse in the echo sequence, the time-varying magnetic field from the dark spins (BDark) in the resonant slice (light/dark blue) leads to net NV spin phase (τ_{NV}) accumulation, while the magnetic field from non-resonant dark (grey/black) spins is refocused and thus their effects on the NV spin are cancelled, irrespective of the initial polarization state of the dark spins. (c) NV-MRI provides 3D mapping of the distribution of dark electronic spins near the NV sensor (indicated by the red cross), with sub-nanometer resolution (see main text for further discussion).

simultaneous MW and RF π-pulses are applied to the NV and target dark spins respectively, so that φ_{NV} accumulates only for resonant dark spins, and refocuses for off-resonant dark spins. Target dark spins are in an unpolarized mixed state at room temperature, and so across multiple spin measurements, $\langle \varphi_{NV} \rangle = 0$; however, DEER measures $\cos \varphi_{NV}$, which is independent of the dark spins' initial states and consequently measures the variance of the dark spins (coming from magnetic quantum-projection noise).

When scanning the magnetic tip to perform NV-MRI, we simultaneously frequency-lock the applied MW signal to the NV spin resonance [90], which keeps the NV sensor active and also measures the tip-induced frequency detuning. The resulting spatial map of the frequency-locked NV signal experimentally determines the point-spread-function (PSF) for dark-spin imaging. Because dark spins are spatially offset from the NV location and/or distributed over a non-zero volume, the observed dark-spin signal as a function of magnetic tip position is offset and/or broadened from the measured PSF, and the dark-spin spatial distribution can be found via deconvolution (Fig. 5.2.1c). An important feature of our technique is that by directly measuring the dark-spin PSF there is no reliance on magnetic-field modeling or iterative deconvolution schemes that must be simultaneously solved for both an unknown signal and an unknown PSF.

The spatial resolution of NV-MRI is given by $\frac{1}{\tau \gamma \nabla B_{tip}}$ where γ and τ are the target spin's gyromagnetic ratio and spin-interrogation time, respectively, and ∇B_{tip} is the gradient of the tip's magnetic field at the target spin's position projected along the spin's quantization axis. We determined the spatial resolution limit in our setup by measuring ∇B_{tip} using a single NV center, with a relatively long T_2^* coherence time, which allows for a long τ (Fig. 5.2.2). Using a $\tau = 450$ ns Ramsey interferometry sequence, we measured spatial fringes with oscillation periods down to 3.3 ± 0.3 Å(Fig. 5.2.2a), showing that the magnetic tip produces a gradient of 2.4 G/nm and demonstrating that the experimental setup is mechanically stable down to sub-nm length scales. By bringing the tip closer to
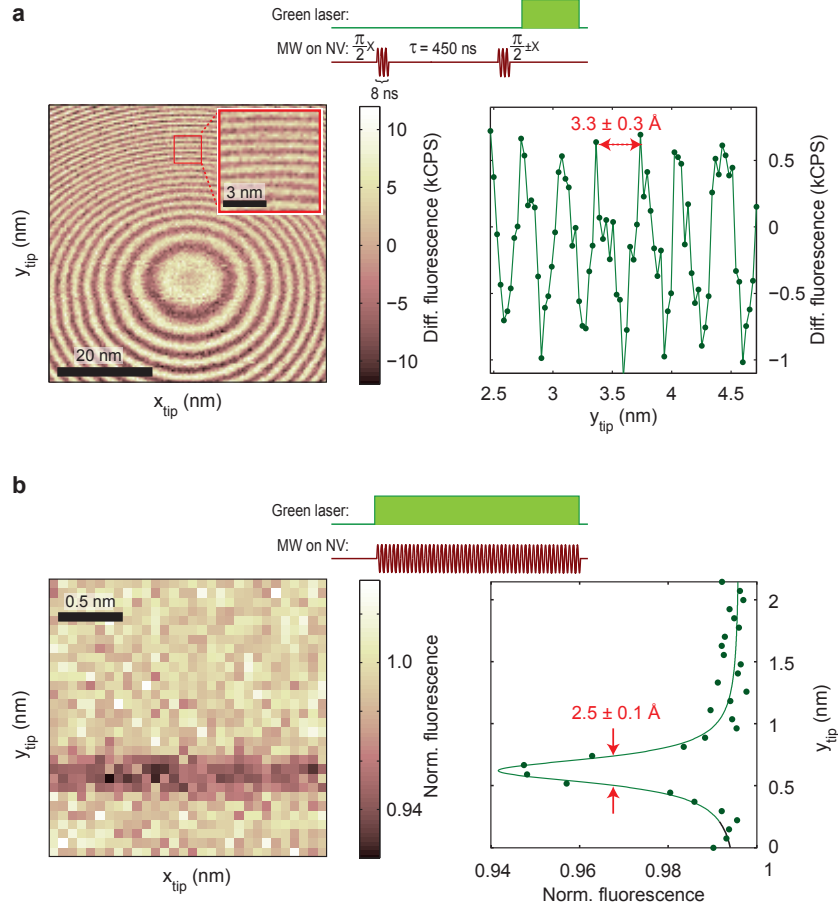
Figure 5.2.2: Scanning gradients with sub-nm MRI resolution. (a) Scanning Ramsey interferometry on a single, shallow NV center in a 0.12-T external magnetic field. As the magnetic tip is laterally scanned over the NV center 50 nm above the diamond surface and near the NV center, the resultant variation in magnetic field at the NV center leads to 2D spatial oscillations in the measured NV Ramsey interferometry fluorescence signal as a function of lateral tip position (center panel). A linecut along the y-direction (30 nm above the diamond surface, right panel) shows oscillations with a period of 3.3 ± 0.3 Å, indicating that the tip-induced magnetic-field gradients are 2.4 G/nm. (b) Continuous-wave ESR magnetometry with an inverse line-width of $\tau = 120$ ns. Magnetic-tip scan with a 20-nm vertical offset from the NV, zoomed into one resonant slice with a full-width-at-half-maximum of 2.5 Å and thus a 12 G/nm tip-induced magnetic-field gradients.

the NV center (Fig. 5.2.2b), we observed gradients of at least 12 G/nm (effective $\tau = 120$ ns); however, vibrations in our experimental setup currently limit the spatial resolution to 2.5 Å. For NV-MRI of dark spins with static tip gradients, the target-spin interrogation time is limited the target spin T_2^* (150 ns), enabling sub-nanometer 3D NV-MRI resolution

5.3 MRI OF ENSEMBLES OF AND INDIVIDUAL DARK SPINS

To demonstrate such sub-nanometer NV-MRI performance, we spatially mapped the spin environment of individual NV centers near a diamond surface. Shallow NV centers are the mainstay for NV-based sensing [38, 40, 62, 64, 65, 79, 80, 94] and quantum-information processing [14, 26], yet their dominant sources of decoherence have not been identified and localized. In the absence of the magnetic tip, we first used DEER spectroscopy and observed a g=2 dark electronic spin bath coupled to shallow NV spins, consistent with previous measurements that did not determine the origin or spatial distribution of these dark spins [64]. We measured g=2 electron-spin resonances for more than 60% of measured NV spins (>30 centers in three diamond samples). We then used the NV-MRI technique to perform 3D imaging of the spatial distribution of these dark electronic spins on and near the diamond surface.

We present imaging experiments mapping the spatial locations of these g=2 dark spins around two separate NV centers by scanning the magnetic tip in three dimensions (Fig 5.3.1). Comparing the measured dark-spin PSF to the observed dark-spin resonance slice (Fig. 5.3.1b and Fig. 5.3.1d, right panel), we find that for both NV centers the dark-spin signal is shifted vertically from the PSF, which shows that the imaged dark spins are located 10 nm and 14 nm above the two NV sensors, respectively (Fig. 5.3.1b and Fig. 5.3.1d). Given the implantation energy used to form the shallow NV spins, the observed dark-spin location is consistent with them being on the diamond surface (nominal depth of 10 ± 3 nm).
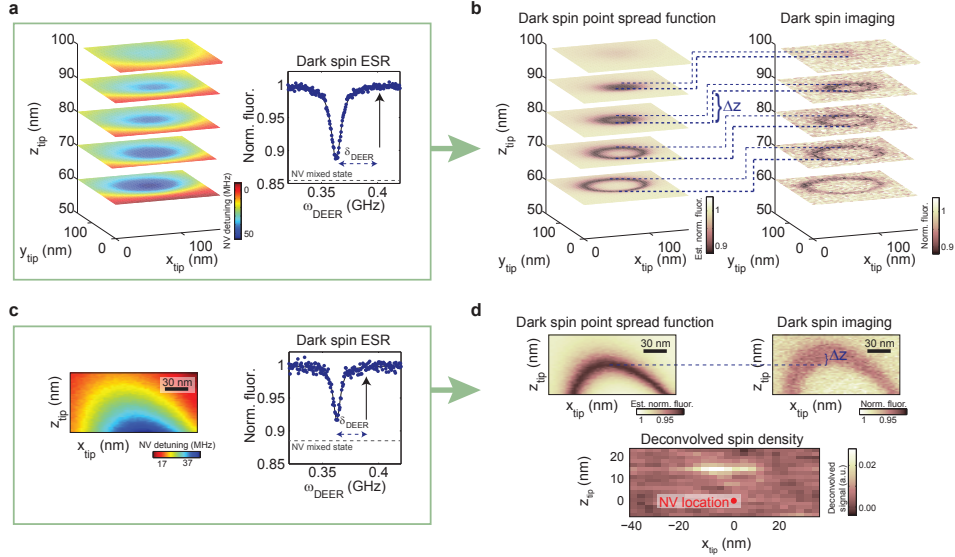
Figure 5.3.1: MRI of ensembles of dark spins at the diamond surface.
(a) Determining the dark-spin NV-MRI point-spread function (PSF). 3D plot of the detuning of the frequency-locked NV microwave signal ω_{NV}, measured by xy scanning of the magnetic tip with variable z offset of 60 nm to 100 nm from the diamond surface (left). This detuning map is combined with the tip-independent dark-spin electron-spin resonance (ESR) spectrum (right) to determine the dark-spin PSF. (b) NV-MRI tomography of dark spins proximal to an individual shallow NV center. Displacement of the dark-spin resonance slice image (right) from the dark-spin PSF (left) indicates the location of the dark spins with respect to the NV center. For a given dark-spin lateral (xy) image, the best match to the dark-spin PSF (determined from the diameter of the resonance circle) is shifted by $\Delta z = 10$ nm, showing that the dark spins lie at or very close to the diamond surface. (c) Dark-spin PSF determination for a second NV center in a vertical (xz) scan. (d) Vertical (xz) NV-MRI of dark spins. Similarly to b, the dark-spin resonance slice image is vertically shifted ($\Delta z = 14$ nm for this NV sensor), again suggestive of surface dark spins. Deconvolving the dark-spin image with the PSF gives the spatial distribution of the nearby dark spins, indicating a surface layer above the shallow NV center.

An image deconvolution along the xz plane (Fig. 5.3.1d) directly shows that the dark spin distribution is spread out in a line, indicating a layer of spins at the diamond surface. This layer of dark spins likely extends further in the xz plane direction, probably with near-uniform coverage over the diamond surface, but laterally distant spins couple more weakly to the single NV and are undetectable when their signal becomes smaller than the measurement noise. As we directly measure the vertical distance between the NV sensor and the dark-spin layer, the density of dark spins in the layer can be found using the dark-spin/NV coupling rate (100 kHz for this NV center) [79]. The extracted two-dimensional dark-spin density is 0.5 spins/nm^2, which for a surface layer corresponds to a single unpaired electron spin every 60 surface atoms.

We also observed that some shallow NV spins are coherently coupled to an individual dark electronic spin, as evidenced by coherent oscillations in the DEER signal as a function of evolution time (Fig. 5.3.2a) [92]. We note that the intensity of the observed dark-spin DEER oscillations cannot be explained by a classical single spin, where the spin is modeled by a magnetic moment that can have an arbitrary, continuous magnetization. In that situation, for an unpolarized dark spin, the measured DEER signal would average over all possible magnetizations and the signal would decay to the NV mixed state. However, for a S = 1/2 quantum spin, measurement of its magnetization can only yield two values, giving single-frequency oscillations in the DEER signal, as we observe. This quantum-projection noise enhances the signal for MRI imaging, and in this case it increases the signal-to-noise of dark-spin imaging by 1.9 compared to a classical variance.

Next, we imaged the 3D location of this coherently coupled dark spin by scanning the magnetic tip both laterally (Fig. 5.3.2b) and vertically (Fig. 5.3.2c) and using the deconvolution method described in Fig. 5.3.1. For vertical imaging, we found an offset of the dark-spin position relative to the NV sensor of $[\Delta y, \Delta z] = [5.1 \pm 0.3, -3.65 \pm 0.05]$ nm, with spatial resolution of 1.5 ± 0.6 nm

Figure 5.3.2: Individual dark-spin MRI. (a) Coherent dynamics from an individual dark spin strongly coupled to a single shallow NV center. Measured oscillations in the NV DEER signal (pulse sequence shown at top) as a function of spin evolution time τ_{NV}. The DEER signal oscillates coherently and overshoots the NV mixed state, indicated strong coupling of the NV to a single nearby dark electronic spin. For comparison, the expected DEER signal is plotted (black solid line) for comparably strong NV coupling to a single classical spin, demonstrating that the dark-spin effect on the NV DEER signal originates from quantum-projection noise. (b) Lateral (xy) NV-MRI of single, coherently coupled dark spin at 50-nm z-axis tip offset; the dark-spin PSF is illustrated in dashed red lines. The vector connecting the center of the PSF circle and the dark-spin resonance gives the lateral shift (Δx,Δy) of the dark spin from the NV. Two distinct resonant slices appear because different sets of dark-spin hyperfine transitions are driven by the applied RF signal. (c) Vertical (yz) NV-MRI of the same coherently coupled dark spin as shown in b. Scanning the magnetic tip across the symmetry plane of the lateral image in b gives the dark-spin vertical shift Δz, in addition to a second measure of Δy. The tip-induced magnetic-field gradient along the z-direction provides 1.5 nm spatial resolution. (d) Illustration of the 3D location of the coherently coupled dark spin relative to the NV sensor, as determined from data in b,c. (e) Lateral (xy) NV-MRI of a second coherently coupled dark spin, imaged with 0.8 nm resolution.

Figure 5.3.2 *(Continued)*

a

Laser:

MW (ω_{NV}): $\frac{\pi}{2}$ π τ_{NV} $\frac{\pi}{2}$

RF (ω_{DEER}):

NV spin echo

P(m_s=0)

mixed state

Exp. classical spin signal

Individual dark spin signal

τ_{NV} (μs)

b

25 nm

y_{tip} (nm)

x_{tip} (nm)

Norm fluor.

0.75   1.0

c

z_{tip} (nm)

10 nm

1.5 nm

y_{tip} (nm)

Norm fluor.

0.9   1.0

z_{tip} (nm)

0.9   1

Norm. fluor

d

NV

Dark spin

$[\Delta x, \Delta y, \Delta z] =$
$[4.0\pm0.4, 5.1\pm0.3, -3.65\pm0.05]$ nm

e

y_{tip} (nm)

0.8 nm

5 nm

x_{tip} (nm)

y_{tip} (nm)

0.9   1

Norm. fluor

95
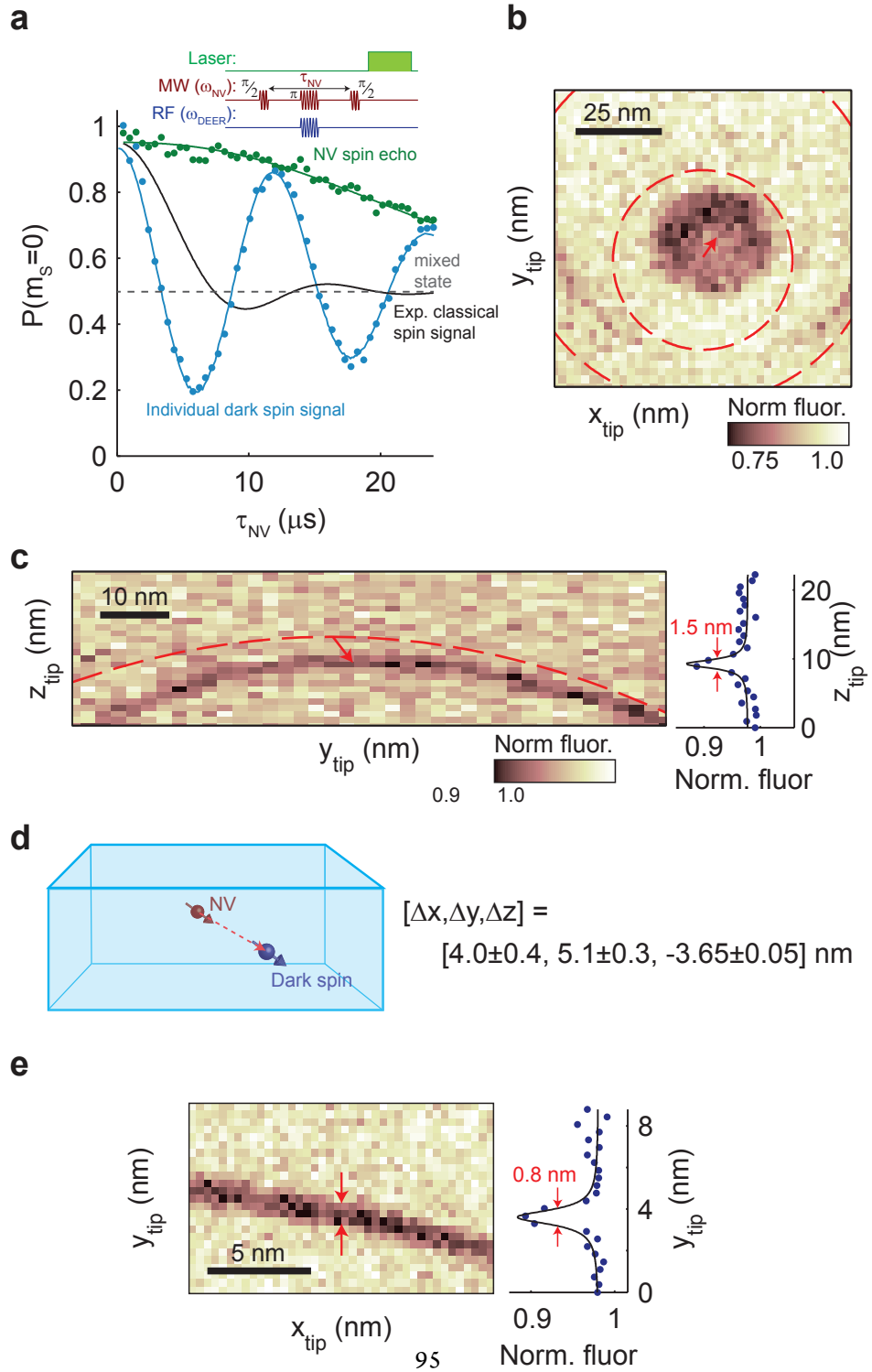
given by the spatial width of the dark-spin resonance. For lateral imaging, the dark-spin signal is not only shifted in location, but is also different in size because the dark spin lies at a different depth than the NV sensor and magnetic-field gradients along the z direction are strong compared to the lateral gradients. To achieve high-precision spin-localization in the lateral dimensions, we fit the center of mass of the measured dark-spin PSF and compared this PSF to the center of the response circle, yielding the lateral offset $\Delta x = 4.0 \pm 0.4$ nm. The location of this coherently coupled dark spin relative to the NV sensor is illustrated in the cartoon in Fig. 5.3.2d. As an additional example, Fig. 5.3.2e displays an xy-plane NV-MRI image of another dark-spin that is coherently coupled to a different NV spin. The lateral spatial resolution in this image is 0.8 ± 0.4 nm, and we observe that its location is consistent with being potentially on the diamond surface.

5.4 Discussion and outlook

Our NV-MRI demonstration provides the first 3D spatial mapping of dark electronic spins on and near a diamond surface, achieving sub-nanometer resolution. We expect that NV-MRI will be applicable to a wide range of systems in both the physical and life sciences that can be placed on or near the diamond surface and then probed under ambient conditions. For example, one-dimensional spin chains have been proposed as a method for transferring quantum information [102]. A key technical challenge that NV-MRI could address is determining the precise (atomic-scale) location of spins along a chain, which critically influences the fidelity of quantum information transfer. Additionally, individual paramagnetic electron spins with long coherence times at room temperature have attracted interest as potential quantum bits [44], but currently such spins cannot be read out individually. NV-MRI would allow for simultaneous control and detection of dark electron spins brought into proximity to NV sensors near the diamond surface. Finally, NV-MRI could image the location of individual electronic spin labels in biological systems, e.g., selectively

attached to specific amino acids on a protein [1], which could aid in the determining the structure of proteins.

Furthermore, studying the nanoscale electronic environment on and near diamond surfaces is critical for understanding and maximizing the coherence of NV sensors and quantum bits. We find that the majority of dark spins near shallow NV centers are at the diamond surface, and thus we expect that passivation of the surface to reduce the dark-spin density will improve NV-based sensing and quantum information applications. Alternatively, dark spins at the surface could be initialized with NV-assisted spin-polarization techniques [8, 58] and then used as a resource for improved sensing: such ancilla sensor spins would effectively amplify magnetic signals [89] from samples placed on [65, 94] or scanned [38, 62] over the diamond surface. In addition, coherently coupled dark spins, which we identified and imaged can potentially be entangled with the NV sensor to achieve Heisenberg-limited sensing [36], thus dramatically increasing metrology performance.

5.5   SUPPLEMENTARY METHODS

5.5.1   SHALLOW NV CENTERS

The NV centers used in this work for dark-spin readout are created by implanting ^{14}N (at $3 \cdot 10^{11}$ cm^{-2} density with 6 keV energy) into electronic grade diamond (Element 6, [100] cut) and annealing the diamond (2 hours at 800°C in vacuum) via previously reported procedures [37, 62]. Waveguiding nanopillars [4] are used to isolate individual NV centers and enhance NV collection rates (200-400 kCPS for single NV centers). We note that the nominal depth of implanted N at 6 keV is 10 ± 3 nm [104], though in reality NV centers can lie deeper in the crystal because of channeling during implantation [97]. The coherence properties of these shallow NV centers exhibited considerable variation, with T_2^* values typically being 500 ns to 1 us long and Hahn-echo T_2 values of roughly 3 to 30 us.

5.5.2 Scanning magnetic gradients

Magnetic tips are optimized from previous iterations of scanning gradients [37]. For all tips used in this work, nickel films are thermally evaporated onto laser-pulled quartz rods, with radii of curvature of 35 nm. In order to minimize off-axis fields that quench NV spin contrast, and are inevitable during tip scanning, the gradient is maximized while minimizing the total value of the tip field. This is accomplished by evaporating a layer of nickel equal to the tip radius of curvature directionally onto its end, resulting in the majority of the tip field coming from as small a volume as possible. Tips are brought within a radius of curvature of dark spins of interest for the highest possible gradients. We note that we observed significant reductions in MRI performance when using films in thickness below 30 nm (due to weak magnetization) or above 40 nm (due to off-axis fields).

5.5.3 Quantifying magnetic field gradients using Ramsey interferometry

We measure the gradient of the magnetic field from our scanning tip by using a Ramsey interferometry sequence applied to a single NV center for a fixed evolution time τ 5.2.2a). Without the presence of the tip, the spin evolves coherently between the $m_S = 0$ and $m_S = 1$ states with a period of $1/\tau$, as long as the detuning from the NV resonance is less than the MW Rabi frequency (31 MHz). In the presence of the magnetic tip (Fig. 5.2.2a) and with fixed τ_{NV}, the tip's magnetic field maps these Ramsey oscillations in frequency space to real space. The spatial period of the fringes therefore measures the local magnetic field gradient (of the field component projected along the NV axis) in the scan range.

5.5.4 Pulsing normalization and references

In order to quantify the NV DEER signal from proximal dark spins, all presented dark spin measurements are normalized by (or are referenced to) the NV sensor running a sequence identical to the DEER sequence, except that the dark-spin

addressing π-pulses are removed. For instance, for DEER spin-echo pulsing the normalized dark-spin signal is found from the fluorescence rate of that measurement divided by the fluorescence rate from a spin-echo measurement on the NV with the same evolution time.

This normalization ensures that any observed dark-spin signal is not the result of (a) reduction of NV fluorescence collection, (b) reduction of NV contrast, (c) reduction of NV coherence, or (d) detuning of NV addressing MWs, all of which in principle can occur when scanning the magnetic tip. Such issues would cause a reduction in the magnitude of the normalized DEER signal we observe, but do not easily allow for any false positive signals. We note that we rule out possible cross-talk between the DEER RFs and the NV MWs (which could potentially lead to fictitious normalized signals). This is done by ensuring that when the RF is detuned from any dark-spin resonances, the fluorescence from the DEER signal is equal to the fluorescence from a NV spin-echo (as can be seen in the normalized fluorescence going to 1 in DEER ESR measurements like those in Fig. 5.3.1a, 5.3.1c).

During pulsing experiments, measurements are also referenced to the fluorescence of the NV spin states ($m_S = 0$ and typically $m_S = 1$), to provide context for the strength of the DEER signal. In particular, to claim coupling of individual dark spins via DEER, it is necessary to prove that the DEER signal goes beyond the NV mixed-state. By measuring the NV reference states by either using an empty pulse sequence or using a single π-pulse, the fluorescence of the DEER can be directly compared to the fluorescence of a mixed NV spin state.

For optimizing signal-to-noise and increasing clarity, we find it useful to vary the phase of the NV readout $\pi/2$ pulse by 180 degrees, so as to probe coherence and DEER originating from both the $m_S = 0$ and $m_S = 1$ states and to ensure that pulse errors are insignificant.

All normalization and references are interwoven in experiments. For pulse evolution measurements (e.g. Fig. 5.3.2a) each signal/reference is measured once at each time interval before incrementing to a new one. For scanning (or frequency sweeping ESR), a fixed pulse sequence runs in the background,

asynchronously from piezoelectric scanners (MW frequency scanning), where the pulse sequence repeats many thousands of times within each pixel (frequency point). By minimizing the time between signal and references, we are able to reject low-frequency common-mode noise such as fluorescence rate drifts and ensure proper normalization.

5.5.5   Precision and accuracy determinations

Unless otherwise specified, error bars on extracted dark spin distances refer to the precision of the measurement. These estimates use the fact that the dominant noise source in NV-based measurements is photon shot noise, which is uncorrelated. Consequently, the noise on different pixels/data points can be well approximated to be independent from one another (particularly when fluorescent rates are normalized to avoid slow-drifts in count rates). Thus, the error induced on distance estimates from these random variables can be found by either using the covariance matrix from regression fitting or by calculating how the χ^2 from a model varies as a function of distance parameters.

Estimating the extent of systematic errors is more difficult. In general, piezoelectric nonlinearities, piezoelectric hysteresis, and errors in point-spread-function determination can all lead to inaccuracies which are unaccounted when estimating measurement precision. In order to provide an upper bound for the contributions of these issues to measurement accuracy, for the single dark spin imaging, we can compare the observed dark-spin coupling rate to the NV (oscillation period in Fig. 5.3.2a) to the calculated magnetic field from an individual Bohr magneton residing at the extracted displacement from the NV (Fig. 5.3.2d), taking into effect the directions of the dark-spin quantization axis and the NV axis. We find the extracted dark-spin coupling rate is 72 kHz and the measured coupling rate is 85 kHz. Because the coupling rate is a strong function of distance ($B \propto r^{-3}$), the agreement between these two coupling rates indicates that the extracted distance is accurate to within 6%.

5.5.6 Dark-spin deconvolution

Deconvolution of the dark-spin imaging in Fig. 5.3.1d is performed using a Weiner deconvolution implemented in MATLAB as has been used and described previously [37].

5.6 Supplementary discussion

5.6.1 Prospects for imaging nuclear spins

NV-based MRI has the potential for imaging of individual nuclear spins with sub-nanometer resolution. Because of the diminished size of the proton gyromagnetic ratio (1/700 smaller than electronic spins), stronger gradients are required to achieve the same resolution as in imaging electronic spins. This decrease in resolution is significantly offset by the longer coherence times of nuclear spins (typically 100x longer), provided that the NV coherence times are sufficiently long to incorporate slow nuclear magnetic resonance π-pulses into AC magnetometry sensing schemes. Nuclear spatial resolution of <1 nm are achievable with the highest demonstrated gradients here (12 G/nm) and the typical T_2^* of nuclear spins (20-50 μs at room temperature [65, 94]). Furthermore, incorporating time-dependent gradients through controlled oscillation of magnetic tips [48] would allow the spatial resolution to be determined by T_2 instead of T_2^*, thereby pushing the capability of NV-MRI to imaging with atomic resolution.

5.6.2 The role of dark-spin interactions in NV-MRI

In general, magnetic dipole-dipole interactions between dark spins can influence the recorded NV-MRI signal in magnetic imaging. For the presented experiments, we operated in a regime where these interactions between the dark spins did not contribute to the signal, so as to make the interpretation of these proof-of-principle experiments more clear and to ensure that the extracted distances only depend on the physical location of the spins.

To achieve this, we first applied a static magnetic field (>100 G), which is significantly stronger than the spins' mutual dipolar interaction strength (≈ 5 G). This static magnetic field defined a quantization axis for the dark spins, so that during each measurement shot dark spins are either aligned or anti-aligned to this axis. This statistical polarization is maintained within the relaxation time of the dark spins ($T_1 \approx$ a few us) and is measured by the NV contingent on the dark-spins being driven by the applied radiofrequency (RF) field. Additionally, we set the Rabi frequency of this RF field to be stronger than the dark spins' collective dephasing rate ($1/T_2^* \approx 7 - 10$ MHz) as demonstrated in the Supp. Fig. 1c. Consequently, for spins in the resonance slice from the magnetic tip, they are effectively always on resonance with the driving RF and thus detected by the NV using double electron-electron resonance (DEER).

The relaxation time of the dark spins (T_1) is also an important parameter in NV-MRI, as in the DEER sequence, to efficiently acquire a dark-spin signal on the NV, the NV-phase-accumulation time should not be longer than the dark-spin T_1. We note that in general the T_1 of dark spins may depend on the presence of magnetic field gradients, as by spatially-shifting the resonances of dark spins via gradients would potentially inhibit dipolar flip-flops between dark spins. By measuring the dark-spin relaxation times as a function of magnetic field gradient, NV-MRI could thus provide a method for studying many-body spin dynamics in solid-state systems.

5.7 SUPPLEMENTARY FIGURES

5.7.1 DEER CHARACTERIZATION OF G=2 SPINS.

(a) DEER-ESR on an NV center, taken by monitoring the drop in NV coherence as a function of dark-spin addressing RF frequency ω_{DEER}. On most shallowly-implanted NV centers, we observe a single resonance peak. (b) Measuring the dark spin g factor. By varying an external field aligned to the NV axis, the dark spin g factor can be found by comparing the NV shift in resonance to the dark spin resonance frequency ω_o. We find a good agreement between the g factors of the NV and the dark spins (limited by accuracy in aligning the magnetic field better than 5 degrees), thus determining the g factor of the spins to be approximately g=2. Our deconvolution scheme uses this relation between NV detuning and DEER detuning for generating the DEER point-spread-function (PSF) from the NV-measured field. (c) Dark-spin Rabi oscillations. For a fixed ω_{DEER} and NV evolution time (τ_{NV}), Rabi oscillations on the dark spins can be observed by varying the length of the DEER π-pulse (τ_{DEER}). For all DEER-ESR measurements in this work, the τ_{DEER} is set equal to a π-pulse. (d) DEER signal as a function of τ_{NV}. By sweeping τ_{NV}, the optimal evolution time can be found by maximizing the signal-to-noise ratio of the DEER signal (fluorescence of the DEER sequence divided by the NV spin echo). In general, the easiest way to optimize the DEER signal is to have initial guesses for τ_{DEER}, and τ_{NV}, and then find ω_{DEER}. At this point τ_{DEER} can be found, and lastly the optimal τ_{NV}. The plotted DEER ESR (a) and DEER Rabi (c) are taken after this optimization and are from a different NV center to that shown in (b).
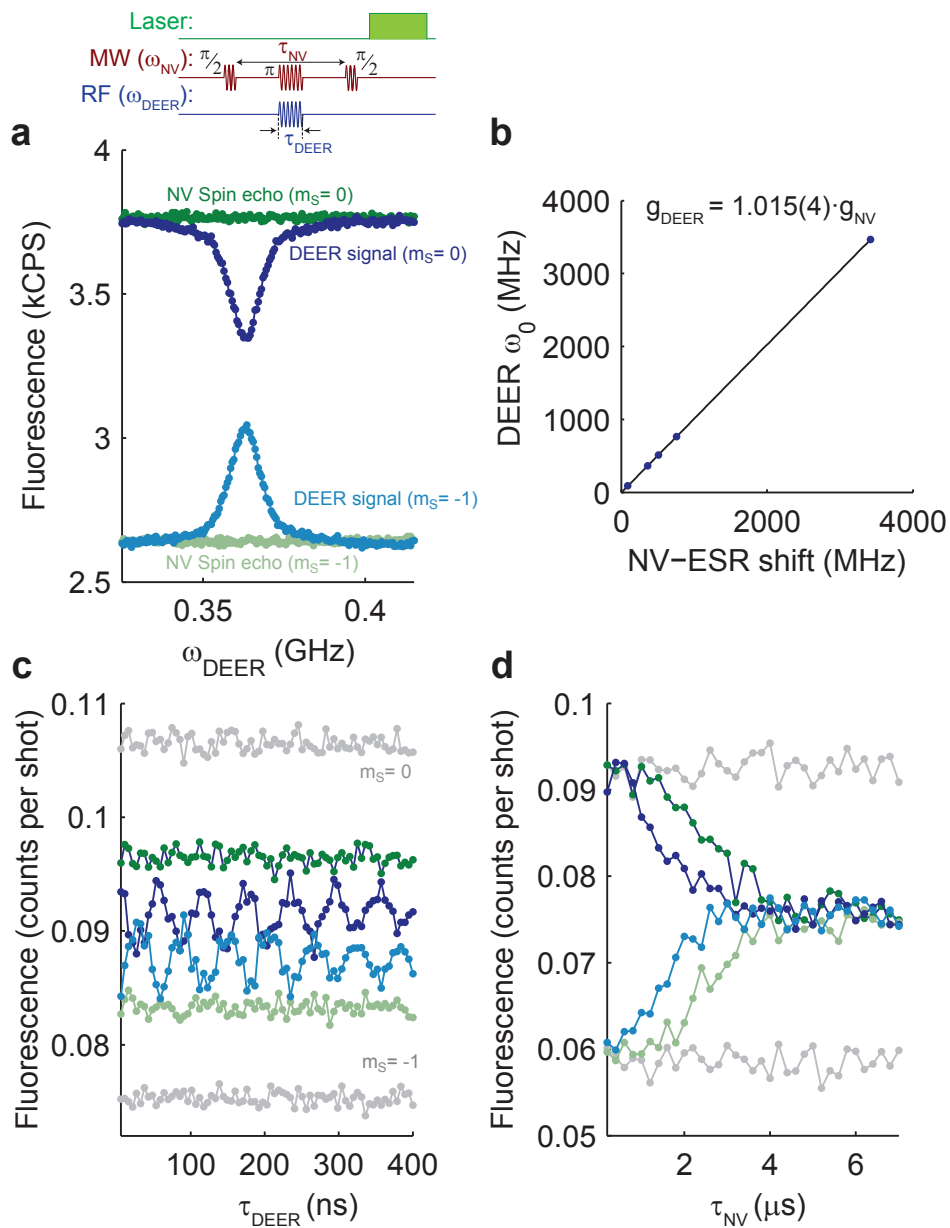
Figure 5.7.1
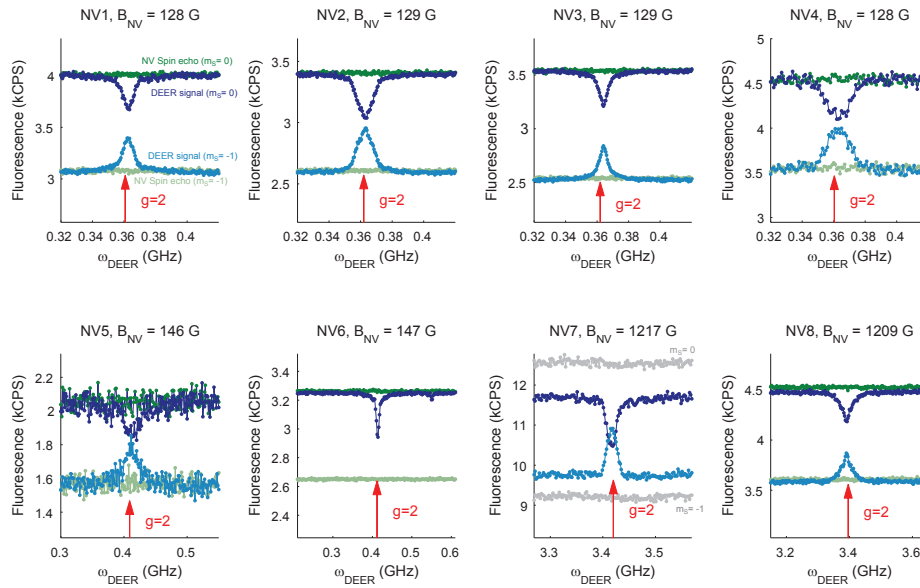
Figure 5.7.2

5.7.2 G=2 DEER RESONANCES ON MANY NV CENTERS.

DEER ESR spectra for eight different NV centers are shown, all exhibiting a single pronounced peak at the g=2 peak (red arrows) for the magnetic field used in each measurement. The magnetic field is found from the shift in the NV resonance from the NV zero-field splitting, noting that the field is aligned to the NV axis. NV1 is the center used in Fig. 3 5.3.1c and 5.3.1d, NV3 is used in Fig. 5.3.1a and Fig. 5.3.1b, and NV7 is used in Fig 5.3.2e.

5.7.3 LOCKING ω_{NV} TO THE NV RESONANCE AS THE TIP IS SCANNED.

To both maintain dark-spin readout and to determine the dark-spin point-spread-function, we lock the frequency of the NV-addressing MWs (ω_{NV}), to the NV resonance [90] (a) Single-sideband-mixed NV-ESR. To get a linear fluorescence response to detuning, we frequency modulate the NV-addressing MWs by $\pm\delta\omega$ (typ. 5-7 MHz, dictated by the width of the NV-ESR) . We note that since we also simultaneously (within a few μs) need ω_{NV} to be on NV-resonance to perform DEER sequences, we use an IQ mixer (Marki-1545LMP) to rapidly change detuning. (b) Feedback signal and procedure. The difference between the modulated signals is taken, and the NV is on resonance when the difference fluorescence is equal to zero, provided the resonance is within the dynamic range ($\approx 2\delta\omega$) of the feedback. Asynchronously to scanning protocols, we run a software PI feedback loop, which feeds back on ω_{NV} to minimize the continuously measured difference counts δC. (c) Scanning the magnetic tip with feedback off (ω_{NV} fixed to ω_o, arrow in a) yields a single resonance slice where NV fluorescence decreases (normalized to the fluorescence of the $m_S = 0$ state). (d) However, when the frequency is locked, the difference counts are minimized, and ω_{NV} as a function of position directly yields the tip field (given the gyromagnetic ratio of the NV).

a

Fluorescence (CPS)

$\times 10^4$

$+\delta\omega$ $-\delta\omega$

ω_0

ω_{NV} (GHz)

b

Diff. fluor. (CPS)

$\times 10^4$

δC

Setpoint

Feedback loop

ω_{NV} (GHz) $\delta\omega = -p\cdot\delta C$

c

Feedback off

y_{tip} (nm)

x_{tip} (nm)

Diff. fluor (CPS)

-10 -5 0 $\times 10^3$

d

Feedback on

y_{tip} (nm)

x_{tip} (nm)

ω_{MW}(GHz)

2.46 2.5

Figure 5.7.3

a

NV resonance

b

NV coherence
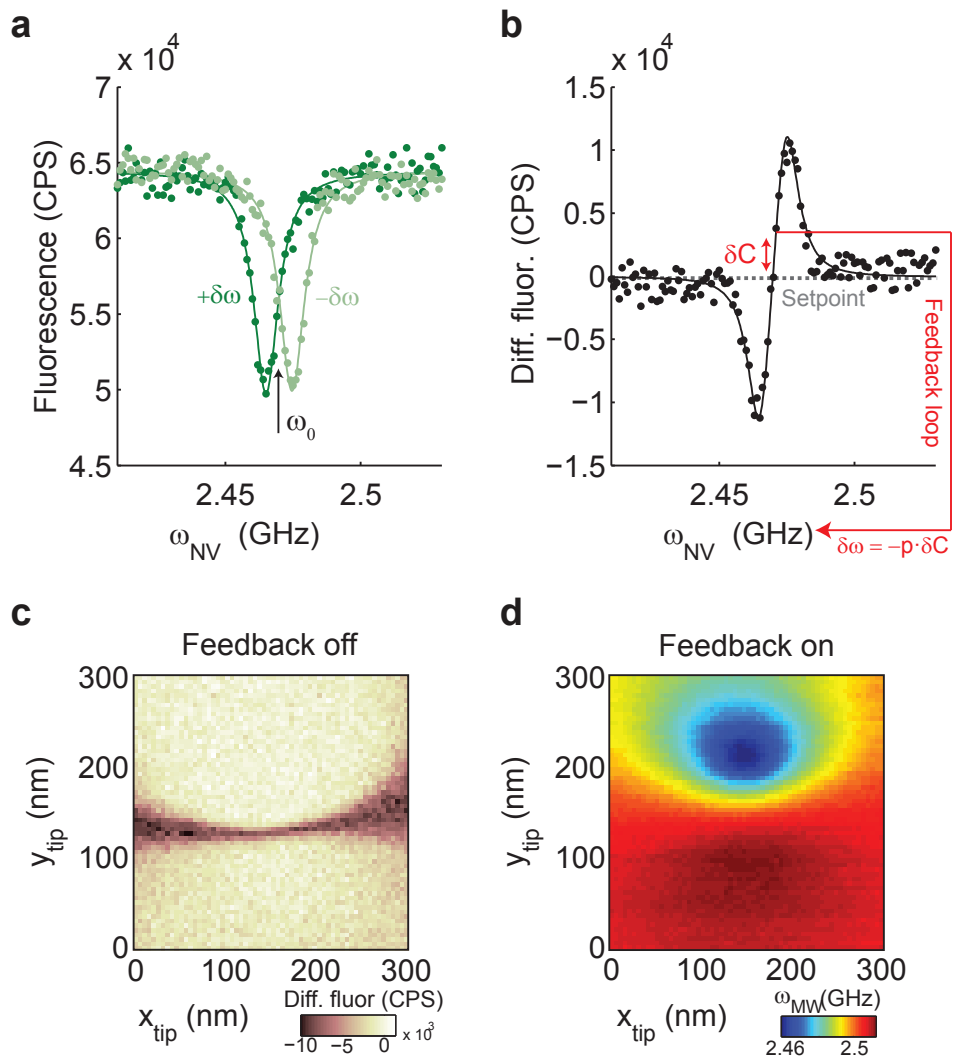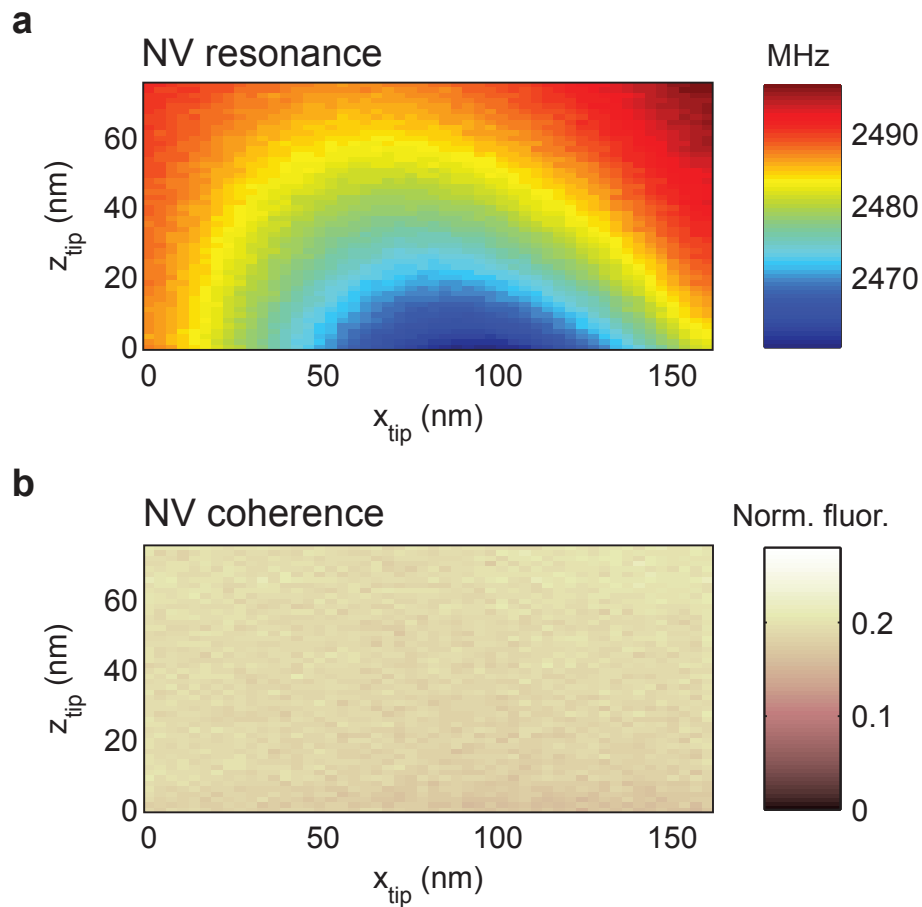
Figure 5.7.4

5.7.4 Maintaining dark spin readout during magnetic tip scanning.

A critical requirement for our dark spin imaging is that the dark-spin readout of the NV sensor is maintained while we scan the magnetic field gradient. Consequently during tip scanning, in addition to measuring the DEER signal and locking ω_{NV} to the NV resonance, we also simultaneously measure the NV coherence by dividing the fluorescence of two spin-echo sequences with the final $\pi/2$ pulses phase shifted by 180 degrees. This is equivalently a measure of the maximum DEER signal, and thus the dark-spin readout fidelity. (a) Measurement of the NV resonance as the tip is scanned (same data as in Fig.

5.3.1c), by frequency-locking ω_{NV}. (b) NV coherence as the tip is scanned. During the same measurement scan, we see that the NV coherence is essentially constant and is nearly equal to the out-of-contact value (which is 0.24, twice the ratio between the $m_S = 0$ state and the mixed state as shown Fig. 5.3.1c). The constant NV coherence ensures that the magnitude of the DEER signal can be properly compared to the PSF in deconvolution.
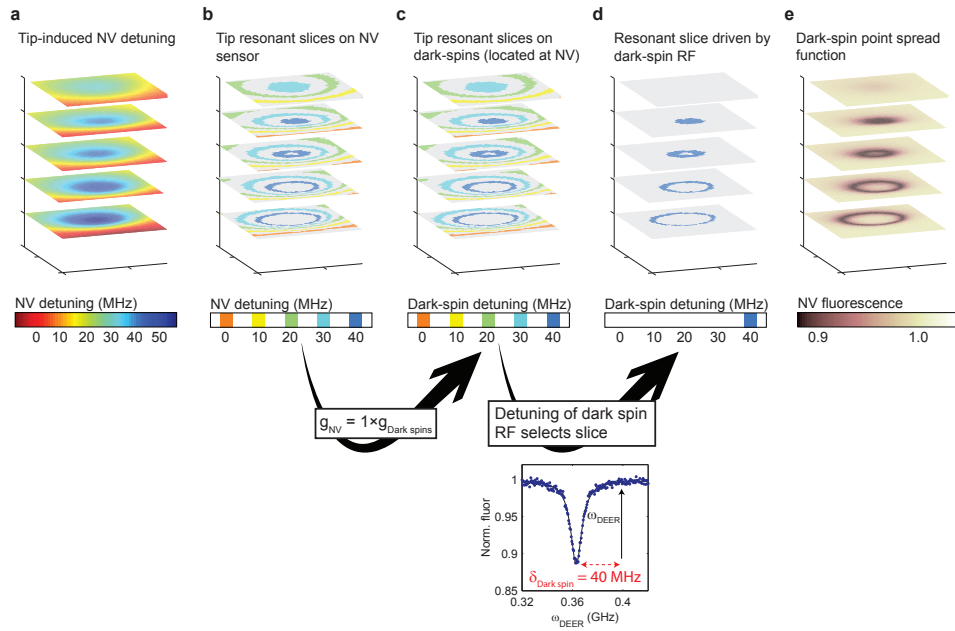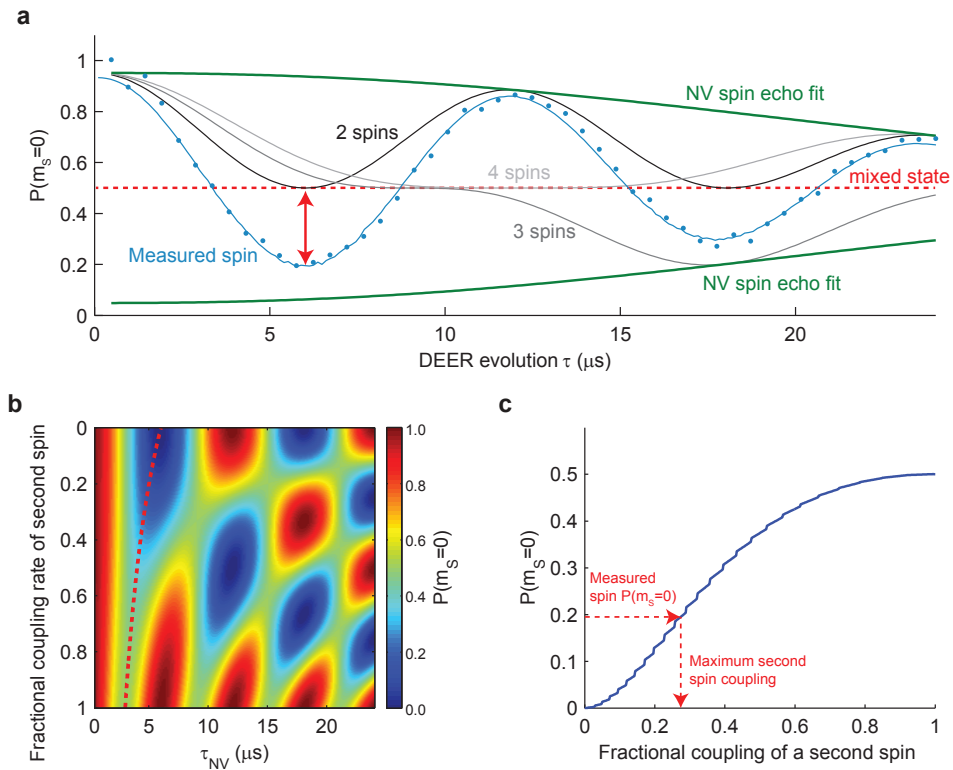
Figure 5.7.5

5.7.5 DETERMINING THE DARK-SPIN POINT SPREAD FUNCTION.

The point-spread-function (PSF) for dark-spin imaging can be determined from
the measured tip-induced detuning on the NV and the dark-spin ESR as follows:
(a) The tip-induced NV detuning is measured by frequency-locking the
NV-addressing MWs to the NV resonance during tip scanning and recording the
applied MW frequency as a function of tip position. (b) This detuning map is
equivalent to a map of resonant slices with finite width. To illustrate this, the
colorscale of the tip-detuning map in a is modified to have discrete values of
width of 4 MHz and spaced at 10 MHz intervals, illustrating resonant slices with
detunings of 0, 10, 20, 30, and 40 MHz. (c) Because the relative g-factors of the
dark spins and NV centers are known, the spatial map of NV resonant slices can
be converted to a spatial of map of dark-spin slices by simply rescaling of the
magnitude of the detuning. (In this situation $g_{NV} = g_{Darkspins}$ so the resonant
slices are the same.) Because these dark-spin slices are measured using the NV
center, they correspond to situation where dark-spins are located at the NV

110

position. (d) During scanning, an RF frequency (ω_{DEER}) is applied to the dark spins with a fixed detuning from the tip-independent dark spin resonance ($\delta_{DEER} = 40$ MHz). Thus, dark spins located at the NV center in the 40 MHz detuning slice are on resonance and are driven and detected by the NV sensor. This resonant slice gives the spatial location of the PSF for dark-spin imaging: if dark-spins are shifted from the NV center, the measured dark-spin response will correspondingly be shifted from the PSF; if the dark-spins are spatially spread over a non-zero volume, the dark-spins response will be the PSF smeared out over this volume. (e) By mapping the dark-spin detuning map to the full ESR spectrum, we obtain the quantitative PSF, which contains both the width of the expected dark-spin response, and the intensity of the dark-spin induced NV fluorescence.

Figure 5.7.6

5.7.6 DEER ON INDIVIDUAL SPINS.

(a) DEER data (blue dots) and simulations (solid lines) as a function of evolution time for one to few, equally coupled spins. For one coupled spin, the NV $P(m_S = 0)$ oscillates with a single frequency between 1 and 0, and overshoots the mixed state. This full amplitude, single frequency oscillation arises because the DEER signal is independent of sign of the field, and there is only one dipolar coupling frequency between the dark spin and the NV sensor. For more than one spin (2, 3, and 4 plotted), multiple frequency components are observed in the DEER signal because each different bath configuration contributes a different frequency oscillation, and the time-averaged DEER signal samples all bath configurations. In general, for more than one equally coupled spin, the

highest frequency of the DEER signal does not go past the NV mixed state, and so DEER signals from individual spins can be positively identified. (b) In general, the coupling between proximal dark spins and the NV are unequal because the dark spins are located at different positions. As a result, intermediate behavior between the cases in a is observable. In a general situation, one dark spin may be more strongly coupled to the NV than other dark spins, and the dark-spin oscillations will overshoot the mixed state, however they will not completely reach the $m_S = -1$ state. The value of the $P(m_S = 0)$ overshoot, however can be used to put an upper bound on the coupling strength of additional spins beyond the dominantly coupled spin. Because the signal contribution from different spins add in quadrature, the strongest extra spin contribution occurs for n = 2 spins. Plotted in b is the simulated DEER signal as a function of evolution time and the fractional coupling rate of a second, weaker coupled spin (dominant spin coupled with 85 kHz). As the fractional coupling goes from 0 to 1, the amplitude of the highest frequency component (values along the red-dashed line) of the dark-spin oscillations goes from 1 to 0.5 in agreement with the time traces in a. (c) $P(m_S = 0)$ as a function of fractional coupling of a second spin is plotted along the dashed line in b, corresponding to the first minimum in the DEER evolution. Because the measured dark-spin oscillations in a reach $P(m_S = 0)$ = 0.2, the maximum contribution from a second spin is $0.27 \cdot 85$ kHz, and thus the more strongly coupled spin is more than three times stronger than any other driven spins. From this upper bound of coupling of a second spin, we say the dark spin signal originates from a single spin. We note that upper bound likely overestimates the contribution from additional spins because the amplitude of the dark-spin signal can equally be explained by a driving fidelity of the single dark spin less than one. For this spin, because we only drive 4 out of the 5 observed spin transitions, this is likely the case, and we can simulate the measured signal with a single spin with spin-flip probability of 85%.
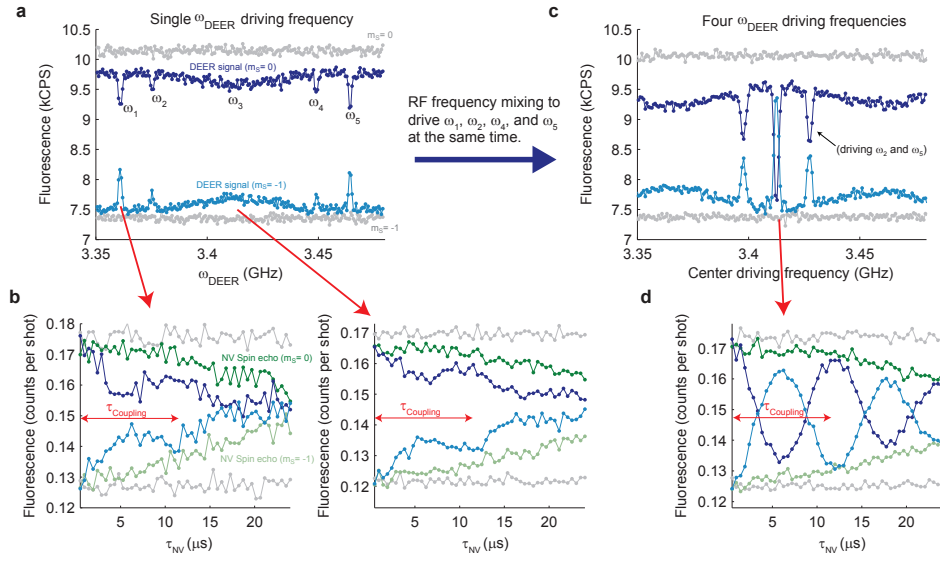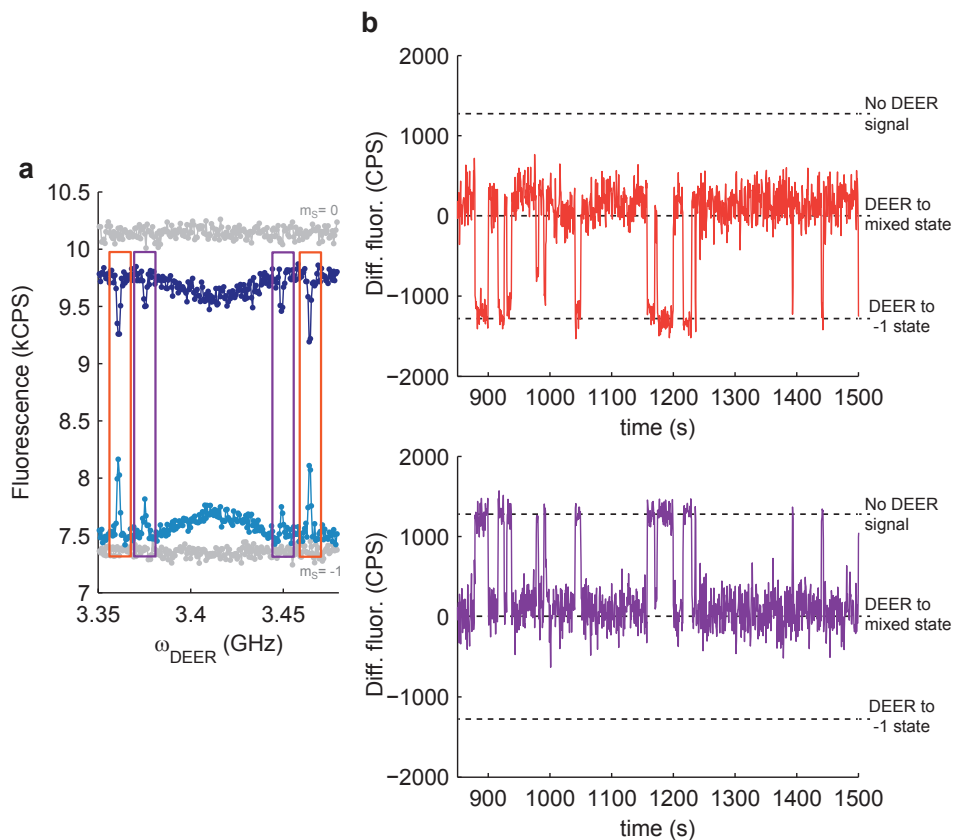
Figure 5.7.7

5.7.7 DEER ON THE IMAGED INDIVIDUAL DARK SPIN.

(a) DEER ESR for the individual dark spin imaged in Fig. 5.3.2 a-d. Five different resonances are observed, suggesting a hyperfine structure: there are two peaks separated by 104 MHz (ω_1, ω_5), two peaks separated by 74 MHz (ω_2, ω_4), and one broad peak centered at g=2 (ω_3, the external field is 1.22 kG). The hyperfine structure is qualitatively similar to ^{14}N P1 centers in diamond, which have an I=1 nuclear spin, and due to an anisotropic hyperfine interaction and Jahn-Teller distortions, lead to 5 peaks. The observed splitting of this dark spin, however, is roughly a factor of two smaller than the ^{14}N P_1 centers, so probably is associated with a different defect in diamond, but perhaps also involving a nitrogen atom and tetrahedral symmetry. We speculate that the middle, g=2 peak is significantly broader because it interacts resonantly with other nearby g=2 spins. (b) DEER signal from driving any peak individually. When any of the 5 peaks are individually driven and the DEER evolution time is swept, coherent oscillations in the DEER are observed. Plotted are DEER oscillations from ω_1 and ω_3, which show the same coupling rate $1/\tau_{Coupling}$, suggesting that the peaks

all come from the same spin. (c) Driving multiple transitions simultaneously. To enhance DEER signal and to conclusively prove that the signal comes from an individual spin, four transitions are simultaneously driven $(\omega_1,\omega_2,\omega_4,\omega_5)$, by frequency mixing two arbitrary-waveform-generated sinusoids into ω_{DEER}. When ω_{DEER} is centered (at ω_3), all four transitions are driven and a DEER signal which dramatically overshoots the mixed state is observed. Because the signal strength adds linearly (going past the mixed state) and not in quadrature (approaching the mixed state), we show the four peaks are not independent, and therefore share a similar origin. If ω_{DEER} is detuned by the difference between $\pm(\omega_1 - \omega_2)$, the mixed frequencies are resonant with only two of the four peaks (ω_1 and ω_4) or (ω_2 and ω_5). (d) DEER driving four transitions as a function of τ_{NV}. The same coherent oscillations as in a are observed, but this time well exceed the NV mixed state demonstrating an individually coupled spin.

Figure 5.7.8

5.7.8   Time-resolved dynamic switching between dark spin states.

(a) DEER ESR of the dark spin imaged in Fig. 5.3.2 a-d. Pairs of peaks (outer peaks in red or inner peaks in purple) are driven by frequency mixing ω_{DEER} for the measurements in b. (b) Switching between pairs of peaks as a function of time. The DEER fluorescence for each pair of peaks (difference between the light blue and dark blue curves in a), are plotted as function of time, where 0 difference counts corresponds to a DEER signal which brings the NV to a mixed state. Most of the time the measured DEER signal is in this intermediate region, however there are occasional switches where a full DEER signal (going all of the way to

116

the $m_s = 1$ state) is observed in the outer peaks. At the same period in time, the DEER signal in the inner peaks vanishes, and the anti-correlation of the two time traces demonstrates that the same spin leads to all four resonances, and the discreteness of the switching provides further proof that it is a single spin. We speculate that the origin of the pairs of peaks could be a dynamic Jahn-Teller distortion, as the spin-state lifetime in the outer peaks (up to tens of seconds), is may be too long for a hyperfine state. When all four transitions are driven, the DEER signal is constant in time (data not shown).
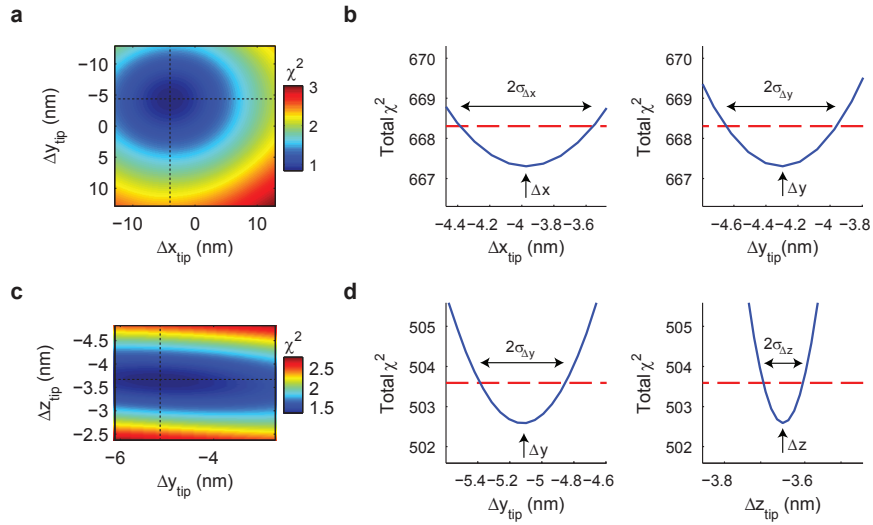
Figure 5.7.9

5.7.9 DETERMINING DARK SPIN LOCATION WITH HIGH PRECISION.

The location of the dark spin imaged in Fig. 5.3.2b (lateral imaging) and Fig. 5.3.2c (vertical imaging), can be quantitatively found by varying the response point-spread-function (PSF) location (away from $[\Delta x, \Delta y, \Delta z] = [0,0,0]$, which corresponds to the NV location) and minimizing the χ^2 of a comparison between the model PSF and the data. The standard error on each pixel σ is found by taking the standard deviation of regions of each image which do not contain any resonant DEER signal. For the vertical imaging, the PSF has the same shape as the data, and so it can be used directly for the comparison. For the horizontal imaging, because the z-gradients are large, and the dark spin is shifted vertically from the NV, the PSF has a different size, and so a point spread function is modeled to be a circle with a Lorentzian profile, with a width matching the DEER image. (a) Lateral imaging χ^2 map for translating the response function with respect to the DEER imaging. The χ^2 is normalized by the number of data points minus the degrees of freedom in the translation. The minimum value of the χ^2 is 0.85 indicating the model matches the data well and the errors are well

estimated. (b) Line cuts of the total χ^2 across the minimum χ^2 value in a. The location of the minimum χ^2 is found to be $[\Delta x, \Delta y] = [\text{-4.0, -4.2}]$ nm, giving the offset of the dark spin from the NV sensor. The standard error of the location determination is given by how much Δx (Δy) is varied to increase the total χ^2 by 1. This is found to be 0.4 nm (0.3 nm). (c) χ^2 map as in a, but for the vertical dark spin imaging (minimum value of 1.35). Here, the map is asymmetric in y and z because the PSF is narrower along the z direction, and is thus more sensitive to vertical displacements. (d) Line cuts of the total χ^2 across the minimum χ^2 value in c. As in b, the location and standard error of the estimate of location are found for the vertical deer imaging to be $[\Delta y \pm \sigma y, \Delta z \pm \sigma z] = [-5.1 \pm 0.3, -3.65 \pm 0.05]$ nm. We note that the two estimates for Δy differ because for lateral imaging, the exact PSF is not known, and in general is not symmetric about the y-axis. Consequently, it is not strictly accurate to take the center of the PSF response and compare that to the center of the DEER signal (as this analysis does in a), if the dark spin is positioned at a non-zero offset Δz. For this reason, we quote the value for Δy determined in the vertical direction, which does not have this issue. On the other hand, we note that extracting Δx from the lateral imaging can be done accurately, since the dipole field and NV axis are symmetric around $\Delta x = 0$, and so the offset of the center of the PSF and the dark spin image in the x-direction is an accurate measurement of the dark spin offset.
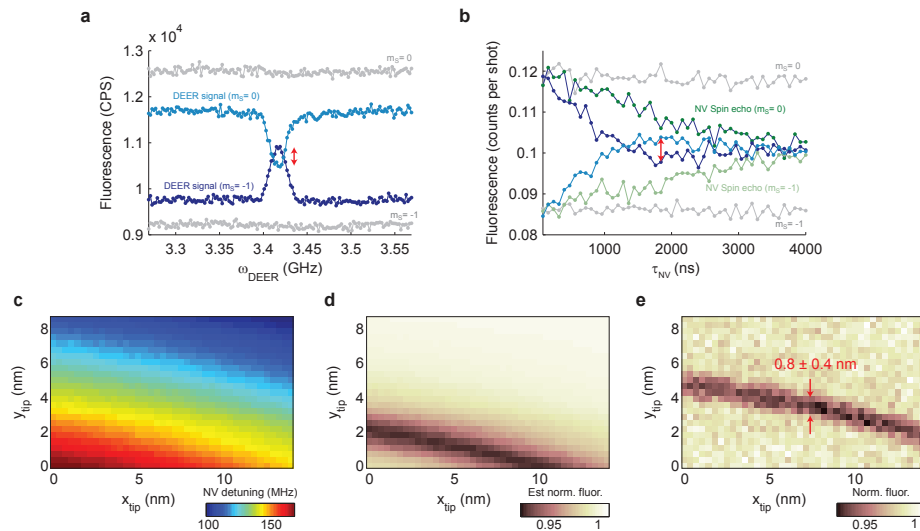
Figure 5.7.10

5.7.10   Scanning DEER another single dark spin.

(a) Plotted is the DEER ESR of the NV in Fig. 5.3.2e which is coupled to an individual dark spin. In contrast to the dark spin in Fig. 5.3.2d, this dark spin has a single resonance peak at g=2, similar to the spins imaged Fig. 3. (b) Varying the DEER evolution time (τ_{NV}), showing an overshoot in the DEER signal indicating a dominantly-coupled individual spin. As the DEER signal does not completely overshoot the mixed state, there are likely additional spins coupled more weakly. (c) Lateral magnetic tip imaging and the resulting frequency-locked detuning of ω_{NV}. (d) DEER PSF determined from the DEER ESR in a and tip-induced detuning in c, following the procedure in Fig. 5.3.1. e Lateral DEER MRI of the dark spin. We observe a high resolution MRI slice with full-width-at-half-maximum of 0.8 ± 0.4 nm along the y direction, demonstrating sub-nanometer lateral spatial resolution. The dark spin DEER signal vanished from the NV before vertical scans could be taken to locate the spin three dimensions as done in Fig. 5.3.2. Nevertheless, the fact that the observed DEER is sharper than the PSF suggests that the dark spin is closer to

the tip than the NV, since the gradients are dramatically stronger near the tip. The observed lateral offset in the DEER signal from the PSF can also be explained by a vertical shift, as this image is a very small section in a DEER resonance ring, the diameter of which varies strongly with z distance (as see in Fig. 5.3.2 b-c).

References

[1] C. Altenbach, T. Marti, H. G. Khorana, and W. L. Hubbell. Transmembrane protein structure: spin labeling of bacteriorhodopsin mutants. *Science*, 248(4959):1088–1092, 1990. URL http://www.sciencemag.org/content/248/4959/1088.abstract.

[2] D. D. Awschalom, D. Loss, and N. Samarth. *Semiconductor Spintronics and Quantum Computation*. 2002.

[3] P. B. Ayscough and C. S. Lai. *Spin Labels: Biological Systems*. RCS Publishing,, 1985.

[4] T. M. Babinec, B. J. M. Hausmann, M. Khan, Y. Zhang, J. R. Maze, P. R. Hemmer, and M. Loncar. A diamond nanowire single-photon source. *Nature Nanotech.*, 5:195–199, 2010. URL http://dx.doi.org/10.1038/nnano.2010.6.

[5] G. Balasubramanian, I. Y. Chan, R. Kolesov, M. Al-Hmoud, J. Tisler, C. Shin, C. Kim, A. Wojcik, P. R. Hemmer, A. Krueger, T. Hanke, A. Leitenstorfer, R. Bratschitsch, F. Jelezko, and J. Wrachtrup. Nanoscale imaging magnetometry with diamond spins under ambient conditions. *Nature*, 455(7213):648–651, 2008.

[6] G. Balasubramanian, P. Neumann, D. Twitchen, M. Markham, R. Kolesov, N. Mizuochi, J. Isoya, J. Achard, J. Beck, J. Tissler, V. Jacques, P. R. Hemmer, F. Jelezko, and J. Wrachtrup. Ultralong spin coherence time in isotopically engineered diamond. *Nat Mater*, 8(5):383–387, 2009.

[7] C. Barthel, D. J. Reilly, C. M. Marcus, M. P. Hanson, and A. C. Gossard. Rapid single-shot measurement of a singlet-triplet qubit. *Phys. Rev. Lett.*, 103(16):160503, Oct 2009. URL http://dx.doi.org/10.1103/PhysRevLett.103.160503.

[8] C. Belthangady, N. Bar-Gill, L. M. Pham, K. Arai, D. Le Sage, P. Cappellaro, and R. L. Walsworth. Dressed-state resonant coupling between bright and dark spins in diamond. *Phys. Rev. Lett.*, 110(15): 157601, 2013. URL http://link.aps.org/doi/10.1103/PhysRevLett.110.157601. PRL.

[9] F. Bloch. Nuclear induction. *Phys. Rev.*, 70:460–474, Oct 1946. doi: 10.1103/PhysRev.70.460. URL http://link.aps.org/doi/10.1103/PhysRev.70.460.

[10] H. Bluhm, S. Foletti, I. Neder, M. Rudner, D. Mahalu, V. Umansky, and A. Yacoby. Dephasing time of gaas electron-spin qubits coupled to a nuclear bath exceeding 200μs. *Nature Physics*, 7:109–113, February 2011. doi: 10.1038/nphys1856.

[11] C. Bradac, T. Gaebel, N. Naidoo, M. J. Sellars, J. Twamley, L. J. Brown, A. S. Barnard, T. Plakhotnik, A. V. Zvyagin, and J. R. Rabeau. Observation and control of blinking nitrogen-vacancy centres in discrete nanodiamonds. *Nature Nanotech.*, 5:345–349, 2010. URL http://dx.doi.org/10.1038/nnano.2010.56.

[12] B. C. Buchler, T. Kalkbrenner, C. Hettich, and V. Sandoghdar. Measuring the quantum efficiency of the optical emission of single radiating dipoles using a scanning mirror. *Phys. Rev. Lett.*, 95:063003, 2005. URL http://dx.doi.org/10.1103/PhysRevLett.95.063003.

[13] D. Budker, W. Gawlik, D. F. Kimball, S. M. Rochester, V. V. Yashchuk, and A. Weis. Resonant nonlinear magneto-optical effects in atoms. *Reviews of Modern Physics*, 74(4):1153–1201, 2002. RMP.

[14] J. Cai, A. Retzker, F. Jelezko, and M. B. Plenio. A large-scale quantum simulator on a diamond surface at room temperature. *Nat. Phys.*, 9(3): 168–173, 2013. ISSN 1745-2473. URL http://dx.doi.org/10.1038/nphys2519. 10.1038/nphys2519.

[15] A. M. Chang, H. D. Hallen, L. Harriott, H. F. Hess, H. L. Kao, J. Kwo, R. E. Miller, R. Wolfe, J. van der Ziel, and T. Y. Chang. Scanning hall probe microscopy. *Appl. Phys. Lett.*, 61(16):1974–1976, 1992.

[16] B. M. Chernobrod and G. P. Berman. Spin microscope based on optically detected magnetic resonance. *Journal of Applied Physics*, 97(1):014903–3, 2005.

[17] L. Childress, M. V. Gurudev Dutt, J. M. Taylor, A. S. Zibrov, F. Jelezko, J. Wrachtrup, P. R. Hemmer, and M. D. Lukin. Coherent dynamics of coupled electron and nuclear spin qubits in diamond. *Science*, 314(5797): 281–285, 2006. doi: 10.1126/science.1131871. URL http://www.sciencemag.org/content/314/5797/281.abstract.

[18] A. Cuche, A. Drezet, Y. Sonnefraud, O. Faklaris, F. Treussart, J.-F. Roch, and S. Huant. Near-field optical microscopy with a nanodiamond-based single-photon tip. *Opt. Express*, 17:19969–19980, 2009. URL http://dx.doi.org/10.1364/OE.17.019969.

[19] G. de Lange, Z. H. Wang, D. Riste, V. V. Dobrovitski, and R. Hanson. Universal dynamical decoupling of a single solid-state spin from a spin bath. *Science*, 330:60–63, 2010. doi: 10.1126/science.1192739.

[20] G. de Lange, D. Ristè, V. V. Dobrovitski, and R. Hanson. Single-spin magnetometry with multipulse sensing sequences. *Physical Review Letters*, 106(8):080802, 2011.

[21] G. de Lange, T. van der Sar, M. Blok, Z.-H. Wang, V. Dobrovitski, and R. Hanson. Controlling the quantum dynamics of a mesoscopic spin bath in diamond. *Sci. Rep.*, 2, 2012. URL http://dx.doi.org/10.1038/srep00382. 10.1038/srep00382.

[22] C. L. Degen. Scanning magnetic field microscope with a diamond single-spin sensor. *Appl. Phys. Lett.*, 92(24):243111–3, 2008.

[23] C. L. Degen, M. Poggio, H. J. Mamin, C. T. Rettner, and D. Rugar. Nanoscale magnetic resonance imaging. *Proc. Nat. Acad. Sci.*, 106(5): 1313–1317, 2009. URL http://www.pnas.org/content/106/5/1313.abstract. 10.1073/pnas.0812068106.

[24] V. V. Dobrovitski, G. de Lange, D. Ristè, and R. Hanson. Bootstrap tomography of the pulses for quantum control. *Phys. Rev. Lett.*, 105: 077601, Aug 2010. doi: 10.1103/PhysRevLett.105.077601. URL http://link.aps.org/doi/10.1103/PhysRevLett.105.077601.

[25] F. Dolde, H. Fedder, M. W. Doherty, T. Nöbauer, F. Rempp, G. Balasubramanian, T. Wolf, F. Reinhard, L. C. L. Hollenberg, F. Jelezko, and J. Wrachtrup. Electric-field sensing using single diamond spins. *Nature Physics*, 7:459ñ463, 2011. URL http://dx.doi.org/10.1038/nphys1969.

[26] F. Dolde, I. Jakobi, B. Naydenov, N. Zhao, S. Pezzagna, C. Trautmann, J. Meijer, P. Neumann, F. Jelezko, and J. Wrachtrup. Room-temperature entanglement between single defect spins in diamond. *Nat. Phys.*, 9(3): 139–143, 2013. ISSN 1745-2473. URL http://dx.doi.org/10.1038/nphys2545. 10.1038/nphys2545.

[27] A. Dréau, M. Lesik, L. Rondin, P. Spinicelli, O. Arcizet, J.-F. Roch, and V. Jacques. Avoiding power broadening in optically detected magnetic resonance of single nv defects for enhanced dc magnetic field sensitivity. *Phys. Rev. B*, 84:195204, Nov 2011. doi: 10.1103/PhysRevB.84.195204. URL http://link.aps.org/doi/10.1103/PhysRevB.84.195204.

[28] K. H. Drexhage. Iv interaction of light with monomolecular dye layers. volume 12 of *Progress in Optics*, pages 163–232. Elsevier, 1974. URL http://dx.doi.org/10.1016/S0079-6638(08)70266-X.

[29] M. V. Dutt, L. Childress, L. Jiang, E. Togan, J. Maze, F. Jelezko, A. S. Zibrov, P. R. Hemmer, and M. D. Lukin. Quantum register based on individual electronic and nuclear spin qubits in diamond. *Science*, 316(5829):1312, 2007. URL http://dx.doi.org/10.1126/science.1139831.

[30] R. J. Epstein, F. M. Mendoza, Y. K. Kato, and D. D. Awschalom. Anisotropic interactions of a single spin and dark-spin spectroscopy in diamond. *Nature Phys.*, 1(2):94, NOV 2005. URL http://dx.doi.org/10.1038/nphys141.

[31] S. Foletti, H. Bluhm, D. Mahalu, V. Umansky, and A. Yacoby. Universal quantum control of two-electron spin quantum bits using dynamic nuclear polarization. *Nature Phys.*, 5:903, 2009. URL http://dx.doi.org/10.1038/NPHYS1424.

[32] G. D. Fuchs, V. V. Dobrovitski, R. Hanson, A. Batra, C. D. Weis, T. Schenkel, and D. D. Awschalom. Excited-state spectroscopy using single spin manipulation in diamond. *Phys. Rev. Lett.*, 101:117601, 2008. URL http://dx.doi.org/10.1103/PhysRevLett.101.117601.

[33] T. Gaebel, M. Domhan, I. Popa, C. Wittmann, P. Neumann, F. Jelezko, J.R. Rabeau, N. Stavrias, A.D. Greentree, S. Prawer, et al. Room-temperature coherent coupling of single spins in diamond. *Nature Physics*, 2:408–413, 2006. URL http://dx.doi.org/10.1038/nphys318.

[34] M. Garwood and L. Delabarre. The return of the frequency sweep: Designing adiabatic pulses for contemporary nmr. *Journal of Magnetic Resonance*, 153:155, 2001. doi: 10.1006/jmre.2001.2340.

[35] P. Glover and P. Mansfield. Limits to magnetic resonance microscopy. *Rep. Prog. Phys.*, 65(10):1489, 2002. URL http://dx.doi.org/10.1088/0034-4885/65/10/203.

[36] G. Goldstein, P. Cappellaro, J. R. Maze, J. S. Hodges, L. Jiang, A. S. Sørensen, and M. D. Lukin. Environment-assisted precision measurement. *Phys. Rev. Lett.*, 106(14):140502, 2011. URL http://link.aps.org/doi/10.1103/PhysRevLett.106.140502. PRL.

[37] M. S. Grinolds, P. Maletinsky, S. Hong, M. D. Lukin, R. L. Walsworth, and A. Yacoby. Quantum control of proximal spins using nanoscale magnetic resonance imaging. *Nat Phys*, 7:687–692, 2011.

[38] M. S. Grinolds, S. Hong, P. Maletinsky, L. Luan, M. D. Lukin, R. L. Walsworth, and A. Yacoby. Nanoscale magnetic imaging of a single electron spin under ambient conditions. *Nat. Phys.*, 9(4):215–219, 2013. ISSN 1745-2473. URL http://dx.doi.org/10.1038/nphys2543. 10.1038/nphys2543.

[39] M. S. Grinolds, M. Warner, K. De Greve, Y. Dovzhenko, L. Thiel, R. L Walsworth, S. Hong, P. Maletinsky, and A. Yacoby. Subnanometre resolution in three-dimensional magnetic resonance imaging of individual dark spins. *Nat Nano*, 9:279–284, 2014.

[40] B. Grotz, J. Beck, P. Neumann, B. Naydenov, R. Reuter, F. Reinhard, Fedor Jelezko, J. Wrachtrup, D. Schweinfurth, B. Sarkar, and P. R. Hemmer. Sensing external spins with nitrogen-vacancy diamond. *New J. Phys*, 13 (5):055004, 2011. ISSN 1367-2630. URL http://stacks.iop.org/1367-2630/13/i=5/a=055004.

[41] A. Gruber, A. Drabenstedt, C. Tietz, L. Fleury, J. Wrachtrup, and C. von Borczyskowski. Scanning confocal optical microscopy and magnetic resonance on single defect centers. *Science*, 276(5321):2012–2014, 1997.

[42] T. Gullion and J. Schaefer. Elimination of resonance offset effects in rotational-echo, double-resonance nmr. *Journal of Magnetic Resonance (1969)*, 92(2):439 – 442, 1991. ISSN 0022-2364. doi: 10.1016/0022-2364(91)90286-3. URL http://www.sciencedirect.com/science/article/pii/0022236491902863.

[43] R. Hanson, L. P. Kouwenhoven, J. R. Petta, S. Tarucha, and L. M. K. Vandersypen. Spins in few-electron quantum dots. *Rev. Mod. Phys.*, 79: 1217, 2007. doi: 10.1103/RevModPhys.79.1217. URL http://link.aps.org/abstract/RMP/v79/p1217.

[44] W. Harneit. Fullerene-based electron-spin quantum computer. *Phys. Rev. A*, 65(3):032322, 2002. URL http://link.aps.org/doi/10.1103/PhysRevA.65.032322. PRA.

[45] B. J. M. Hausmann, M. Khan, Y. Zhang, T. M. Babinec, K. Martinick, M. McCutcheon, P. R. Hemmer, and M. Loncar. Fabrication of diamond nanowires for quantum information processing applications. *Diamond Relat. Mater.*, 19:621–629, 2010. ISSN 0925-9635. doi: DOI:10.1016/j.diamond.2010.01.011. URL http://dx.doi.org/10.1016/j.diamond.2010.01.011.

[46] P. Hemmer. Toward molecular-scale mri. *Science*, 339(6119):529–530, 2013. URL http://www.sciencemag.org/content/339/6119/529.short.

[47] C. Hettich, C. Schmitt, J. Zitzmann, S. Kühn, I. Gerhardt, and V. Sandoghdar. Nanometer resolution and coherent optical dipole coupling of two individual molecules. *Science*, 298(5592):385–389, 2002. doi: 10.1126/science.1075606. URL http://www.sciencemag.org/content/298/5592/385.abstract.

[48] S. Hong, M. S. Grinolds, P. Maletinsky, R. L. Walsworth, M. D. Lukin, and A. Yacoby. Coherent, mechanical control of a single electronic spin. *Nano Letters*, 12(8):3920–3924, 2012.

[49] F. Jelezko, T. Gaebel, I. Popa, A. Gruber, and J. Wrachtrup. Observation of coherent oscillations in a single electron spin. *Phys. Rev. Lett.*, 92:76401, 2004. doi: http://dx.doi.org/10.1103/PhysRevLett.92.076401. URL http://dx.doi.org/10.1103/PhysRevLett.92.076401.

[50] R. Kalish, C. Uzan-Saguy, B. Philosoph, V. Richter, J. P. Lagrange, E. Gheeraert, A. Deneuville, and A. T. Collins. Nitrogen doping of diamond by ion implantation. *Diamond Relat. Mater.*, 6:516–520, 1997. ISSN 0925-9635. doi: DOI:10.1016/S0925-9635(96)00657-7. URL http://www.sciencedirect.com/science/article/B6TWV-3WHKY2W-29/2/f1ef1f79df975f256863d5018b54e7da.

[51] B. E. Kane. A silicon-based nuclear spin quantum computer. *Nature*, 393:133–137, 1998. URL http://dx.doi.org/10.1038/30156.

[52] K. Karrai and I. Tiemann. Interfacial shear force microscopy. *Phys. Rev. B*, 62:13174, 2000. URL hppt://dx.doi.org/10.1103/PhysRevB.62.13174.

[53] J. R. Kirtley, M. B. Ketchen, K. G. Stawiasz, J. Z. Sun, W. J. Gallagher, S. H. Blanton, and S. J. Wind. High-resolution scanning squid microscope. *Appl. Phys. Lett.*, 66(9):1138–1140, 1995.

[54] T. Kohashi, M. Konoto, and K. Koike. High-resolution spin-polarized scanning electron microscopy (spin sem). *J. Electron Microsc.*, 59:43–52, 2010. doi: 10.1093/jmicro/dfp047. URL http://dx.doi.org/10.1093/jmicro/dfp047.

[55] S. Kuhn, C. Hettich, C. Schmitt, J.P.H. Poizat, and V. Sandoghdar. Diamond colour centres as a nanoscopic light source for scanning near-field optical microscopy. *J. Microsc.*, 202:2–6, 2001. URL http://dx.doi.org/10.1046/j.1365-2818.2001.00829.x.

[56] C. Kurtsiefer, S. Mayer, P. Zarda, and H. Weinfurter. Stable solid-state source of single photons. *Phys. Rev. Lett.*, 85:290–293, 2000. URL http://dx.doi.org/10.1103/PhysRevLett.85.290.

[57] N.D. Lai, D. Zheng, F. Jelezko, F. Treussart, and J.-F. Roch. Influence of a static magnetic field on the photoluminescence of an ensemble of nitrogen-vacancy color centers in a diamond single-crystal. *Appl. Phys.*

Lett., 95:133101, 2009. URL
http://dx.doi.org/10.1063/1.3238467.

[58] A. Laraoui and C. A. Meriles. Approach to dark spin cooling in a diamond nanocrystal. *ACS Nano*, 7(4):3403–3410, 2013. ISSN 1936-0851. doi: 10.1021/nn400239n. URL http://dx.doi.org/10.1021/nn400239n.

[59] R. G. Larsen and D. J. Singel. Double electron–electron resonance spin–echo modulation: Spectroscopic measurement of electron spin pair separations in orientationally disordered solids. *The Journal of Chemical Physics*, 98(7):5134–5146, 1993. doi: 10.1063/1.464916. URL http://link.aip.org/link/?JCP/98/5134/1.

[60] C. L. Lee, E. Gu, M. D. Dawson, I. Friel, and G. A. Scarsbrook. Etching and micro-optics fabrication in diamond using chlorine-based inductively-coupled plasma. *Diamond Relat. Mater.*, 17:1292–1296, 2008. URL http://dx.doi.org/10.1016/j.diamond.2008.01.011.

[61] S. C. Lee, K. Kim, J. Kim, S. Lee, J. H. Yi, S. W. Kim, K. S. Ha, and C. Cheong. One micrometer resolution nmr microscopy. *J. mag. res.*, 150: 207, 2001. URL http://dx.doi.org/10.1006/jmre.2001.2319.

[62] P. Maletinsky, S. Hong, M. S. Grinolds, Birgit J. M. Hausmann, M. D. Lukin, R. Walsworth, Marko Loncar, and A. Yacoby. A robust scanning diamond sensor for nanoscale imaging with single nitrogen-vacancy centres. *Nat Nano*, 7(5):320–324, 2012.

[63] H. J. Mamin, M. Poggio, C. L. Degen, and D. Rugar. Nuclear magnetic resonance imaging with 90-nm resolution. *Nature*, 2:301–306, 2007. doi: http://dx.doi.org/10.1038/nnano.2007.105.

[64] H. J. Mamin, M. H. Sherwood, and D. Rugar. Detecting external electron spins using nitrogen-vacancy centers. *Phys. Rev. B*, 86(19):195422, 2012. URL http://link.aps.org/doi/10.1103/PhysRevB.86.195422. PRB.

[65] H. J. Mamin, M. Kim, M. H. Sherwood, C. T. Rettner, K. Ohno, D. D. Awschalom, and D. Rugar. Nanoscale nuclear magnetic resonance with a nitrogen-vacancy spin sensor. *Science*, 339(6119):557–560, 2013. URL http://www.sciencemag.org/content/339/6119/557.abstract.

[66] Peter Mansfield. Snapshot magnetic resonance imaging (nobel lecture). *Angewandte Chemie International Edition*, 43(41):5456–5464, 2004. ISSN 1521-3773. doi: 10.1002/anie.200460078. URL http://dx.doi.org/10.1002/anie.200460078.

[67] Y. Martin and H. K. Wickramasinghe. Magnetic imaging by "force microscopy" with 1000 [a-ring] resolution. *Appl. Phys. Lett.*, 50(20): 1455–1457, 1987.

[68] P. C. Maurer, J. R. Maze, P. L. Stanwix, L. Jiang, A. V. Gorshkov, A. A. Zibrov, B. Harke, J. S. Hodges, A. S. Zibrov, A. Yacoby, D. Twitchen, S. W. Hell, R. L. Walsworth, and M. D. Lukin. Far-field optical imaging and manipulation of individual spins with nanoscale resolution. *Nature Phys.*, 6:912, 2010. URL http://dx.doi.org/10.1038/NPHYS1774.

[69] P. C. Maurer, G. Kucsko, C. Latta, L. Jiang, N. Y. Yao, S. D. Bennett, F. Pastawski, D. Hunger, N. Chisholm, M. Markham, D. J. Twitchen, J. I. Cirac, and M. D. Lukin. Room-temperature quantum bit memory exceeding one second. *Science*, 336:1283, June 2012. doi: 10.1126/science.1220513.

[70] J. R. Maze, P. L. Stanwix, J. S. Hodges, S. Hong, J. M. Taylor, P. Cappellaro, L. Jiang, M. V. Gurudev Dutt, E. Togan, A. S. Zibrov, A. Yacoby, R. L. Walsworth, and M. D. Lukin. Nanoscale magnetic sensing with an individual electronic spin in diamond. *Nature*, 455(7213):644–647, 2008.

[71] L. P. McGuinness, Y. Yan, A. Stacey, D. A. Simpson, L. T. Hall, D. Maclaurin, S. Prawer, P. Mulvaney, J. Wrachtrup, F. Caruso, R. E. Scholten, and L. C. L. Hollenberg. Quantum measurement and orientation tracking of fluorescent nanodiamonds inside living cells. *Nature Nanotech.*, 6:358–363, 2011. ISSN 1748-3387. URL http://dx.doi.org/10.1038/nnano.2011.64.

[72] J. Michaelis, C. Hettich, J. Mlynek, and V. Sandoghdar. Optical microscopy using a single-molecule light source. *Nature*, 405:325–328, 2000. URL http://dx.doi.org/10.1038/35012545.

[73] A. Morello, J. J. Pla, F. A. Zwanenburg, K. W. Chan, K. Y. Tan, H. Huebl, M. Mottonen, C. D. Nugroho, C. Yang, J. A. van Donkelaar, A. D. C. Alves, D. N. Jamieson, C. C. Escott, L. C. L. Hollenberg, R. G. Clark, and A. S.

Dzurak. Single-shot readout of an electron spin in silicon. *Nature*, 467: 687, 2010. URL http://dx.doi.org/10.1038/nature09392.

[74] R. R. Nair, M. Sepioni, I.-L. Tsai, O. Lehtinen, J. Keinonen, A. V. Krasheninnikov, T. Thomson, A. K. Geim, and I. V. Grigorieva. Spin-half paramagnetism in graphene induced by point defects. *Nature Physics*, 8: 199–202, March 2012. URL http://dx.doi.org/10.1038/nphys2183.

[75] B. Naydenov, F. Reinhard, A. Lämmle, V. Richter, R. Kalish, l. F. S. D Haenens-Johansson, M. Newton, F. Jelezko, and J. Wrachtrup. Increasing the coherence time of single electron spins in diamond by high temperature annealing. *Appl. Phys. Lett.*, 97:242511, 2010. URL http://dx.doi.org/10.1063/1.3527975.

[76] P. Neumann, R. Kolesov, B. Naydenov, J. Beck, F. Rempp, M. Steiner, V. Jacques, G. Balasubramanian, M. L. Markham, D. J. Twitchen, S. Pezzagna, J. Meijer, J. Twamley, F. Jelezko, and J. Wrachtrup. Quantum register based on coupled electron spins in a room-temperature solid. *Nature Physics*, 6:249–253, 2010. ISSN 1745. URL http://dx.doi.org/10.1038/nphys1536.

[77] M. A. Nielsen and I. L. Chuang. *Quantum Computation and Quantum Information*. Cambridge Univ. Press, 2000.

[78] N. M. Nusran, M. U. Momeen, and M. V. G. Dutt. High-dynamic-range magnetometry with a single electronic spin in diamond. *Nature Nanotechnology*, 7:109–113, February 2012. doi: 10.1038/nnano.2011.225.

[79] B. K. Ofori-Okai, S. Pezzagna, K. Chang, M. Loretz, R. Schirhagl, Y. Tao, B. A. Moores, K. Groot-Berning, J. Meijer, and C. L. Degen. Spin properties of very shallow nitrogen vacancy defects in diamond. *Phys. Rev. B*, 86(8):081406, 2012. URL http://link.aps.org/doi/10.1103/PhysRevB.86.081406. PRB.

[80] K. Ohno, F. J. Heremans, L. C. Bassett, B. A. Myers, D. M. Toyli, A. C. Bleszynski Jayich, C. J. Palmstrom, and D. D. Awschalom. Engineering shallow spins in diamond with nitrogen delta-doping. *Applied Physics Letters*, 101(8):082413–5, 2012.

[81] C.-A. Palma and P. Samori. Blueprinting macromolecular electronics. *Nat. Chem.*, 3(6):431–436, 2011. ISSN 1755-4330. URL http://dx.doi.org/10.1038/nchem.1043. 10.1038/nchem.1043.

[82] S. Pezzagna, D. Wildanger, P. Mazarov, A. D. Wieck, Y. Sarov, I. Rangelow, B. Naydenov, F. Jelezko, S. W. Hell, and J. Meijer. Nanoscale engineering and optical addressing of single spins in diamond. *Small*, 6:2117–2121, 2010. URL http://dx.doi.org/10.1002/smll.201000902.

[83] J. R. Rabeau, P. Reichart, G. Tamanyan, D. N. Jamieson, S. Prawer, F. Jelezko, T. Gaebel, I. Popa, M. Domhan, and J. Wrachtrup. Implantation of labelled single nitrogen vacancy centers in diamond using [sup 15]n. *Appl. Phys. Lett.*, 88(2):023113–3, 2006.

[84] I. I. Rabi, J. R. Zacharias, S. Millman, and P. Kusch. A new method of measuring nuclear magnetic moment. *Phys. Rev.*, 53:318–318, Feb 1938. doi: 10.1103/PhysRev.53.318. URL http://link.aps.org/doi/10.1103/PhysRev.53.318.

[85] P. Recher and B. Trauzettel. Quantum dots and spin qubits in graphene. *Nanotechnology*, 21:302001, 2010. URL http://dx.doi.org/10.1088/0957-4484/21/30/302001.

[86] E. Rittweger, K. Y. Han, S. E. Irvine, C. Eggeling, and S. W. Hell. Sted microscopy reveals crystal colour centres with nanometric resolution. *Nature Photon.*, 3:144, 2009. URL http://dx.doi.org/10.1038/NPHOTON.2009.2.

[87] L. Rondin, J.-P. Tetienne, P. Spinicelli, C. Dal Savio, K. Karrai, G. Dantelle, A. Thiaville, S. Rohart, J.-F. Roch, and V. Jacques. Nanoscale magnetic field mapping with a single spin scanning probe magnetometer. *Applied Physics Letters*, 100(15):153118, 2012. doi: 10.1063/1.3703128. URL http://link.aip.org/link/?APL/100/153118/1.

[88] D. Rugar, R. Budakian, H. J. Mamin, and B. W. Chui. Single spin detection by magnetic resonance force microscopy. *Nature*, 430:329, 2004. doi: 10.1038/nature02658.

[89] M. Schaffry, E. M. Gauger, J. J. L. Morton, and S. C. Benjamin. Proposed spin amplification for magnetic sensors employing crystal defects. *Phys. Rev. Lett.*, 107(20):207210, 2011. URL

http://link.aps.org/doi/10.1103/PhysRevLett.107.207210.
PRL.

[90] R. S. Schoenfeld and W. Harneit. Real time magnetic field sensing and imaging using a single spin in diamond. *Phys. Rev. Lett.*, 106(3):030802, 2011. URL
http://link.aps.org/doi/10.1103/PhysRevLett.106.030802.
PRL.

[91] S. Sekatskii and V. Letokhov. Nanometer-resolution scanning optical microscope with resonance excitation of the fluorescence of the samples from a single-atom excited center. *JETP Lett.*, 63:319–323, 1996. URL
http://dx.doi.org/10.1134/1.567024.

[92] F. Shi, Q. Zhang, B. Naydenov, F. Jelezko, J. Du, F. Reinhard, and J. Wrachtrup. Quantum logic readout and cooling of a single dark electron spin. *Phys. Rev. B*, 87(19):195414, 2013. URL
http://link.aps.org/doi/10.1103/PhysRevB.87.195414. PRB.

[93] J. A. Sidles, J. L. Garbini, K. J. Bruland, D. Rugar, O. Züger, S. Hoen, and C. S. Yannoni. Magnetic resonance force microscopy. *Rev. Mod. Phys.*, 67 (1):249–265, 1995. URL
http://link.aps.org/doi/10.1103/RevModPhys.67.249. RMP.

[94] T. Staudacher, F. Shi, S. Pezzagna, J. Meijer, J. Du, C. A. Meriles, F. Reinhard, and J. Wrachtrup. Nuclear magnetic resonance spectroscopy on a (5-nanometer)3 sample volume. *Science*, 339(6119):561–563, 2013. URL
http://www.sciencemag.org/content/339/6119/561.abstract.

[95] J. M. Taylor, P. Cappellaro, L. Childress, L. Jiang, D. Budker, P. R. Hemmer, A. Yacoby, R. Walsworth, and M. D. Lukin. High-sensitivity diamond magnetometer with nanoscale resolution. *Nat Phys*, 4(10): 810–816, 2008.

[96] E. Togan, Y. Chu, A. S. Trifonov, L. Jiang, J. Maze, L. Childress, A. S. Dutt, M. V. G. AU Sorensen, P. R. Hemmer, A. S. Zibrov, and M. D. Lukin. Quantum entanglement between an optical photon and a solid-state spin qubit. *Nature*, 466:730–734, 2010. URL
http://dx.doi.org/10.1038/nature09256.

[97] D. M. Toyli, C. D. Weis, G. D. Fuchs, T. Schenkel, and D. D. Awschalom. Chip-scale nanofabrication of single spins and spin arrays in diamond. *Nano Lett.*, 10:3168–3172, 2010. URL http://dx.doi.org/10.1021/nl102066q.

[98] E. van Oort and M. Glasbeek. Optically detected low field electron spin echo envelope modulations of fluorescent n-v centers in diamond. *Chem. Phys.*, 143:131–140, 1990. ISSN 0301-0104. URL http://dx.doi.org/10.1016/0301-0104(90)85013-M.

[99] G. Waldherr, J. Beck, P. Neumann, R. S. Said, M. Nitsche, M. L. Markham, D. J. Twitchen, J. Twamley, F. Jelezko, and J. Wrachtrup. High-dynamic-range magnetometry with a single nuclear spin in diamond. *Nature Nanotechnology*, 7:105–108, February 2012. doi: 10.1038/nnano.2011.224.

[100] F. Wolny, T. Mühl, U. Weissker, K. Lipert, J. Schumann, A. Leonhardt, and B. Büchner. Iron filled carbon nanotubes as novel monopole-like sensors for quantitative magnetic force microscopy. *Nanotechnology*, 21:435501, 2010. URL http://stacks.iop.org/0957-4484/21/i=43/a=435501.

[101] X. Xu, B. Sun, P. R. Berman, D. G. Steel, A. S. Bracker, D. Gammon, and L. J. Sham. Coherent optical spectroscopy of a strongly driven quantum dot. *Science*, 317(5840):929–932, 2007. URL http://dx.doi.org/10.1126/science.1142979.

[102] N. Y. Yao, L. Jiang, A. V. Gorshkov, Z. X. Gong, A. Zhai, L. M. Duan, and M. D. Lukin. Robust quantum state transfer in random unpolarized spin chains. *Phys. Rev. Lett.*, 106(4):040505, 2011. URL http://link.aps.org/doi/10.1103/PhysRevLett.106.040505. PRL.

[103] N. Y. Yao, L. Jiang, A. V. Gorshkov, P. C. Maurer, G. Giedke, J. I. Cirac, and M. D. Lukin. Scalable architecture for a room temperature solid-state quantum information processor. *Nat Commun*, 3:800, 2012. 10.1038/ncomms1788.

[104] J. F. Ziegler. *The Stopping and Range of Ions in Matter*. 2010. URL http://www.srim.org.

[105] O. Zuger and D. Rugar. First images from a magnetic resonance force microscope. *Appl. Phys. Lett.*, 63(18):2496–2498, 1993.

Colophon

THIS THESIS WAS TYPESET using LaTeX, originally developed by Leslie Lamport and based on Donald Knuth's TeX. The body text is set in 11 point Arno Pro, designed by Robert Slimbach in the style of book types from the Aldine Press in Venice, and issued by Adobe in 2007. A template, which can be used to format a PhD thesis with this look and feel, has been released under the permissive MIT (X11) license, and can be found online at github.com/suchow/ or from the author at suchow@post.harvard.edu.